X-Ray diagnostics and X-ray imaging of laser-produced plasmas

Olena Turianska

université de BORDEAUX

THÈSE PRÉSENTÉE

POUR OBTENIR LE GRADE DE

DOCTEUR DE

L'UNIVERSITÉ DE BORDEAUX

ECOLE DOCTORALE SCIENCES PHYSIQUES ET DE L'INGENIEUR

SPÉCIALITÉ

LASERS, MATIERE ET NANOSCIENCES

Par Olena Turianska

X-Ray diagnostics and X-ray imaging of laser-produced plasmas

Soutenue le 01.12.2022

Membres du jury :

Mme Petra KOESTER, Chargée de recherche, CNR-INO Pisa, Italie, Rapporteur

M. Luca VOLPE, Professeur des universités, University of Salamanca, Centro de Láseres Pulsados (CLPU), Rapporteur

M. Dimitri BATANI, Professeure des universités, CELIA - Centre Lasers Intenses et Applications, Université de Bordeaux, Directeur de these

M. Emmanuel D'HUMIERES, Professeur, CELIA - Centre Lasers Intenses et Applications, Université de Bordeaux, Examinateur

M. Pravesh PATEL, Directeur scientifique, Focused Energy USA, Examinateur

Mme Katarzyna BATANI, Associate Professor, Institute of Plasma Physics and Laser Microfusion , Examinateur

Titre : Diagnostic par rayons X et imagerie par rayons X de plasmas produits par laser

Résumé :

Ce travail s'est axé sur le développement et l'optimisation des diagnostics par rayons X pour l'étude des plasmas produits par laser. En particulier l'imagerie par contraste de phase à rayons X résolue en temps (XPCI) est étudiée comme alternative à l'utilisation de la radiographie par rayons X pour sonder les phénomènes dynamiques dans les plasmas à haute densité. L'XPCI a été spécifiquement appliquée pour étudier la dynamique des chocs générés par laser dans des cibles en plastique. Les résultats expérimentaux obtenus ont été complétés par des simulations hydrodynamiques 1D et 2D. Il a été possible de réaliser l'XPCI dans diverses installations laser à haute énergie, avec des conditions d'irradiation laser tres différentes.

De plus, les travaux ont également porté sur la caractérisation des spectres de bremsstrahlung générés lors d'interactions laser-plasma de haute intensité à l'échelle de la femtoseconde, en vue de leur utilisation comme source de "backlighter" dans l'XPCI. Ces émissions de rayons X sont également intéressantes en tant que diagnostic de plasma car elles permettent de caractériser les électrons chauds qui sont responsables de l'émission de bremsstrahlung. Un module semi-analytique a été développé permettant une estimation rapide de la température de la population d'électrons chauds à partir des spectres mesurés.

Ces sujets traités sont d'importance pour la physique de la haute densité d'énergie (HED) et pour la fusion par confinement inertiel.

Mots clés : ondes de choc, plasmas produits par laser, Diagnostics rayons X, Imagerie par contraste de phase à rayons X, canon Bremsstrahlung

Title : X-Ray diagnostics and X-ray imaging of laser-produced plasmas

Abstract :

This work was focused on the development and optimization of X-ray diagnostics for the study of laser produced plasmas and in particular time-resolved x-ray contrast imaging (XPCI) as an alternative to the use of X-ray radiography in probing dynamical phenomena in high density plasmas. XPCI was specifically applied to study the dynamics of laser-generated shocks in plastic targets. The obtained experimental results were completed by 1D and 2D hydrodynamic simulations. It was possible to realize XPCI in various high-energy laser facilities, for variable nanosecond laser drive conditions.

In addition, the work also focused on the characterization of bremsstrahlung spectra generated in high-intensity femtosecond-scale laser-plasma interactions, for their use as a backlighter source in XPCI. These X-ray emissions are also interesting as a plasma diagnostic because they allow us to characterize the hot electrons which are responsible for the bremsstrahlung emission. A semi-analytical module was developed allowing for a fast estimation of the hot electron population temperature from the measured spectra.

These developed topics are of importance for high energy density (HED) physics and for inertial confinement fusion.

Keywords : Shock waves, laser produced plasmas, X-ray diagnostics, X-ray phase contrast imaging, Bremsstrahlung cannon

Table of Contents

Statement of Original Authorship

The work contained in this thesis has not been previously submitted to meet requirements for an award at this or any other higher education institution. To the best of my knowledge and belief, the thesis contains no material previously published or written by another person except where due reference is made.

Signature: _____

Date: _____

Acknowledgements

Life is so interesting and unpredictable…

I moved to France in October 2018. These 4 years were crazy! I travelled a lot, met amazing people, run interesting experimental campaign, pass through pandemic and war…

First of all, I would like to say thank for my grandparents who build “strong core” on me. I remember I должна держать хвост пистолетом and fight or die. Be honest after 24 of February I thought my PhD is done and I would be not able to wright anything. So, I was wrong! I would like to dedicate this thesis to my dear grandparents Nina and Victor who left this world at 2017.

The second person that I would like to thank is Dimitri Batani, that took me in his group and gave a lot of great opportunities. You supported and guided my research during these four years. Thank you for believing on me even in a darkness time.

Then I would like to thank the jury members. I was honored to have the opportunity to present my work in front of such experts. A big thank to Petra Koester, Luca Volpe , Pravesh Patel ,Katarzyna Batani, Emmanuel D'Humieres and Daniele Margarone having carefully read my manuscript who agreed to be part of the committee of my PhD defence and for having carefully read my manuscript . I would like to thank them also for the interesting discussion taken during my PhD defense.

A special thanks goes to Abutrab Aliverdiev . We had a lot of discussions, and I am sure that this helped me a lot during my PhD. I really enjoyed working with you and I learnt a lot I hope one day we see each other in real life and will drink glass of good cognac 😊.

I also would like to thank all the collaborators with whom I had the pleasure to work with, in particular Paul, Luca, Francesco, Sergey, Naomi, Artem, Sero, Ghassan and Sophia. Sophia you are my soulmate and partner in crime. Love you !

I would like to acknowledge my old pals Таня Некраса, Лиза, Женя и Татьяна Крайняя. (Number 225 have spatial meaning for us.) Katia thanks you now Prague is like my second home ! Also big thanks for Крас, Ярик, Леонид, Коля, Надя, Дима, Николай, Макс, Таня Чередниченко, Лера, Оля, Нина. Hope to see all of you soon!

A thesis work is for sure a challenging and busy period, but it was made less difficult by the presence of colleagues and friends. Alessandro and Gloria, Corisande and Nikita thanks for been all time on my side.

My spatial thanks for family of Tenuta who adopted me and support me on my way. Olga, Joao and Nina thank you a lot for your kindness and advises.

A special thanks also to other colleagues that I had the opportunity to meet: Donaldi, Diego, Luke, Christos, Francesco, Phill, Antoine, Guillaume, Stefan, Micha, Gabriel and Romain, Duncan, Aleksander, Thoma, Diluka and Alana.

I would like to thank also the administrative and informatic staff of the CELIA laboratory composed by Sophie, Celine, Sonia Richard and Gaetan and director of CELIA Eric. Your patience, your kindness and your professionalism are essential for the laboratory.

Wondaful people always come into my life in the moment when I don't expect them but really need them. Thank you, Markus Roth and all focused energy team! I am starting new chapter in my life with you.

The last, but not least, I thank my mother for her support and believe on me !

If you can find the North star you are never lost …

Introduction

Plasma physics is currently one of the most active subdisciplines of physics. The measurement of the parameters of laboratory plasmas, termed plasma diagnostics, is based on a wide variety of characteristic plasma phenomena. The objective of plasma diagnostics is to deduce information about the state of the plasma from practical observations of physical processes and their effects. In this work, we study X-ray diagnostics and X-ray imaging of laser-produced plasmas, which are important for studying the physics of matter in extreme conditions and for inertial confinement fusion.

The first part of the work consists of studying the bremsstrahlung spectrum generated in high-intensity laser-plasma interactions. Characterizing the bremsstrahlung spectrum is important because it can serve as the X-ray source used for backlighting in experiments based on X-ray radiography or X-ray phase contrast imaging (XPCI). This is also useful as a plasma diagnostic because it allows the characterization of the hot electrons that are responsible for bremsstrahlung emission. In particular, I analyzed the experimental data from a diagnostic called the Bremsstrahlung Cannon (BSC). The BSC consists of a stack of detectors, the imaging plates, separated by filters of different materials and thicknesses. The BSC was used in several experiments at CLPU (Spain), GSI (Germany), and Vulcan (UK). Bremsstrahlung spectra are usually assumed to be exponential, corresponding to a hot electron Maxwellian distribution. The slope of this exponential is taken as a representative of the temperature of the hot electrons. Here, I developed an easy semi-analytical module for estimating hot electron temperature.

At the Centro de Láseres Pulsados (CLPU) in Salamanca, the main goal of the experiment with the VEGA-2 laser was the study of hot electron-driven blast waves propagating in solid materials. The temperature of the general hot electron was calculated from BSC data.

The second part of the thesis addresses the development of X-ray phase contrast imaging (XPCI) diagnostics and its applications to the study of shock wave propagation in solid targets. In the second part of the manuscript, I presented three experimental campaigns where XPCI was used.

For the campaign at the Vulcan laser at the Rutherford Appleton Laboratory in the UK, X-ray phase contrast imaging was used to study shock waves. The propagation of a shock with a Gaussian shape was clearly observed. To follow the dynamics of shock propagation in time, images were obtained for different time delays of 15 ns, 25 ns, and 35 ns. The experimental results were compared to hydro

numerical results obtained from 1D and 2D hydro simulations performed using the code MULTI.

X-ray radiography and X-ray absorption spectroscopy of a titanium wire isochorically heated by laser-accelerated electrons were performed during the experiment at GSI, Germany (laser Phelix). We used a combination of X-ray spectroscopy and X-ray radiography to understand the state of matter heated by electrons. X-ray phase-contrast imaging (XPCI) was also tested in this experiment for imaging cold wire targets. The experiment on the heated wire was studied by time-resolved X-ray radiography.

Finally, XPCI was tested at the large-scale facility Omega EP in Rochester, US. In this experiment, we were able not only to detect a first shock but also to detect a second shock launched by a second laser pulse in the target, a task that has proven to be very difficult using conventional X-ray radiography based on absorption.

Chapter 1: Introduction

1.1 GENERAL ON LASER-PLASMA INTERACTION

1.1.1 Plasma general description

Atoms that are at least partially ionized are considered to be in the state of matter called plasma. This fundamental characteristic indicates that the electromagnetic fields produced by the propagation of the particles themselves have a significant impact on the motion of the particles, which highlights the complexity of plasma physics. The difference between electromagnetic and charged fields is what causes plasmas to respond as a group. Oscillations, also known as plasma waves, are formed by the coherent motion of charged particles.

The term "plasma" encompasses a wide range of systems, from weakly ionized plasma, such as that found in the Earth's ionosphere, where only a small percentage of free electrons and ions interact with neutral atoms and molecules, to highly ionized and hot plasmas, such as those found in space or in fusion laboratories.

A major property of plasmas, called quasi-neutrality, is directly linked to their ability to react to any perturbation and consequently neutralize a local electrical perturbation. In a plasma, the electric field created by a charged particle is screened by opposite charges beyond a certain distance, resulting in the plasma being globally neutral. This quasi-neutrality condition is mathematically described by

$$-en_e + \sum_i Z^* e n_i = 0 \quad (1.1)$$

With n_e the electron density e the elementary charge Z^* the ionization degree and n_i the density of the ionic species of index i.

1.1.2 Plasma characteristic lengths

In a plasma, several lengths can be determined, and they play a crucial role in characterizing plasma interactions or interactions between a plasma and an external beam. These lengths are determined based on the unique characteristics of a plasma, including the different types of particle interactions that can occur depending on the level of quasi-neutrality defined on a particular length scale. One important local phenomenon in plasmas is particle collisions, specifically Coulomb scattering. The hierarchy of characteristic lengths allows for the description of both collisional and collective aspects of plasma interactions, as well as the estimation of the strength of interactions between particles in the plasma.

Landau length

The minimum distance between two plasma electrons is called the Landau length r0 and it is defined at a distance where the electron kinetic and potential energies are equal:

$$\frac{mev_e^2}{2} = \frac{e^2}{4\pi\varepsilon_0 r_0} \text{ (1.2)}$$

where ε_0 is a vacuum permittivity. Then Landau length r_0 is equal to:

$$r_0 = \frac{e^2}{4\pi\varepsilon_0 k_B T_e} \text{ (1.3)}$$

The generalized Landau length for the interaction between two particles α and β in a plasma with respective charges Zα and Zβ can be also defined using the same classical approach. Then the generalized Landau length rαβ is given by:

$$r_{\alpha\beta} = \frac{Z_\alpha Z_\beta e^2}{4\pi\varepsilon_0 \mu v_r^2} \text{ (1.4)}$$

Wigner-Seitz radius

The Wigner- Seitz radius is a variable that determines the mean distance a between two plasma electrons and is dependent on the electron density.

$$\alpha=(4\pi n_e/3)^{-1/3} \text{ (1.5)}$$

Debye length

The presence of collective fluctuations poses one of the challenges in the theoretical description of plasmas. This fundamental property of plasmas, known as screening, was discovered by Peter Debye and Erich Huckel in 1923. It explains that while an electric charge can have a significant local influence on a plasma, its effect is limited to a specific region defined by the screening sphere. Within this sphere, the electric potential of the charge is screened by the surrounding particles. The characteristic length representing the range of the electric potential before it is screened is referred to as the screening length or Debye length λ_D. In other words, it is the distance beyond which plasma neutrality becomes valid. The Boltzmann-Poisson equation can be solved, with appropriate boundary conditions, to determine the screening length or Debye length.

$$\lambda_D = \sqrt{\frac{\varepsilon_0 k_B T_e}{4\pi e^2 n_e}} \text{ (1.6)}$$

Evaluating all the constants it can be also rewritten as:

$$\lambda_D[cm] = 743\sqrt{T_e[eV] \Big/ n_e[cm^{-3}]} \text{ (1.7)}$$

The number of electrons in the screening sphere is defined as:

$$N_D = \frac{4}{3}\pi n_e \lambda_D^3 \text{ (1.8)}$$

The screening effect can only be defined if there are enough electrons in the screening sphere $N_D \gg 1$.

De Broglie wavelength

Let's define the system of two plasma particles α and β. Then the relative velocity is $v_r = |v_\alpha - v_\beta|$ and $\mu = m_\alpha m_\beta / (m_\alpha + m_\beta)$ is the reduced mass of the interacting system. The De Broglie wavelength $\lambda_{Broglie}$ is the distance under which quantum diffraction effects start appearing in the interaction between particles α and β and can be written as:

$$\lambda_{Broglie} = \frac{\hbar}{\mu v_r} \quad (1.9)$$

where the reduced Plank's constant is denoted by $\hbar$. For the plasma electrons, a thermal plasma wavelength, also known as a De Broglie wavelength, can be defined.

$$\lambda_e = \frac{\hbar}{m_e v_{th}} \quad (1.10)$$

1.1.3 Plasma frequency

The electronic response to an electric perturbation inside of a plasma can be studied to learn more about its propensity to be quasi-neutral. Fast operations could generate a charge separation and break the neutrality, whereas slow processes would prevent this from happening. It allows the plasma to reorganize itself and keep the perturbation from forming. This collective effect leads to oscillations of the free electrons similarly to a harmonic oscillator, with a characteristic frequency ω_{pe}:

$$w_{pe} = \sqrt{\frac{n_e e^2}{m_e \varepsilon_0}} \quad (1.11)$$

The rapid oscillations of the plasma density characterized by w_{pe} are called Langmuir waves and correspond to the propagation of plasmons.

Electron - ion collision frequency

The collisional energy exchange between the plasma particles creates the thermal equilibrium in the plasma. Ions and electrons both arrive at their corresponding equilibrium temperatures, T_e and T_i, respectively. After that, electron-ion collisions initiate the electron-ion relaxation process, which continues until the thermal electron-ion equilibrium, $T_e = T_i$. It is characterized by a collision frequency $\nu_{e,i}$:

$$\nu_{e,i} = \frac{\sqrt{2\pi}}{12\pi^2} \frac{Z^2 e^4 n_i ln\Lambda}{\varepsilon_0^2 \sqrt{m_e} (k_B T_e)^{3/2}} \sim \frac{n_i}{T_e^{3/2}} \ln(\Lambda) \quad (1.12)$$

where $\ln(\Lambda)$ is a Coulomb logarithm that identifies the nature of collisions. This expression is valid for a weak collision-dominated classical plasma ($\Gamma_{e,i} >> 1$) and is in accordance with the Landau-Spitzer model. Similar approaches can be used to measure the frequency of collisions between electrons and either phonons $\nu_{e,ph}$, or electrons e, $\nu_{e,e}$. The distance a particle can travel in the plasma between two consecutive collisions can be determined using the collision frequency. This distance, called as the particle's mean free path, can be written as follows for an ion interacting with an electron in plasma:

$$l_{e,i} = \frac{v_{th}}{v_{e,i}} \text{ (1.13)}$$

Coulomb logarithm

Direct particle interactions, such as particle collisions or Coulomb scattering, are interaction processes that take place over distances less than the screening length. The impact parameter of interaction b, which approximately equals the distance between two interacting particles, is the parameter that determines whether type of effect is dominant. Let's introduce the parameter, referred to as "soft" (remote) and "hard" (near), collisions, which can measure the relative relevance of small-angle collisions against large-angle collisions. The impact parameter b described earlier is crucial in identifying the type of collisions. For a strongly coupled plasma one finds b < a. The minimum value of b – b_{min} is equal to the Landau length $r_{\alpha\beta}$ of the two colliding particles at an angle deflection of 90◦. It is a classical distance of minimum approach b0. Or if quantum effects are important, b has a minimum value of bmin that is equal to the De Broglie wavelength of the two-particle interaction. One can consequently define the type of collisions by:

- ✓ b ≈ b_{max}: soft collisions or small-angle scattering.
- ✓ b ≈ b_{min}: hard collisions or large-angle scattering.

The ratio quantifying the relative importance of small-angle to large-angle scattering is the Coulomb logarithm lnΛ:

$$ln\Lambda = ln\left(\frac{b_{max}}{b_{min}}\right) = \max\left(\ln\left(\frac{\max(\lambda_D, a)}{\max(b_0, \lambda_{Broglie})}\right), 2\right) \text{(1.14)}$$

This parameter defines the dominant collision phenomena in plasma. Its minimum value is often taken as 2 in the literature to ensure its positivity.

1.1.4 Plasma parameters

Plasma state is based on the relation between scale and length. Two parameters, the plasma coupling parameter and the degeneracy parameter Θ, which are related to density effects and statistics respectively, can be defined to generally represent the plasma state. The interaction of plasma depending on the scale length, processes can be classified as collisional or collective effects. Processes, for instance, that occur at scale lengths greater than the screening length λ_D are referred to as collective effects, such as dynamic screening or plasmon excitation. When the screening length is in the case of a highly non-ideal plasma, simultaneously extremely small (a particle's electric potential is virtually quickly filtered), with $\lambda_D >$ *a*, for interaction distances larger than *a*, collective effects are defined.

Plasma coupling parameter

The plasma coupling parameter is defined by the ratio between the density of electrostatic potential energy $< E_p >= e_0/4\pi\varepsilon_0 a$ and the mean density of kinetic energy $< E_k >= k_B T_e$. It measures the strength of electron-electron correlations in plasma.

$$\Gamma = {< E_p >}\Big/{< E_K >} = \frac{e^2}{4\varepsilon_0 k_B T_e} \sqrt[3]{\frac{4\pi n_e}{3}} \quad (1.15)$$

This variable makes possible classification. In a case than $\Gamma \gg 1$ strongly coupled plasmas are referred to as non-ideal, and electron interactions are dominant. Weakly coupled plasmas is one in which the long-range collective plasma effects tend to dominate and the plasma is perfect, collision less, and where the electrons' kinetic energy dominates over their potential energy in situation $\Gamma \ll 1$.

If the plasma being considered is not degenerate, the given expression for is acceptable. It is important to remember that equation behind describes the strength of correlations between electrons, or Γ_{ee}. The ionization state Z Γ_{ee} =Z $^{1/3}$ Γ_{ii} should also be taken into consideration when defining the similar parameter for ion correlations, which is Γ_{ii}.

Plasma degeneracy parameter

The parameter, plasma degeneracy degree, which evaluates the impact of the Pauli exclusion rule on the target electrons, is as follows:

$$\Theta = \frac{K_B T_e}{E_F} \quad (1.16)$$

where E_F is the Fermi energy. Θ is the ratio between the kinetic energy of the plasma electrons and their Fermi energy. This option allows each to decide between:

- ✓ Θ≤1 Degenerate plasmas that follow Fermi-Dirac statistics (Pauli exclusion's influence cannot be neglected). The kinetic energy of an electron is then given as E_k=$k_B T_e$+E_F
- ✓ Θ>>1 non-degenerate plasmas that conform by the Maxwell-Boltzmann statistics and have electrons with kinetic energy higher than their Fermi energy

The expression for the plasma coupling parameter should be rewritten in the case of degenerate plasmas:

$$\Gamma = \frac{e^2}{a(k_B T_e + E_F)} \quad (1.17)$$

1.1.5 Plasma waves

In the absence of imposed magnetic fields, the plasma waves in a simple case primarily consist of charge density fluctuations. We are using a model that treats the plasma as two separate components: electrons and ions (known as the two-fluid model). This model allows for the characterization of two distinct plasma waves, one with high frequency and the other with low frequency.

When a high-intensity laser beam with a specific angular frequency is focused on the surface of a target plasma, it rapidly creates and modifies the plasma's

propagation due to the presence of free electrons in the beam. The dispersion relation for an electromagnetic wave in a plasma is a mathematical relationship that describes how the wave's properties, such as its frequency and propagation speed, are related to the properties of the plasma.

$$w^{2=}w_p^2 + k_0^2c^2 \text{ (1.18)}$$

Where is k is wavenumber of laser radiation, c is speed of light w is plasma frequency. Electromagnetic waves is the high frequency one. The term proportional to the wavenumber is usually negligeable, so in a first approximation $w^2 \sim w_p^2$. This mean that laser radiation cannot propagate into the plasma above certain electron density This density called critical density and can be written like:

$$n_e = \frac{m_e w_L^2}{4\pi e^2} = 1.1 * 10^{21}\lambda^2 \text{ (1.19)}$$

Where m_e end e respectively mass and charge of electron λ is the wave length of the laser expressed in microns and n_e is presenting in cm^{-3} .

The low frequency is an ion acoustic wave The dispersion relation of this oscillation is $w=\pm kv_s$ where $v_s = \sqrt{(ZT_e + 3T_i/M}$ is ion sound velocity and $w<<w_p$

1.1.6 Parametric instabilities

One of the fundamental processes in of laser with fully ionize plasmas (corona region) is the parametric excitation of two new waves (parametric instabilities).Laser may excite plasma waves or other electromagnetics waves. In all case we have interaction with laser pumping two other waves, Parametric decay inwhere the phase matching conditions

$$w_0 = w_1 + w_2, \boldsymbol{k_0} = \boldsymbol{k_1} + \boldsymbol{k_2} \text{ (1.20)}$$

Are satisfied. Note that(w_0,$\boldsymbol{k_0}$) correspond to the incident laser, and (w_1,$\boldsymbol{k_1}$) and (w_2, $\boldsymbol{k_2}$)to the excited modes. The various modes of parametric instabilities that can develops on the nature of the excited model:

- ✓ Stimulated Raman Scattering (SRS). It involves scattering of the laser photon by an electron plasma wave. SRS may occur in subcritical plasma with a density ($n < {}^{n_{cr}}/_4$)
- ✓ Stimulated Brillion Scattering (SBR). It involves scattering of the laser photon by an ion-acoustic wave. SBS may occur in the whole volume of the undersense plasma ($n < n_{cr}$)
- ✓ Parametric decay instability (PDI). The laser photon decay into two plasma waves: one ion acoustic wave running inwards like the laser photon and one electron-plasma wave that runs outwards in opposite direction. PDI is an absorption process which may occur in a region close to the critical surface ($n \sim n_{cr}$)

- ✓ Two- plasmon decay (TPD) instability. The laser photon decay into two electron-plasma waves. Since both electron plasma wave has approximately a frequency w_p, this instability may occur at density $n \sim {}^{n_{cr}}/_{4}$.Direction of propagation of both electron plasma wave is symmetrical at 45 degree to both $\boldsymbol{k_0}$ and $\boldsymbol{v_{os}}$, where $\boldsymbol{v_{os}}$ is the oscillatory velocity of an electron in the large amplitude light wave.

Parametric instabilities can have negative effects in inertial fusion. When there is interaction between a laser and a plasma, it can lead to the scattering of light and the generation of populations of high-energy electrons. Two common types of instabilities that reduce the efficiency of laser energy coupling to the fusion target are Stimulated Raman Scattering (SRS) and Stimulated Brillouin Scattering (SBS). In SRS, some of the laser energy is scattered, while in SBS, the laser energy is converted into acoustic waves that can lead to energy loss. These instabilities result in a portion of the laser energy not reaching the dense part of the target, requiring higher power laser devices, which present technological challenges.

Laser light scattering also causes an uneven deposition of laser energy, resulting in an asymmetric implosion of the target. This can introduce nonuniformities on the target surface, which can serve as the initial conditions for the development of hydrodynamic instabilities during the implosion process.

Concerning the population of hot electrons, they are produced when a portion of the laser energy is converted into energy carried by an electron plasma wave. These high-energy electrons are generated by plasma waves through their interaction with electrons moving at the phase velocity of the wave. These electrons can become trapped in the high-amplitude plasma waves excited by parametric instabilities and subsequently accelerated to high energies. Due to their long mean free path, these hot electrons can penetrate into the target and preheat the shell, increasing its entropy. This preheating of the shell can hinder achieving high compression (high areal density) during the target implosion. In fact, the total target areal density is influenced by various factors and is related to the shell preheat.

$$\rho R({}^{mg}/_{cm^2}) \approx 2600[E_L\,(MJ)]^{\frac{1}{3}}\alpha^{-0.6} \quad (1.21)$$

Where E_L is the laser energy. Thus, achieving high compression requires keeping the shell entropy law that implies among others reducing the possible shell preheat.

1.2 MECHANISMS OF EMISSION OF X-RAY FROM PLASMA

1.2.1 Line thermal emission

Thermal radiation is the electromagnetic radiation emitted by a material due to its heat, and the characteristics of this radiation depend on the material's temperature. An example of thermal radiation is the infrared radiation emitted by a household heater or radiator. Even in extremely cold conditions, standing close to a blazing

campfire will make a person feel the radiating heat. When the heat generated by the movement of charges in a material, such as protons and electrons in ordinary matter, is converted into electromagnetic radiation, thermal radiation is produced.

The Earth is heated by solar radiation, which is thermal radiation from the Sun's extremely hot gases. Similarly, the Earth radiates heat, although at a much lower intensity due to its cooler temperature. The Earth's surface temperature is determined by the balance between heating from the Sun's thermal radiation and cooling from the Earth's own thermal radiation. Radiation is the only method of heat transfer that does not require a medium to conduct the heat. Radiant heat can be transferred from one surface to another with minimal heat absorbed between them. However, once the surfaces are heated, they can transfer heat to the surrounding environment through conduction or convection.

All objects with a temperature above absolute zero emit thermal radiation in a spectrum of wavelengths. The amount of radiation emitted by a black body at any one wavelength is described by the spectral black body emissive power distribution or Planck's Law. Thermal radiation field in the electromagnetic spectrum covers a range of wavelengths ~ 10^{-7}–10^{-4} m,i.e., in the visible and infrared regions [Hackford, 1960]

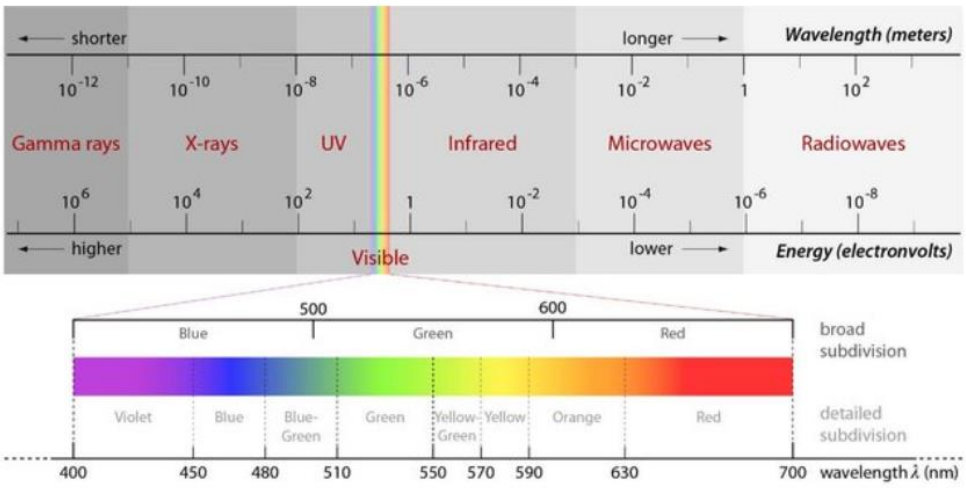

Fig1.2.1 Thermal emission spectrum [Geert,2017]

The visible part of the spectrum covers a wavelength of 0.40–0.76 um. The infrared region of the spectrum consists of a near-infrared region (0.76–25 um) and the far infrared region (25–1000 um). A main portion of the thermal radiation energy falls on the wavelength's region of 0.76–15 um, i.e., lies in the near infrared. Radiation in the visible region of the spectrum is significant only at very high temperatures.

Thermal radiation can be viewed as a surface phenomenon because thin surface layers (− 0.001 to 1 mm) on the body are involved in the radiative heat transfer.

1.2.2 Line emission induced by hot electrons (K-a)

When the hot electron collides an ion, the acquired energy can be sufficient to ionize the ion are release it even from the most inner shell of the atom characterized by the quantum number n=1, also called K-shell or 1s orbital. In this ionisation process the excited ion can decay down to a more stable state and filling-in the inner shell gap let by the excited electron with an outer shell one. The transition energy is either transmitted to another electron or emit a photon of the corresponding energy (radiative transition). There are a lot of different transitions for a given atom and each one concerns different transition states. The transition from the orbital 2p to 1s (L-shell to K-shell) is called K_α emission. It is called K_β for the 3p to 1s transmission (M-shell to K-shell). K_α transition are in fact allowed from two possible orbitals of the L-sell and when it occurs from $2p_{1/2}$ orbital, it called $K_{\alpha,1}$ and from $2p_{3/2}$ orbital it is call $K_{\alpha,2}$.

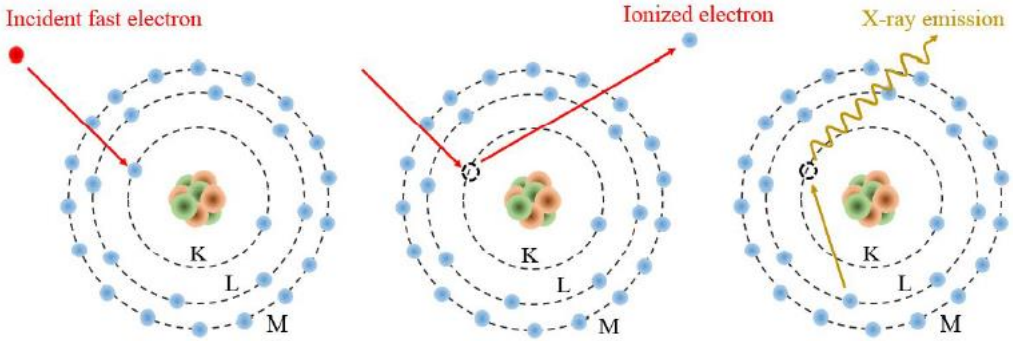

Fig1.2.2 Process of Kα emission caused by fast electron. Image taken from [Vaisseau, X. (2014)].

For instance, E_{K_α} = 8002 eV for copper, a material regularly utilized in the experiment. Only electrons whose kinetic energy is higher than B_K = 8996 eV are likely to cause this ionization. The electrons of the layer with a higher quantum number faster fill the gap that is thus created in layer K. In addition, a $2p_{1/2}$ or $2p_{3/2}$ L layer electron can fill this gap and produce a photon with an energy equal to the difference between the starting level E_L and the level of arrival E_K. In sum up, Figure 1.2.2 shows that if an input electron is given at least the ionization energy I_K, it can release a K shell electron. The gap is then filled by a transition from L to K emitting a photon of energy E_K - E_L. This latter X-ray fluorescence is called Kα emission in the case of a 2p to 1s transition (L-shell to K-shell). This emission is isotropic.

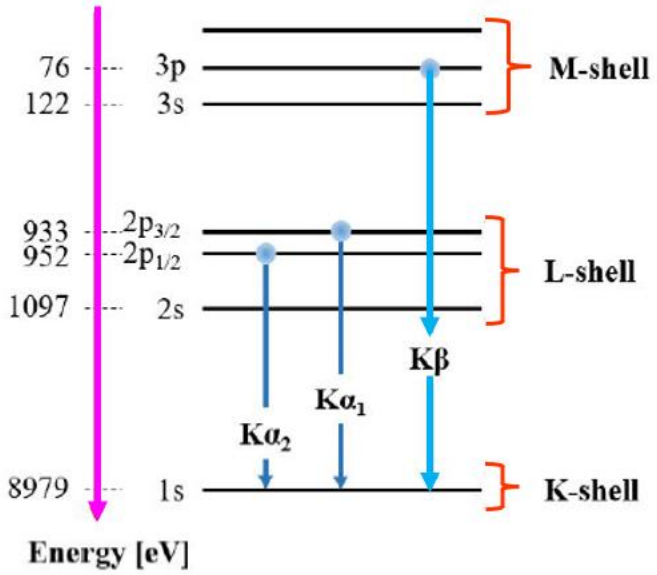

Fig 1.2.3 K-shell emission transitions for a cooper atom.

The energy of the Ka transition can be estimated using the empirical Moseley's [Moseley, 1913] for atoms of atomic number 3<Z<60. This model does not separate $K_{\alpha,1}$ emission from $K_{\alpha,2}$ one and is given by

$$E_{K_\alpha}[eV] = 10.206(Z-1)^2 \quad (1.22)$$

$K_{\alpha,1}$ and $K_{\alpha,2}$ emissions and provides an estimation with a 5 % error.

$K_{\alpha,}$ emission cross section

The K_α emission cross section can be expressed by the following:

$$\sigma_K = f_K \sigma_{ion} \quad (1.23)$$

With σ_{ion} the K_α ionization cross section and f_K the fluorescence yield. This latter term accounts for the fact that there is another relaxation mechanisms, the Auger electron emission. K-shell ionisation cross sections have been deeply studied experimentally and theoretically. The theoretical description for any element needs full quantum calculation. Additionally, it is difficult to apply simple expressions directly in numerical calculations. A lot of empirical laws based an fitting the experimental data have been presented. One of the best semi empirical formulas fitting the experimental data for $f_K(Z)$ is given by

$$f_K(Z) = \frac{[\sum_{i=0}^{3} a_i Z^i]^4}{1+[\sum_{i=0}^{3} a_i Z^i]^4} \quad (1.24)$$

Where

$$a_0 = 0.024 \pm 0.074$$

$$a_1 = 0.030 \pm 0.005$$

$$a_2 = (1.081 \pm 1.136)10^{-4}$$

$$a_3 = (-4.633 \pm 1.281)10^{-6} \text{ (1.25)}$$

The fluorescence yield function $f_K(Z)$ for elements of atomic number Z, $5 \leq Z \leq 99$. In contrast to the K_α emission process, which dominates for high Z elements, the Auger process is dominant for low Z elements.

According to the empirical model of Hombourger described in [Hombourger, 1998], the ionisation cross section σ_{ion} is written as

$$\sigma_{ion} = n_K \pi a_B^2 G_r \left(\frac{E_{Ry}}{I_K}\right)^{C_U} D_U \text{ (1.26)}$$

Where n_K is the number of electrons of the K-shell a_B is the first Bohr radius ($a_B = {\varepsilon_0 h^2}/{\pi m_e e^2}$), G_r is the relativistic factor of Grysinski (considering the relativistic effect in the incident electron motion) and is written as

$$G_r = \left(\frac{1+2J}{U+2J}\right)\left(\frac{U+J}{1+J}\right)^2 \left(\frac{(1+U)(U+2J)(1+J)^2}{J^2(1+2J)+U(U+2)(1+J)^2}\right)^{3/2} \text{(1.27)}$$

Where $J = ({mc^2}/{I_K})$ and $U = {E}/{I_K}$. Here E is the energy of the incident electron. D_U and C_U are two dimensionless factors depending on U where

$$D_U = \left(3.125 - \frac{4.172}{U} + \frac{1.877}{U^2}\right)\frac{\ln(U)}{U} \text{ (1.28)}$$

$$C_U = 2.0305 - \frac{0.316}{U} + \frac{0.1545}{U^2} \text{ (1.29)}$$

Examples of calculated ionisation cross section σ_{ion} as a function of incident x-ray photon energies.

<u>K_α photon number</u>

Let us consider a fast electron population description by an energy distribution function $f(E)$ propagation in a dense, thick medium with an ion density n_i.The number of emitted K_α photons can be written as follows:

$$N_\alpha = n_i \int_0^\infty f(E_0)\left(\int_{E_0}^0 f_K \sigma_K \left(\frac{dE}{ds}\right)^{-1} dE\right) dE_0 \text{ (1.30)}$$

With $N_e = \int_0^\infty f(E)dE$ the number of fast electrons and ${dE}/{ds}$.

$$\frac{dN_\alpha}{ds} = n_i f_K \int \sigma(v) f(v) dv \text{ (1.31)}$$

With v the relativistic electron speed. Even if the K_α radiation is completely isotropic so that photons are emitted with an equal probability in 4π steradian, K_α, diagnostics must be located as close as possible from the target axis due to the re-absorption of the generated line emissions during their propagation.

1.2.3 Bremsstrahlung emission

When a charged particle collides with another charged particle, it slows and emits electromagnetic radiation defined as bremsstrahlung. X-ray spectrum is

generated by this radiation. Another name for this is "braking radiation." Most of these charged particles are electrons and metal atomic nuclei.

The laser field causes the electrons to oscillate, and their energy is converted to thermal energy via electron-ion collision. The electron is free before and after the collision with the atoms, therefore there is no recombination. This process is a free-free electron process, and the mechanism is the opposite of what took place when a charged particle is decelerated by another charged particle, as seen in Fig 1.2.4 . The moving particle loses kinetic energy, which is converted to photons. Because of this, the method is also known as inverse bremsstrahlung. Collisional absorption is the most effective absorption method because the laser directly transfers energy to the electrons, which thermalize locally. Another approach, which will be covered later, includes coupling laser light into plasma waves to create suprastermal electrons, which can then go through the plasma and into unperturbed matter, where they thermalize.

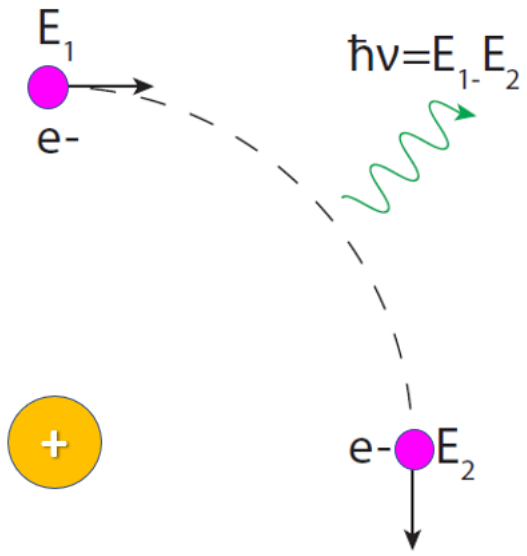

Fig 1.2.4 Bremsstrahlung process, showing the electron in pink and the ion in yellow. The ion-generated Coulomb contact causes the electron to decelerate, which produces a photon with energy equal to the electron's energy loss

Bremsstrahlung often has continuous spectrum and a decreasing energy, showing that it is a braking radiation rather than an atomic transition. It also doesnt have emission lines. Because it has a lot lower intensity than K_α radiation, it is harder to detect. When that happens, it will have a privileged direction because it comes from the movement of the electron similar to the electron beam's rate. The Bremsstrahlung spectrum for relativistic electrons usually numerically calculated, then tabulated. It is also more marked for the fastest electrons (> 1 MeV) emits more energetic photons. The energy distribution of the incident electrons can theoretically be estimated using knowledge of the bremsstrahlung spectrum. For a given energy, the angular distribution has a maximum emission. For very fast electrons (> 10 MeV), this characteristic angle is on the order of 1°, while for slower electrons (> 1

MeV), it is close to 20̊. We observe that the bremsstrahlung is directed mainly in the direction of the electron beam. More specifically, the average emission angle of a bremsstrahlung photon, relative to the initial direction of the electron, is proportional to $1/\gamma$.

1.3 SHOCK GENERATION AND SHOCK PROPAGATION

A shock wave is a discontinuity in density, velocity and temperatures that propagates with velocities greater than the sound speed of the lower density plasma lying ahead.

Let's consider a shock wave propagating at velocity D in an unperturbed fluid with the density ρ_0, the pressure P_0, the internal energy per unit mass ε_0 and the fluid velocity is u_0. The hydrodynamic variables behind the shock front are ρ_1, P_1, ε_1 and u_1. In the reference frame of shock front, the upstream velocity (in the unperturbed fluid) is $u_0 - D$ and the downstream velocity (in the shocked fluid) is $u_1 - D$. From the upstream fluid, the mass flow going in the shock front though a surface area S is $m_0 = \rho_0(u_0 - D)S$. In the downstream fluid, the mass flow getting out of the shock front is $m_1 = \rho_1(u_1 - D)S$. Due to the conservation of mass $m_1 = m_0$, which possible to write as

$$\rho_0(u_0 - D) = \rho_1(u_1 - D). \quad (1.32)$$

The momentums of the upstream and downstream mass flow are $m_0(u_0 - D)$ and $m_1(u_1 - D)$, respectively. This variation of momentum is due to the force acting on the fluid, which in this case in the pressure difference between the upstream and downstream fluid $S(P_1 - P_0)$ following Newton's law. Separating the upstream quantity from the downstream one, the conservation of momentum writes

$$P_0 + \rho_0(u_0 - D)^2 = P_1 + \rho_1(u_1 - D)^2 \quad (1.33)$$

The total energy carried by the upstream mass flow is the sum of the kinetic energy $m_0(u_0 - D)^2/2$ and the internal energy $m_0\varepsilon_0$. The same way, the downstream total energy flow is $m_1(u_1 - D)^2/2 + m_1\varepsilon_1$. This change in total energy is due to the difference in the work of pressure forces between the upstream and downstream fluids. This work per unit time is $-[P_1(u_1 - D)S - P_0(u_0 - D)S]$. The conservation of energy can be written

$$\frac{P_1}{\rho_1} + \frac{(u_1 - D)^2}{2} + \varepsilon_1 = \frac{P_0}{\rho_0} + \frac{(u_0 - D)^2}{2} + \varepsilon_0 \quad (1.34)$$

The equation up call Rankine-Hugoniot. The Rankine-Hugoniot equations are equations of conservation of mass, momentum, and energy though a shock front

$$\varepsilon_1 - \varepsilon_0 = \frac{1}{2}(P_1 + P_0)\left(\frac{1}{\rho_1} - \frac{1}{\rho_0}\right) \quad (1.35)$$

This expression is especially useful since it does not include the fluid and shock velocities.

The Hugoniot curve is the set of all downstream variable and shock velocity combinations for a fluid in a known hydrodynamic state that verify the Rankine-

Hugoniot equations and the fluid's equation of state. As a matter of fact, using the upstream variables P_0, u_0, ε_0 and D. The fluid equation of state and the three Rankine-Hugoniot equations form a system. Of four equations with five unknowns: ε_1, P_1, u_1, D, and the first unknown. Hence, there is this system has an endless number of solutions. However, all other variables are fixed if one is determined.

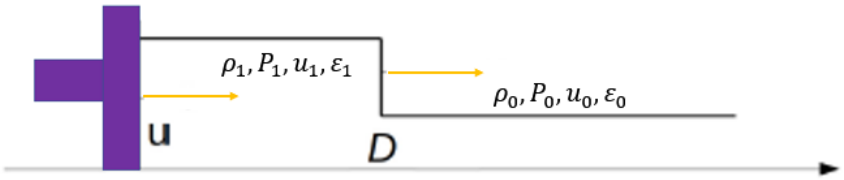

Fig1.3.1 Plot representation of shock wave propagation. The wave is produced by a piston that moves into the gas with constant velocity u. The gas state is described by the hydrodynamic quantities ρ_1; P_1 ; u_1; ε_1 ", subscripted by "0" for the upstream quantities and by "1" for the downstream quantities. D is the shock velocity.

In the case of an ideal gas, the downstream variables and the shock velocity can then be expressed as a function of the upstream variables and one downstream variable alone, the pressure P_1 for example

$$\frac{\rho_1}{\rho_0} = \frac{(\Upsilon+1)P_1+(\Upsilon-1)P_0}{(\Upsilon-1)P_1+(\Upsilon+1)P_0} \quad (1.36)$$

$$\frac{\varepsilon_1}{\varepsilon_0} = \frac{P_1}{P_0} \times \frac{\rho_0}{\rho_1} = \frac{P_1}{P_0} \times \frac{(\Upsilon+1)P_1+(\Upsilon-1)P_0}{(\Upsilon-1)P_1+(\Upsilon+1)P_0} \quad (1.37)$$

$$D = u_0 \pm \sqrt{\frac{(\Upsilon+1)P_1+(\Upsilon-1)P_0}{2\rho_0}} \quad (1.38)$$

$$u_1 = u_0 \pm \sqrt{\frac{2(P_1-P_0)^2}{\rho_0[(\Upsilon+1)P_1+(\Upsilon-1)P_0]}} \quad (1.39)$$

The ± sign in the expression of the shock velocity *D* and of the downstream fluid velocity u_1 depends on if the shock propagates in the same direction as the upstream fluid velocity (case with the sign +) or in the opposite direction (in this case the sign is −).

In the strong shock limit, where the pressure behind the wave front is much higher than the initial pressure, the density dose does not increase with increasing strength but approaches certain finite value [Zel'dovich and Raizer, 2002]. The limiting density or volume ratio across the shock ave is a function of the specific heat ratio only and is given by

$$\frac{\rho_1}{\rho_0} = \frac{\Upsilon+1}{\Upsilon-1} \quad (1.40)$$

The maximum compression limit and the Hugoniot curve of a perfect gas' asymptotic behaviour are shown in fig1.3.1

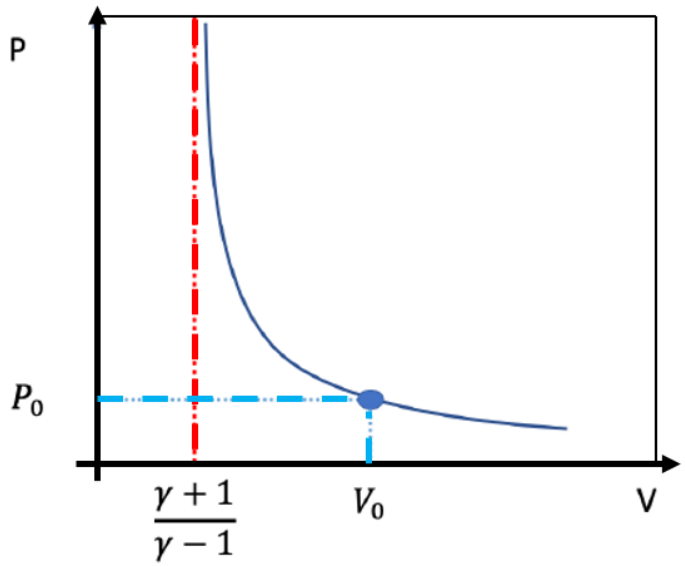

Fig.1.3.2 Hugoniot curve of a perfect gas

An important quantity related to the shock dynamics is the entropy. For a perfect gas with constant specific heat the entropy is given by the formula:

$$S = c_v \ln (pV^{\Upsilon}) \quad (1.41)$$

where V is the specific volume of the gas. As such, the divergence between the entropy on each side of the shock front becomes:

$$S_1 - S_0 = c_v \ln\left(\frac{p_1 V_1^{\Upsilon}}{p_0 V_0^{\Upsilon}}\right) = c_v \ln\left\{\frac{p_1}{p_0}\left[\frac{(\Upsilon-1)\left({}^{p_1}/_{p_0}\right)+(\Upsilon+1)}{(\Upsilon+1)\left({}^{p_1}/_{p_0}\right)+(\Upsilon-1)}\right]^{\Upsilon}\right\} \quad (1.42)$$

For $p_1 \to p_0$the expression leads to$S_1 \cong S_0$, while as the shock strength (p_1/p_0) increases also $S_1 - S_0$, increases monotonically, approaching inanity as $p_1/p_0 \to \infty$. The increase of entropy indicates that a shock wave is a dissipative irreversible phenomenon.

Chapter 2: Measurement of bremsstrahlung X-rays emitted by hot electrons with BSC

2.1 GENERAL DESCRIPTION OF BSC

Fast electrons exhibit an intense and continuous emission of hard X-rays as they propagate. The emitted spectrum of X-rays is dependent on the kinetic energy of the electrons, thus allowing the emitted photon spectrum to be related to the distribution of fast electrons. Various diagnostics have been employed to characterize the average energy of hot electrons and assess the conversion efficiency from laser light to electron beam energy. One such diagnostic discussed in the chapter is the Bremsstrahlung cannon (BSC).The typical design of a BSC involves a stack of detectors, known as imaging plates (IPs), which are separated by filters of varying materials and thicknesses. These filters are specifically chosen and optimized to detect photons based on the expected photon distribution. Monte Carlo simulations are employed to estimate the signal detected by each imaging plate and to optimize the configuration of the filters in the Bremsstrahlung cannon stack.

In these simulations, the Monte Carlo code GEANT4 with the Penelope library is utilized. The simulation setup incorporates the detailed design of the BSC and the parameters of the target to accurately model the photon interactions. By running these simulations, the signal response in each imaging plate and the optimal arrangement of filters can be determined for the Bremsstrahlung cannon.The example of design of Bremsstrahlung spectrometer is shown in Fig 2.1.1

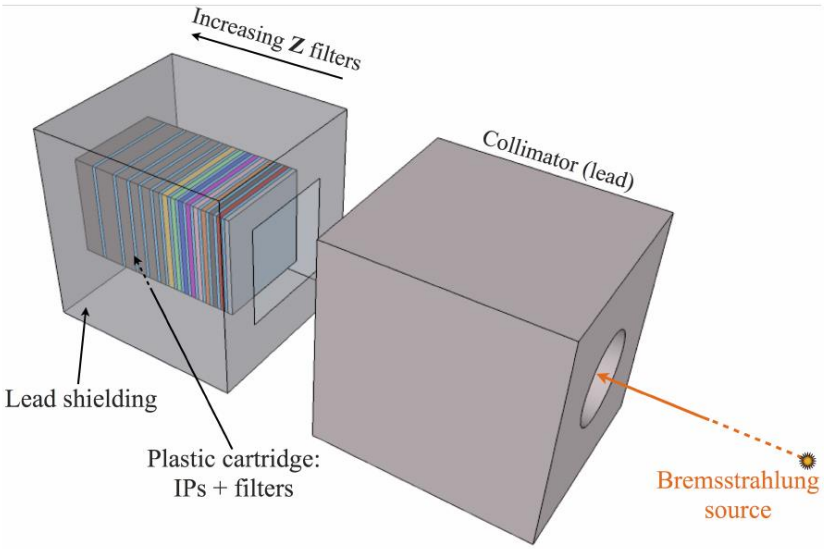

Fig 2.1.1 Schematic of the BC cannon

The lead shield is utilized to protect the imaging plates (IPs) from scattered radiation. It serves as a barrier to minimize the impact of radiation that is not directly relevant to the measurement. Additionally, a collimator is employed to effectively collimate the photon beam entering the stack and shield the system from background radiation.

To further enhance the measurement accuracy and minimize unwanted signal contributions, thick mylar foils with a thickness of 250um are utilized in each filter. These foils help reduce the influence of secondary electrons generated within the stack, ensuring that the measured signal primarily represents the desired photon interaction.

The imaging plates (IPs) used in the BSC function as detectors. They were initially commercialized by Fuji in the 1980s for medical purposes and X-ray imaging. Over time, they found application in detecting particle beams accelerated by lasers, as documented in studies such as those by [Maddox et al,2011; Lamoureux et al,2006; Chen et al, 2008; Boutoux et al,2016].

The IPs consist of layers composed of different materials. One of these layers records the dose deposited by secondary electrons generated by photons. Fujifilm has produced five different types of IPs, commonly referred to as MR, SR, and TR. Table 2.1 provides information on the atomic composition, densities, and thickness of these different IP types. It is worth noting that the TR IP does not include a protective layer. IPs are flexible and can be reusable in various experiments and measurements.

Layer	**SR**	**MS**	**TR**
PROTECTIVE			
Composition	C_2H_2O	C_2H_2O	No layer
Density (g/cm^3)	1.273	1.66	0
Thickness(µm)	6	9	0
SENSITIVE			
Composition	BaFBr:Eu	$BaFBr_{0.85}I_{0.15}$:Eu	$BaFBr_{0.85}I_{0.15}$:Eu
Density (g/cm^3)	3.1	3.31	2.85
Thickness(µm)	120	115	50
SUPPORT			
Composition	C_2H_2O		
Density (g/cm^3)	1.237	1.66	1.66
Thickness(µm)	188	190	250
MAGNETIC			
Composition	$ZnMn_2Fe_5NO_{40}H_{15}C_{10}$		
Density (g/cm^3)	3.1	2.77	2.77
Thickness(µm)	160	160	160

Table 2.1Atomic compositions, densities, and thicknesses of the various layers of SR, MS and TR IPs [Boutoux et al ,2016].

After the shot, the imaging plates (IPs) are transferred to a scanner for the digitalization of the detected signal. The reading process involves the use of a laser light in the red color range, which induces the deexcitation of the *BaFBr* material present in the IP. As a result, the *BaFBr* emits a luminescent blue light, which is detected by the scanner.

Once the readout process is complete, the imaging plate is placed under white light to erase any residual signal. To protect the IP and preserve the signal stored within it, it is essential to transport the IP in a box that shields it from visible light. This protective box helps maintain the integrity of the signal recorded on the IP until it is ready for further analysis or storage.

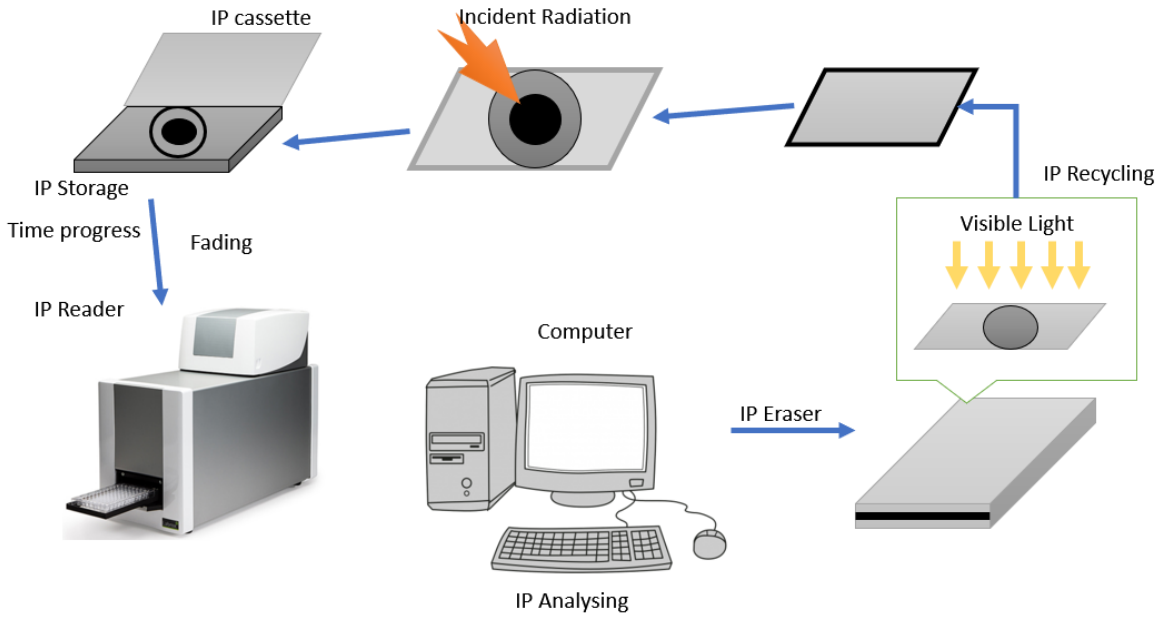

Fig 2.1.2 Scanning process of IP signal.

The scanner is responsible for reading out the imaging plates (IPs). The surface of the IP is divided into pixels, and the scanner scans each pixel to capture the signal. During the scanning process, the scanner emits photons that interact with the "active" layer of the IP. The emitted photons are then detected, and the detection signal is proportional to the number of photons emitted through the pixel.

The scanner generates a matrix containing a numerical value for each pixel named Quantum Level (Q_L). The response of scanner is logarithmic. The Q_L dependence on the number detected luminescence photons is logarithm. Values in Q_L are converted into PSL using the function below

$$PSL = \left(\frac{Res}{100}\right)^2 * \frac{4000}{S} * 10^{L*\left(\frac{Q_L}{2^D-1}-\frac{1}{2}\right)} \quad (2.1)$$

- ✓ PSL : photoluminescence photon number read in pixel;
- ✓ Res: size of pixel in um;
- ✓ S: sensitivity (1000, 4000, 10000);
- ✓ L: latitude(4,5);

- ✓ D: read-out dynamic range (8 bits or 16 bits);
- ✓ Q_L : numerical value of pixel (between 0 and 2^D-1).

The time shift between the irradiation of the imaging plate (IP) and the scanning process is important to measure in order to estimate the signal loss caused by the fading phenomenon. Fading refers to the spontaneous recombination of electron-hole pairs over time, which leads to a decrease in the detected signal. To correct for signal losses due to fading, it is necessary to have knowledge of the fading function specific to the type of imaging plate being used.

The fading phenomenon should be taken into account because there is always a period of time between when the IP is placed in the scanner and when the readout procedure is completed. The extent of fading depends on factors such as the type of imaging plate and the surrounding temperature. By understanding the fading characteristics and incorporating the fading function into the analysis, corrections can be applied to compensate for signal losses and ensure accurate results. In fig 2.1.3

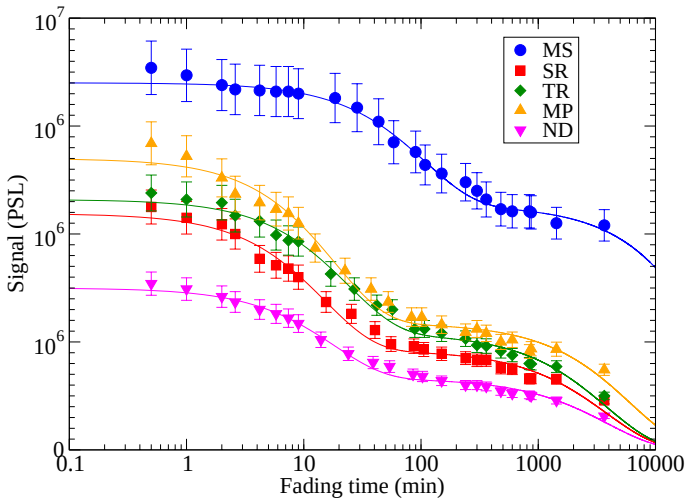

Fig 2.1.3 Fading of the image plates as a function of time at 20 °Con the Fuji FLA3000 IP scanner [Boutoux et al, 2015]

Following the fading characteristics, the recommended waiting time is not more than 60 minutes. The waiting time was around 20-30 minutes in experimental campaigns presented in this manuscript.

2.2 DESCRIPTION OF EASY SEMI-ANALYTICAL METHOD TO ESTIMATE HOT ELECTRON TEMPERATURE

Bremsstrahlung spectra are usually assumed to be exponential corresponding to a hot electron Maxwellian distribution. The slope of this exponential is taken as a representative of the temperature of hot electrons. Easy module for estimating hot electron temperature is described in this chapter.

The basic idea of calculated file is that the transmission of materials composing the cannon filer is well known. Therefore, there is linear relation between the spectrum of the photons and the response of the detector. Let's assume a photon spectrum I(E) characterized by N energy bins coming to the bremsstrahlung cannon. The number of PSL photons obtained after scanning the IP is given by equations:

$$F^1(E_1) = T^1(E_k) * R_{IP}(E_k)$$
$$F^1(E_1) = T^1(E_k) * T^2(E_k) * R_{IP}(E_k)$$
$$\vdots$$
$$F^1(E_1) = T^1(E_k) * T^2(E_k) \dots T^i(E_k) * R_{IP}(E_k) \quad (2.2)$$

The number of F is fixed by the number of filters composing the bremsstrahlung cannon.

The total PSL value is calculated using formula

$$PSL = \int T(E_k) * R(E_k) * I(E_k) dE \quad (2.3),$$

where E_k-photon energy

T(E)-transmission of an incident photon of energy E_k;

R(E)-response function ;

I(E)-number of photons with energy E_k.

IP response data are based on the article of Meadowcroft et al. and Maddox et al. In this article [Meadowcrof et al,2008; Maddox et al.2011] the GEANT4 Monte Carlo simulation was done to model the absolute sensitivity curve for imagine plate MS, SR and TR. Table#2.1 were used to implemented geometry and atomic composition of different types of IP. Energy loss E_{dep} was calculated with the sensitive layer of each IP for different photon energies. It was assumed that in PSL signal is proportional to the energy loss E_{dep} within the sensitive layer of imagine plate,

$$PSL = \alpha * E_{dep}. \quad (2.4)$$

Here the α-coefficient reproduces experimental point within error bar over the whole energy range for each type of IP by a least square minimization technique. The model didn't take into account the imaging plate response below 10 keV. Simulation shows a maximum sensitivity for photons below 100keV energy. For energies about 2keV, MS IPs are more sensitive than SR and TR are more sensitive because protective layer is absent. [Boutoux et al,2016; T. Bonnet et al 2013]

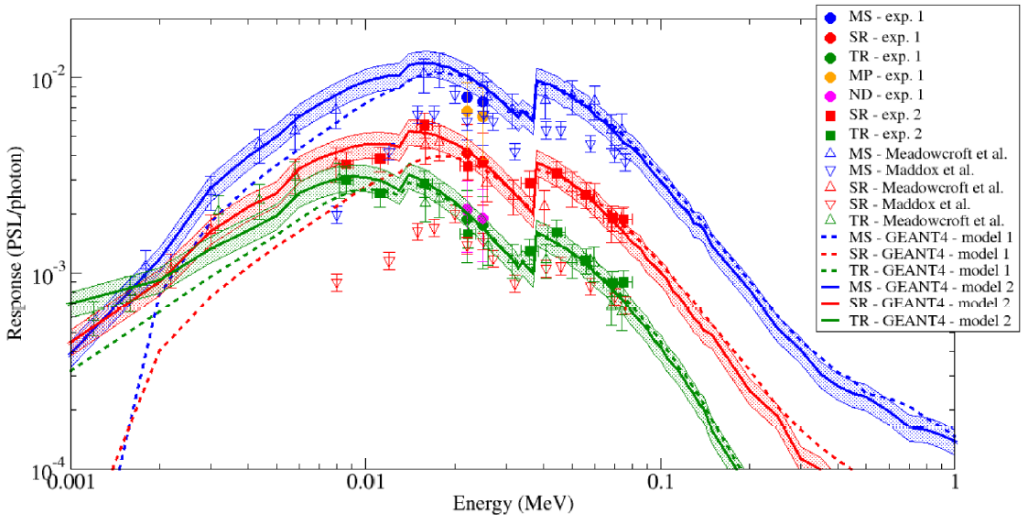

Fig 2.2.1 Measured sensitivities for each type of IP (full symbols) compared to existing studies [Boutoux et al,2016; Meadowcroft et al,2008 and Maddox et al, 2011. (empty symbols).

We used data of IP response in our calculation file for the different type of IP. Transmission is calculated using formula

$$T(E) = e^{-\mu x \rho} (2.5)$$

Where x is the thickness of the filter. NIST online databased was used for mass attenuation coefficients μ, ρ is density. The transmission for the cannon's filters taken from the NIST database and plotted in Fig 2.2.2 (For the bremsstrahlung cannon used in Salamanca experimental campaign). We take into account the each IP transmission. Imaging plate transmission was calculated taken into account each layer of IP in assumption that in energy range larger than 50 keV the contribution of IP transmission is neglected, and transmission value is 1.

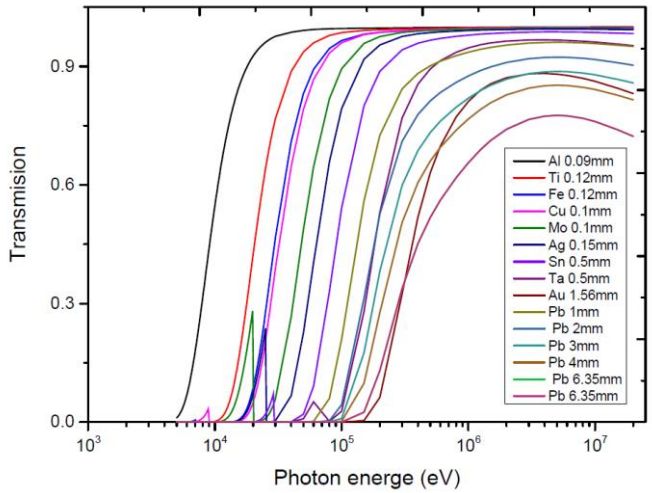

Fig 2.2.2 Transmission of the materials composing the bremsstrahlung cannon filters

The mathematical function used into calculating file is chose by the following steps:

- ✓ The photon spectrum is chosen by the user (mathematical function as well as photon energy range).
- ✓ The photon spectrum is injected into the file and the PSL value is calculated

- ✓ The difference between the result and the experimental spectrum is evaluated, and the initial photon spectrum is modified in order to decrease the difference until a good agreement is reached with experimental result.

The exponential function provides the best agreement with experimental results

$$I(E_k) = \alpha \exp\left(-\frac{E}{T}\right) \quad (2.6)$$

The actuality of this analytical method is presented in 2.4 part. It was compered and confirmed with Monte-Carlo simulations.

2.3 DESCRIPTION OF MONTE-CARLO SIMULATION TO PREDICT BREMSSTRAHLUNG SPECTRA

GEANT4 is a powerful and widely used open-source code for Monte Carlo simulations. It was first released in 1998 and has since undergone numerous updates and expansions. The framework is developed and maintained by a collaboration of scientists and software engineers from around the world.

The primary purpose of GEANT4 is to simulate the propagation of particles through matter. It is specifically designed for calculating the behavior of particles as they interact with materials, allowing for the modeling of complex physical processes. The code is implemented in the C++ programming language and leverages object-oriented technology to provide a comprehensive range of functionality.

GEANT4 offers a rich set of features including tracking, geometry modeling, physics models, and hit handling. Its versatility makes it suitable for a wide range of applications in various scientific fields. For example, it is extensively used in high-energy physics experiments at the Large Hadron Collider (LHC) and plays a crucial role in the design of spacecraft by organizations such as the European Space Agency (ESA) and the National Aeronautics and Space Administration (NASA).

By utilizing GEANT4, researchers can perform detailed Monte Carlo simulations to study particle interactions, evaluate radiation doses, optimize detector designs, and investigate various aspects of particle propagation through matter. Its open-source nature allows for community collaboration, further development, and customization to suit specific simulation needs. [GEANT4 manual 11.0,2021].

For define the atomic composition of matter, the physical process and geometry of detector are many classes in GEANT4. The physical prosses of the interaction of particles with matter are described by different library, like:

- PENELOPE library (PENetration and Energy Loss of Positrons and Electrons). This library is used for the low -energy physics and treats the EM interaction of electrons and photons in the energy range between 250 eV to 1 GeV
- EM OPT3 is used for tracking particles which interact electromagnetically without magnetic field

- Livermore library based on the evaluated electrons, photons and atomic libraries
- EM-STD, multipurposed libraries
- EM OPT1, done for analysis of Compact Muon Solenoid in TeV ranges and specific detector materials.

Deconvolving the electron spectrum from the measured bremsstrahlung spectrum can indeed be a complex task that often requires the use of Monte Carlo numerical simulations. The process involves several steps to accurately predict the bremsstrahlung spectra and obtain the electron spectrum.

First, the electron spectrum is injected into the target material, leading to the generation of bremsstrahlung X-ray emission through collisions with the target ions. To predict the bremsstrahlung spectra, a comprehensive model of the experimental setup is constructed, including all filters, imaging plates (IPs), and the spectrometer geometry. The filters' thicknesses and compositions need to be accurately reconstructed in the simulation.

The layers of the imaging plates consist of specific materials, as listed in Table #1.1. The energy loss of particles passing through each active layer needs to be calculated. This can be achieved using the tools available in GEANT4, which allows for the accurate estimation of energy deposition.

In the next step, monochromatic X-ray beams are injected into the simulated bremsstrahlung cannon. Determining the number of particles to be used in the simulation is a general challenge in Monte Carlo methods. Sufficiently high numbers of particles are required to obtain reliable results. However, the number of particles should be optimized to strike a balance between computational time and statistical significance. Conducting several test runs can help identify the optimum number of particles for the simulation.

During the simulation, the energy deposition in the active layer of each imaging plate is compared with the measured value of photo-stimulated luminescence (PSL) obtained during the experimental measurements. This comparison helps validate the simulation results and ensure consistency with the experimental data.

By following these steps and optimizing the simulation parameters, researchers can obtain insights into the electron spectrum by deconvolving it from the measured bremsstrahlung spectra.

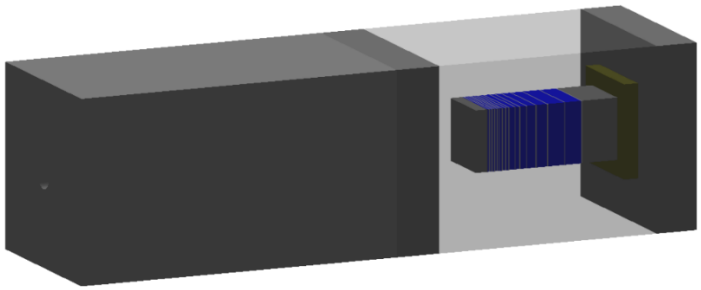

Fig2.3.1 Bremsstrahlung cannon model done in GEANT4 code.

2.4 RESULTS OBTAINED

GENERATION OF TRANSIENT VERY STRONG SHOCKS BY FS-LASERS

The experiment was designed for and performed at the VEGA II system at CLPU in November 2018. The experimental campaign was prepared and performed in collaboration with University of Bordeaux, Centre Lasers Intenses et Applications (CELIA) France, TATA Institute of Fundamental Research, Mumbai, India CLPU (Centro de Laseres Pulsados), Spain, ENEA, Italy, MEPHi, Russia.

The described experimental campaign conducted at the CLPU VEGA-II laser facility focused on investigating the dynamics of shock waves generated by fs-laser irradiation through the energy deposition from hot electrons. The short duration of the laser pulse results in a blast wave instead of a sustained pressure. The experiment involved irradiating solid-density targets of different materials and thicknesses, and the formation and propagation of the blast wave were characterized using various diagnostics.

Several diagnostics were employed to provide a comprehensive understanding of the process. X-ray emission was detected using a bremsstrahlung cannon, Kirkpatrick-Baez, and GEMPix detector. Electron spectrometers were utilized to gather information about the temperature of hot electrons. Optical diagnostics, such as shock chronometry, provided insights into the blast wave's propagation within the target material. Doppler reflectometry was employed to examine the state of the target's rear surface.

Characterizing hot electrons generated in laser-plasma interactions is crucial for Inertial Confinement Fusion and the study of laser-driven radiation and particle sources. One method for characterizing hot electrons is analyzing the emitted hard X-ray spectrum, known as bremsstrahlung emission. The emitted photon spectrum is related to the kinetic energy distribution of the fast electrons. The "bremsstrahlung cannon" (BSC) diagnostic, consisting of a stack of detectors (imaging plates) separated by filters of different materials and thicknesses, is used to analyze the emitted hard X-ray spectrum.

Bremsstrahlung spectra are often assumed to be exponential, corresponding to a Maxwellian distribution of hot electrons. The slope of this exponential can be used as a representative of the hot electron temperature. In this work, a semi-

analytical model is described for estimating the hot electron temperature. The model takes into account the filter transmission and imaging plate sensitivity. The method was applied to analyse data from experimental campaigns conducted at various large-scale laser facilities, including Vega at CLPU, VULCAN at RAL, and Phelix at GSI. The obtained results were compared to Monte Carlo simulations performed using the GEANT4 code with the Penelope library.

Preliminary experimental results confirm the generation of a blast wave that is initially strong but rapidly decays over time, consistent with the predictions made by hydrodynamic and particle-in-cell simulations. These findings contribute to the understanding of extreme pressure conditions and have implications for applications such as shock ignition in inertial confinement fusionEGA laser gool of experiment

Main system VEGA consists in a 30 fs pulse delivered in three different arms of 20 TW (VEGA I), 200 TW (VEGA II) and 1 PW (VEGA III).

- ✓ VEGA-I: 800nm central wavelength, 600mJ energy per pulse, 30fs of pulse duration and can operate up to 10Hz. VEGA-I beam diameter at the exit of the compressor is 3.5cm.
- ✓ VEGA-II: 800nm central wavelength, 6J energy per pulse, 30fs of pulse duration and can operate up to 10Hz. The beam diameter of VEGA-II at the exit of the compressor is 10cm.
- ✓ VEGA-III: 800nm central wavelength, 30J energy per pulse, 30fs of pulse duration and can operate up to 1Hz. VEGA-III beam diameter is more than twice bigger than VEGA-IIl with a size at the exit of the compressor of 25cm.

The aim of the facility is to serve the scientific community and industry by providing access to high power lasers as well as advice through collaborative research. CLPU is an open facility to national and international users.

VEGA-2 is a laser facility at Centro de Laseres Pulsados (CLPU) in Salamanca (Spain). The laser works with the focal spot on target which can range from few μm to tens of μm. The laser works with the parameters which can be founded in a table 2.2 below .

Wavelength	800nm
Pulse duration	30fs
Pulse energy	6J
Pulse intensity	10^{19}W/cm2
Contrast	3 10^{-10}

Table 2.2 VEGA-2 laser parameters

2.4.1 Goal of the experiment

During our experimental campaign, it worked at a power about E_l~ 3J for pulse duration between 29 and 33 fs and focal spot sizes between 20 to 24 μm. The estimated laser intensity was I ~ $4 \cdot 10^{19}$W/cm^2. The repetition rate is 1 shot every 1-2 minutes.

The goals of the experiment were:

- 1)To generate strong shock in solid density matter (P >100 Mbar at initial times) is creating WDM (Warm Dense Matter) states;
- 2) To study the dynamics of a blast wave travelling in the solid density material;
- 3) To characterize the generation and energy deposition from hot electrons and the expansion of the target;
- 4) Measuring the temperature of warm dense matter (WDM).

Experimental design

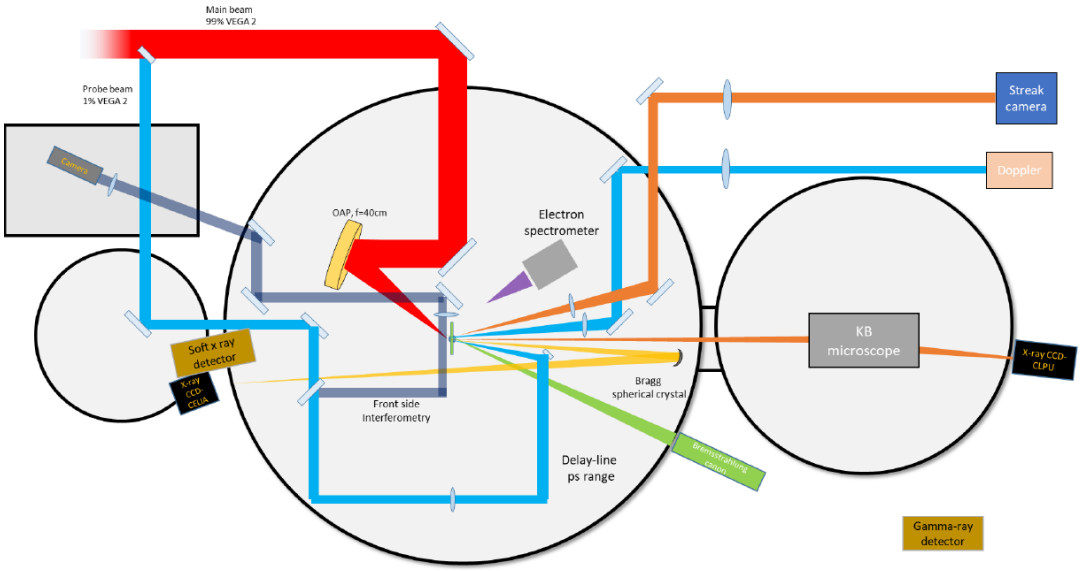

Figure 2.4.1 A schematic layout of the experimental set-up.

2.4.2 Targetry

One of the advantages of the high repetition rate (HRR) laser systems is the possibility to get a lot of data for the statistical study without breaking the vacuum of the interaction chamber. In most high energy laser single shot systems, the target is changed between the shots. In contrast, HHR system require to use a different type of targets that allows fielding a large number of targets inside one target holder. To bring the targets to TCC one can move the X-Y-Z motors of the target holder. Therefore, the target holder is motorized in height, lateral and focal directions with respect to the laser focus position – TCC. Target holder design which was used in the performed experimental campaign can produce 100 shots without breaking the vacuum and is shown in Fig2.4.2

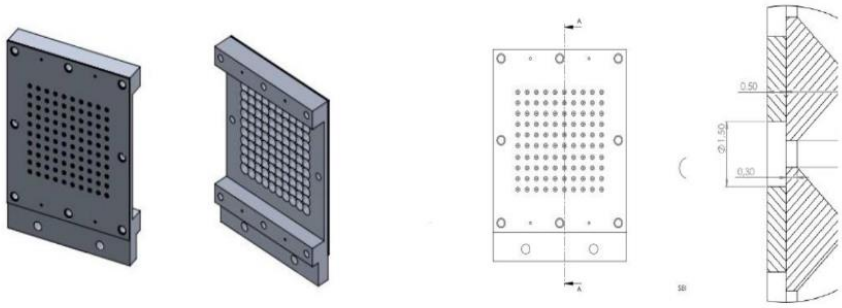

Figure 2.4.2 Target holder design.

As a targets were used simple Al foils, double layer foils Al/Ti and CH target with tracer layer of Ti. Foils size are 25mm x 22mm.

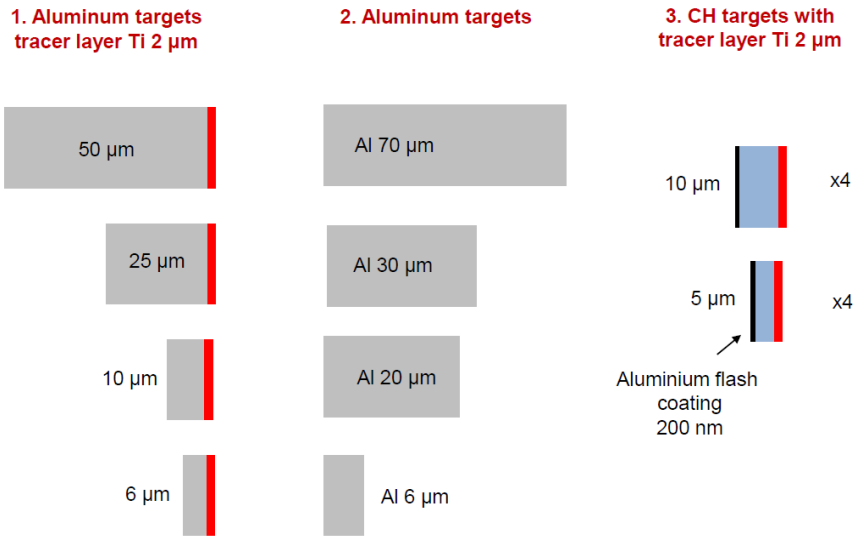

Fig 2.4.3. Targets specification

2.4.3 Result obtained

During experimental campaign set of diagnostics were used: shock chronometry (SOP) for characterize the blast wave, doppler spectroscopy for measured velocity of preheated target in to the rear side, Bremsstrahlung cannon and electron spectrometer to characterize of hot electrons in a front side of the target and KB microscopy (detecting K_α radiation), ϒ-ray and soft X-ray detectors in a rear side of the target.

SOP. A streak camera is a device capable of diagnosing these fast phenomena.

It delivers information about the intensity of a collected light signal as a function of time (over a window that can typically range from 0.55 ns to 1 ms) and of one spatial

dimension. We used streak camera with photocathode S20 in experiment. 400-700BG38 filters was applied before SOP. Magnification was 10. Total path distance was 3190 mm. Set up of SOP is shown in figure 2.4.4

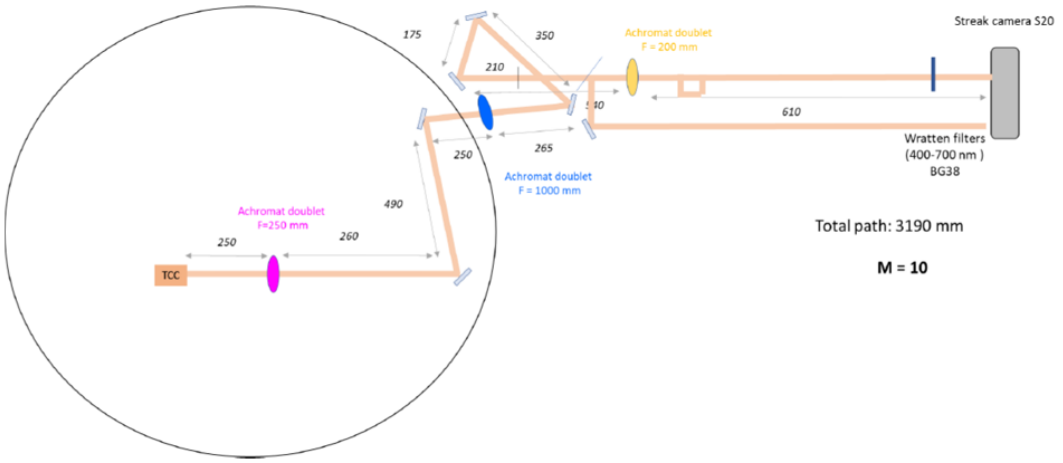

Fig 2.4.4 Set up of the SOP in the present experimental campaing. Magnification is 10, full distance from TCC to the SOP is 3190mm

Fig 2.4.5 shows a sample image (right) and the coresponding temporal prothil (left) of the emission from the rear side of 50um Al thick target rear side records by the streak camera. Time flows up to down, temporal scale was 10 ns. The temporal profile image by arrow show reagion with peak and "bump" which coresponds to shock crietion and shock break out time.The shock velosity can be astimatid by formula $D_{exp} = {}^{d}/_{\tau_{exp}}$ (2.7)' where τ_{exp} is experimental shock breack out time. $D_{exp} \approx 8{,}5\ km/s$ was founded to compere with sounds speed in Al $v_s = 6.4 km/s$. Presence of supersonic wave is an indication of shock criteria.

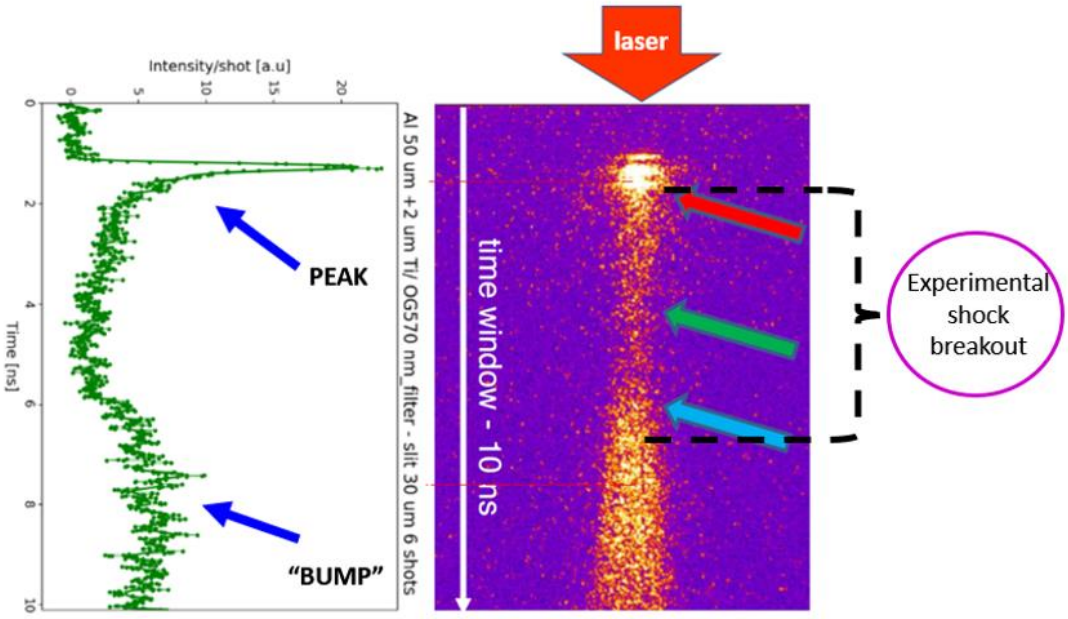

Fig 2.4.5 Creation of the shock detected in streak signal (SOP) (time window is 10 ns) in a AL target with thickness 50 um an 2 um Ti layer. Red arrow shows rapid

emotion by green arrow presents thermal decay; blue arrow represents position of the thermal emission. Experimental shock breaks out region marks by black dash line.

In a fig 2.4.6 shows the interpolation of shots with AL target with different thicknesses (25,50,70um). Shock velocity according to this interpolation is 8.8km/s with compatible with our previous results and prove presents of the shock wave creation.

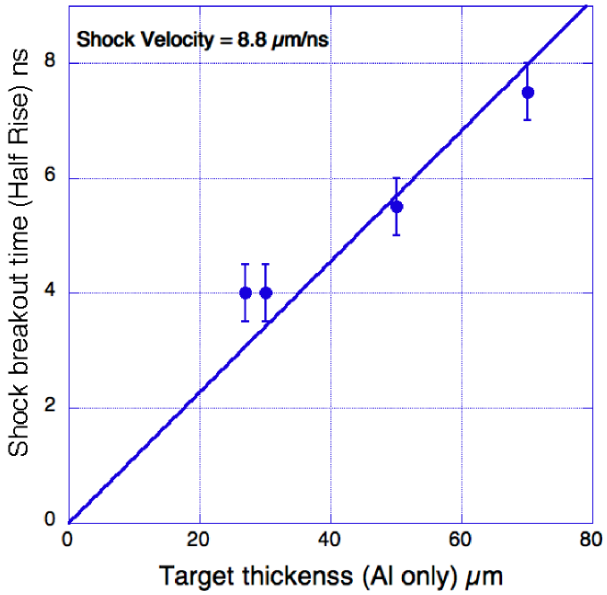

Fig 2.4.6 Interpolation of the shock break out time and different target thicknesses

We used Time Resolved Spectrometry (Doppler velocimetry) to measure the motion of the rear side of the target at early times under the influence of hot electron preheating. Set up of diagnostics is presented in a fig.2.4.7 Probe parameter central wavelength is 400um, pulse width is 75 fs and probe focal spot (FWHM) is 70um.

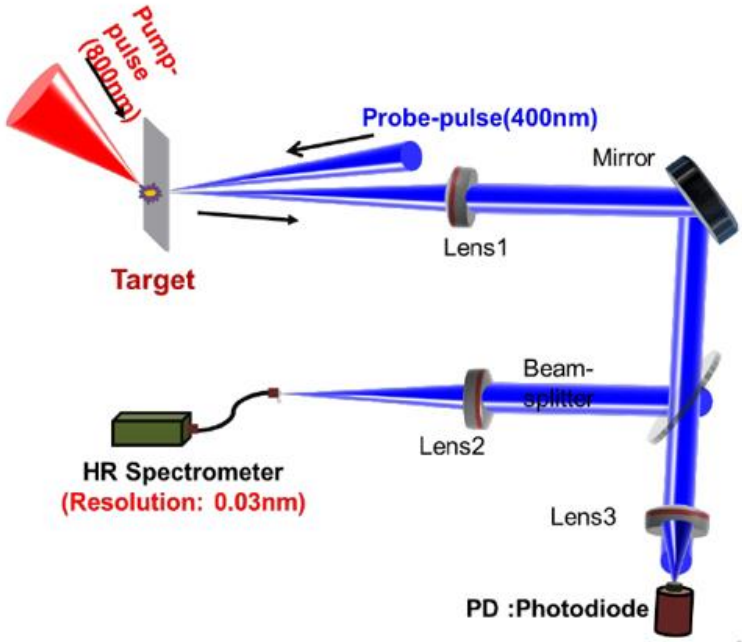

Fig 2.4.7 Set up of Doppler velocimetry

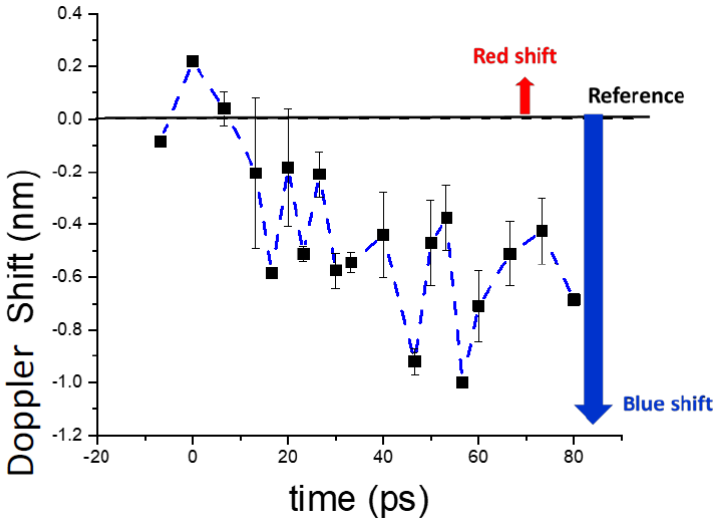

Fig 2.4.8 Target 30 μm Al foil result

Peak velocity ≈ 3 10. cm/s= 3 10H m/s = 300 km/s was founded. High value of result of rear side velocity we surprised. How to take into account errors and shot by shot variation still under discussion and it is not the main topic of thesis. The measurements of Doppler velocimetry seem to be confirmed by hydrodynamics calculations.

The Kirkpatrick-Baez (KB) microscope is an imaging device designed for x-ray imaging at grazing angles of incidence. It consists of two curved mirrors, typically cylindrical or spherical, installed perpendicularly to each other. Each mirror focuses x-rays in a single plane, resulting in an x-ray image in one direction. The KB microscope operates based on total external reflection, taking advantage of grazing incidence angles and optimizing it for a specific x-ray energy range.

In a KB microscope, the mirrors are coated with high atomic number (Z) materials to achieve high reflectivity. The present version of the KB microscope was built to reflect both soft and hard x-rays, up to 20 keV, while maintaining reasonable reflectivity and acceptance solid angle. The acceptance solid angle is determined by both mirrors, but it is important to note that the effective aperture in each perpendicular direction is limited by the long side of the mirrors. Due to the grazing angle, the projection of the long side in the direction perpendicular to the incoming x-rays is considerably smaller than the physical size of the mirror. This reduced effective reflecting surface and the changes in reflectivity with grazing incidence angle are taken into account in the design of the KB microscope.

The KB microscope was implemented in the interaction chamber of the 200 TW system (VEGA-2) at CLPU for the experimental campaign. It was used to characterize hot electrons in the rear side of the target. The KB microscope was employed to image the aluminum Kα radiation generated by laser-driven hot electron transport into a thick aluminum foil target. The emitted radiation was collected using an x-ray CCD camera (back-illuminated Greateyes model GE 1024 256 BI DD) with a pixel size of 26 μm. The camera was covered with two layers of 2 μm thick Mylar coating. The collected data of the aluminum target with different thicknesses and an

image of the signal are shown in Figure 2.4.10. The size of the target's rear side is approximately 300 μm, with little sensitivity to the target material and thickness.

Overall, the KB microscope provided imaging capabilities for studying the emitted radiation and characterizing the hot electrons in the target during the experimental campaign at VEGA-II.

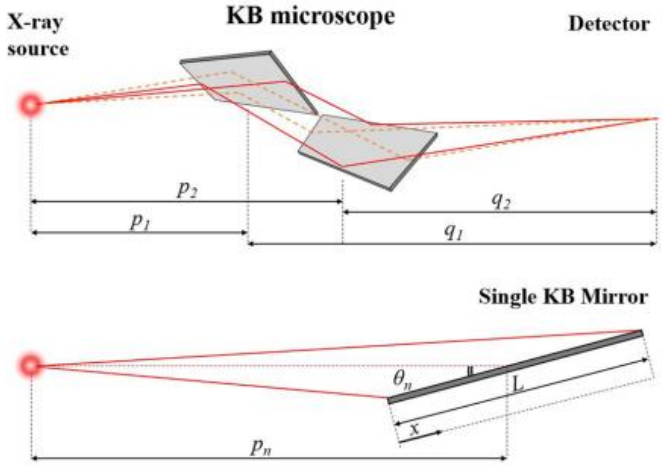

Fig 2.4.9 Schematic diagram of a KB microscope system. [Zeraouli 2019]

Characterization of the intensity and source size of Ti Ka emission E = 4.9650001 KeV

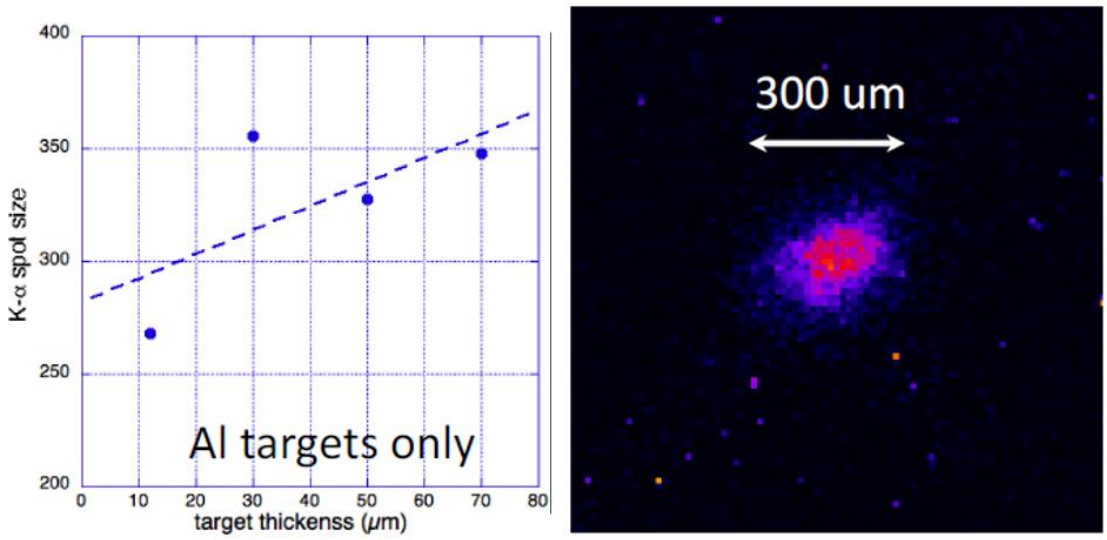

Fig 2.4.10 K_α data of Al target with different thickness and image of the signal.

The size of the con target rear side is around 300 μm with little sensitivity to target material and target thickness.

For the characterization of hot electrons were used electron spectrometer and Bremsstrahlung Cannon (BSC)

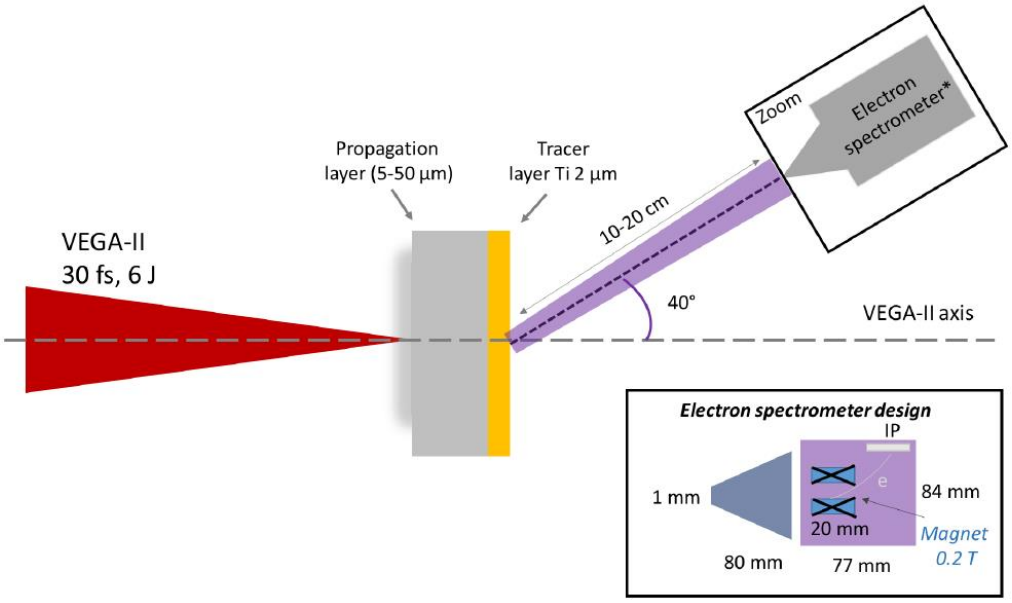

Fig 2.4.11 Set up of electron spectrometer in experimental campaign in VEGA-II. Electron spectrometer design shown below. Magnet 0.2 Tesla was used. IP type MS was used as a detector

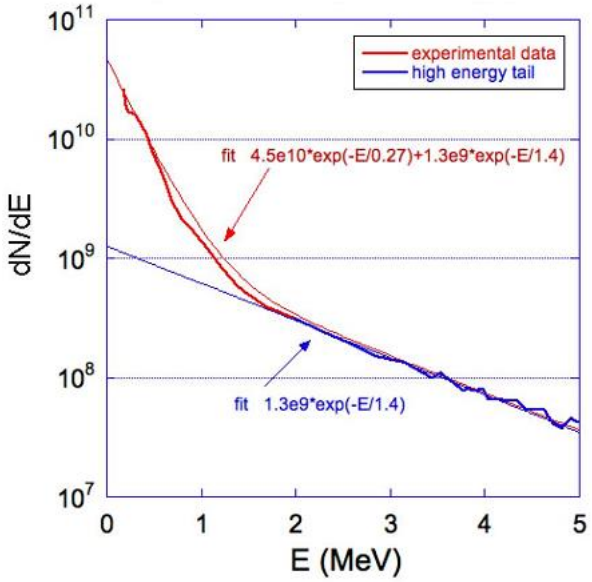

Fig 2.4.12 Electron spectrometer data 25 um Al

The expected hot electrons temperature was calculated using Beg scaling law T_{hot}~100keV$(I\lambda^2)^{1/3}$,for λ=800nm we found a value of the order of ~ 600 keV. Using the alternative Wilks scaling law formula $T_{hot} \approx 512keV[(1 + 0.073\, I\lambda^2)^2 - 1]$, a temperature of ~1.7 MeV was calculated. Hot electron temperatures were found intermediate between the temperatures given by the scaling laws.

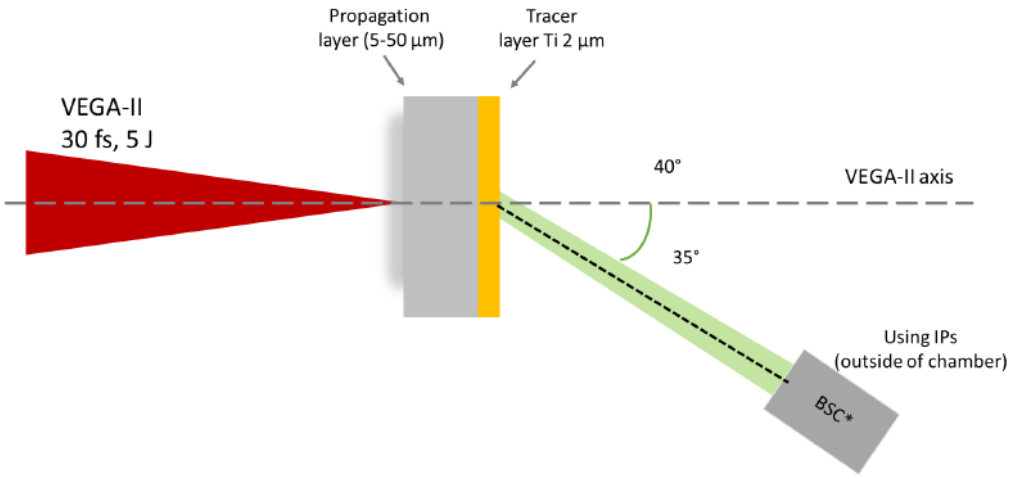

Fig 2.4.13 Set up BSC

The bremsstrahlung spectrometer (BSC) used in the experimental campaign was installed outside the chamber. A description of the BSC can be found in Part 2.1 of the report. Figure 2.1.1 provides a schematic view of the BSC. The distance between the target chamber center (TCC) and the first imaging plate (IP) was measured to be 90.5 cm. The effect of the chamber window, made of mylar with a thickness of 250 µm, was found to be negligible and was not considered in the analysis.

The schematic design of the bremsstrahlung cannon used during the experiment is shown in Figure 2.4.14. Multiple laser shots, typically 10 or 15, were necessary to achieve a significant signal on the imaging plates. The experimental results obtained from the imaging plates were normalized by the number of shots to account for shot-to-shot variations.

For the scanning and digitization of the imaging plates, an RICON MP C2051 scanner was utilized. The scanner settings used were as follows: S = 4000, L = 5, and B = 16 bits. These parameters determine the scanning resolution, line density, and the number of bits used for encoding the pixel values, respectively.

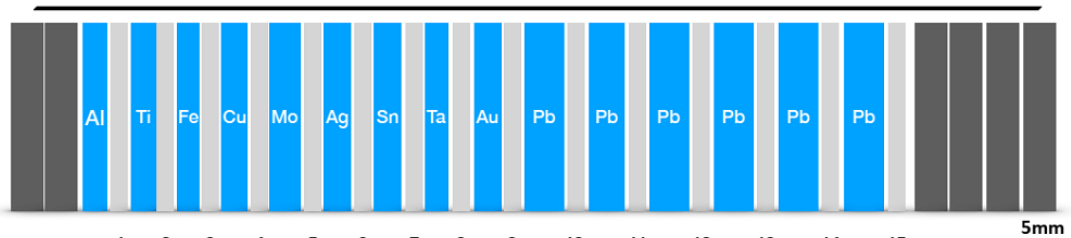

Filter	Al	Ti	Fe	Cu	Mo	Ag	Sn	Ta	Au	Pb	Pb	Pb	Pb	Pb	Pb
Thickness [mm]	0.09	0.12	0.12	0.1	0.1	0.15	0.5	0.5	1.56	1	2	3	4	6.35	6.35
$\rho[g/cc]$	2.7	4.51	7.87	8.96	10.22	10.5	7.31	16.65	19.3	11.35	11.35	11.35	11.35	11.35	11.35

Fig 2.4.14 Characteristics of the filters composing bremsstrahlung cannon used in our experiment on VEGA-II

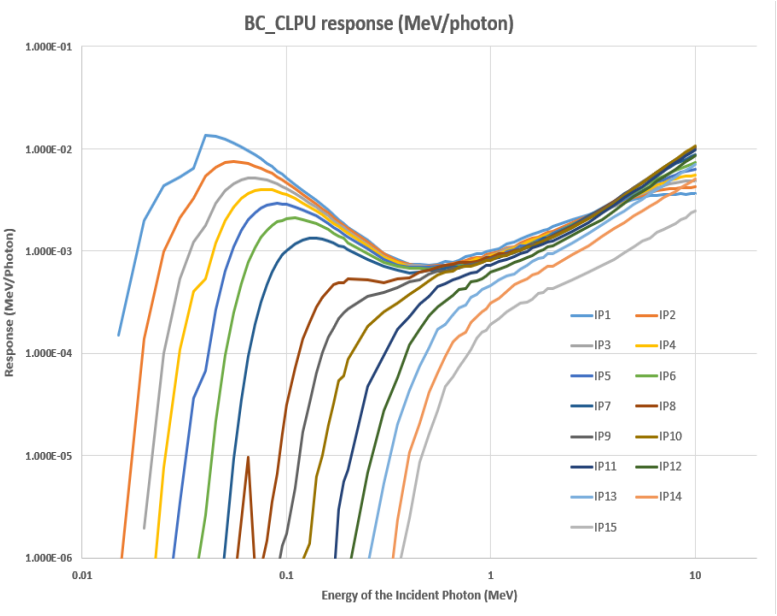

Fig 2.4.15 Response curve

To calculate the response curves of the bremsstrahlung cannon (BSC), Monte Carlo simulations were conducted using the GEANT4 code with the Penelope library. These simulations involved a series of 72 monochromatic X-ray beams.The purpose of these simulations was to evaluate the energy deposited in a single imaging plate (IP) and normalize it by the number of photons. By varying the energy of the monochromatic X-ray beams, the simulation can provide information about the response of the BSC at different energy levels. For each monochromatic X-ray beam, the Monte Carlo simulation calculates the energy deposited in the IP. This information is then normalized by the number of photons in that particular beam. Numerical simulations give the energy $D_i(k)$ deposited by the i-th monoenergetic beam in the *k*-th IP. Exploiting these results, it is possible to calculate the theoretical energy deposition in the IP is the distribution f according to the following formula.

$$E(k) = \sum_{i=1}^{72} \int_{E_{i-1}}^{E_i} f(E) \frac{D_{i-1}(k)+D_i(k)}{2} \mathrm{dE} \quad (2.8)$$

where $f(E)$ is the distribution function

We performed a $\chi 2$ minimization analysis, considering either an exponential distribution of photon and an exponential distribution of energy in GEANT4 simulation.

$$\chi 2 = \sum_{k=1}^{15} \left(E_{dep}(k) - E(k)\right)^2 \quad (2.9)$$

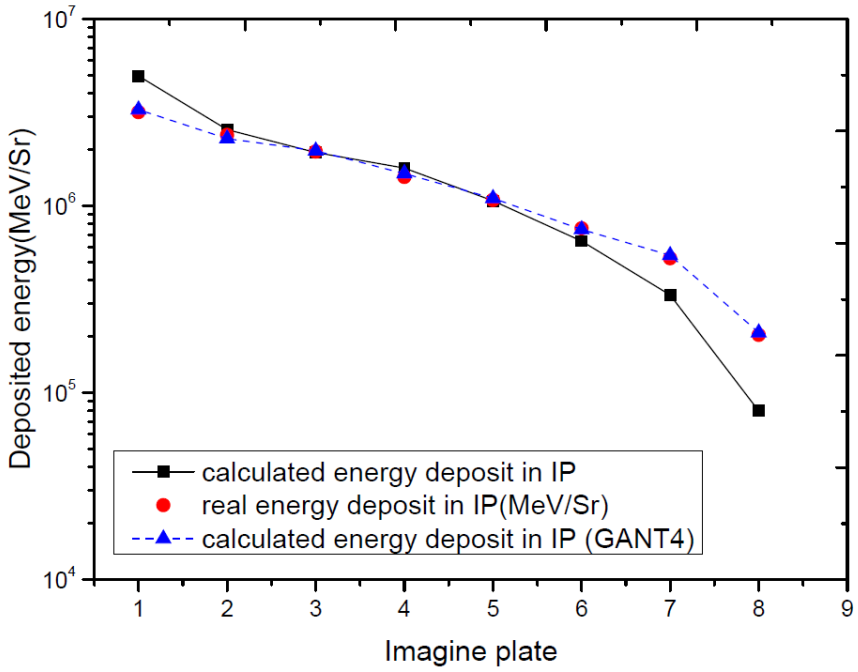

Fig 2.4.16 shot #50-64 in 25 Al target

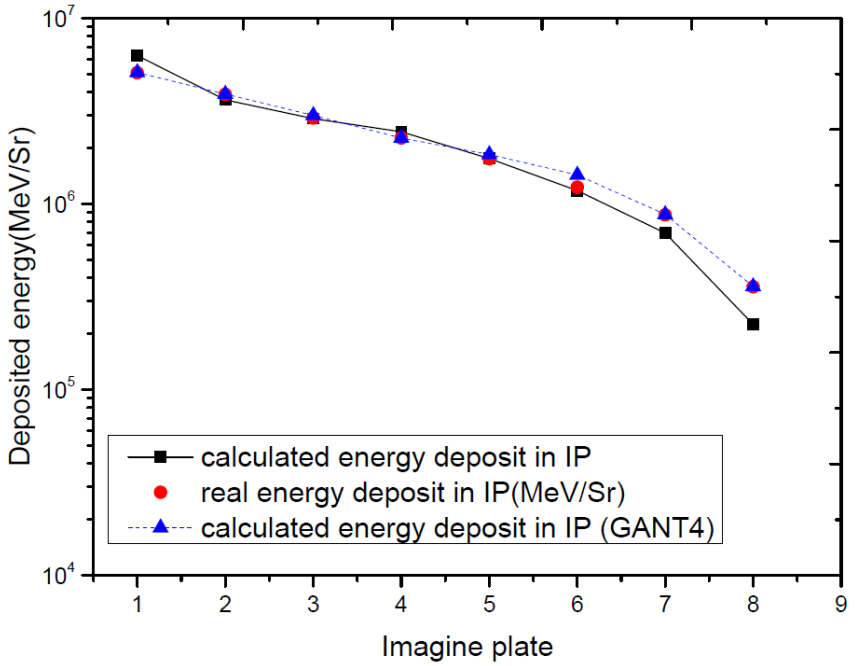

Fig 2.4.17 shot76-86 25 Al target

Figures 2.4.16 and 2.4.17 show the results of the BSC response curves obtained from the complex Monte Carlo simulations using GEANT4 with the Penelope library. These response curves were compared to the results obtained from the simple module for estimating hot electron temperature described in Chapter 2.2.

The comparison between the complex Monte Carlo simulations and the simple model for estimating hot electron temperature demonstrates a good agreement. The photon temperatures obtained from the simulations were found to be 99 keV and 101 keV, while the temperatures estimated using the simple model were 100 keV and 105 keV respectively.

This indicates that the simple model is working well and provides a reasonable estimation of the hot electron temperature. It allows for fast and preliminary analyses without the need for complex Monte Carlo simulations. The agreement between the results obtained from the simple model and the Monte Carlo simulations further validates the applicability of the model in estimating hot electron temperatures based on the BSC data.

Overall, the combination of the BSC response curves obtained from the Monte Carlo simulations and the simple model for estimating hot electron temperature provides a comprehensive and efficient approach for analyzing the experimental data and characterizing the hot electron distribution in the studied system.

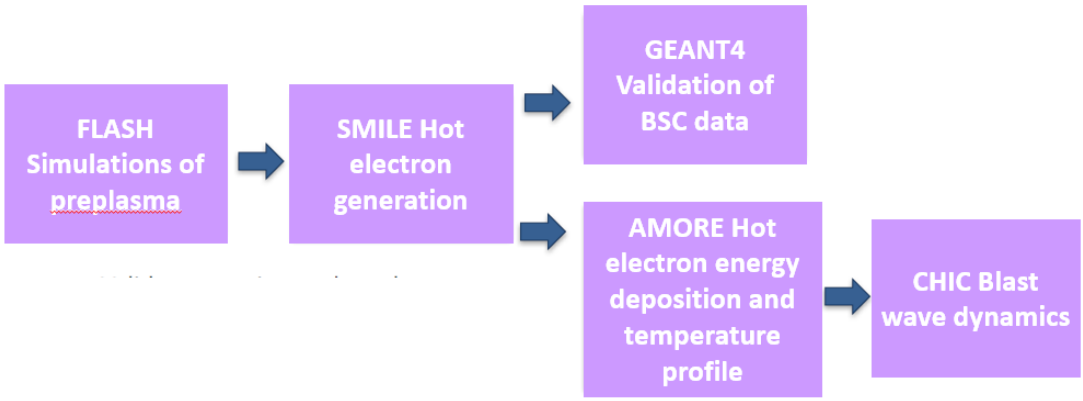

Fig.2.4.18 Simulation chain to validate experimental result

We presenting simulation done by Dr. M Touati behind [Touati et al,2014]. Simulation was done with parameters presenting in table

Simulation time duration (L_t)	600fs
Spatial cell size	0.5um
Kinetic energy step	10keV
Maximum kinetic energy (L_ε)	$3*10^4$keV
Simulation box size	L_z=70,50,30,20,10 or 6um and L_x=300um

Table2.3 Simulation box properties

Al from z=0 to 50um was used. Parameter was equal ρ=2.7g/cm^3, A=26.98, Z=13 and $T_e=T_i$=300K. Specular reflection of electrons at the target rear side and/or irradiated side or not are shown.

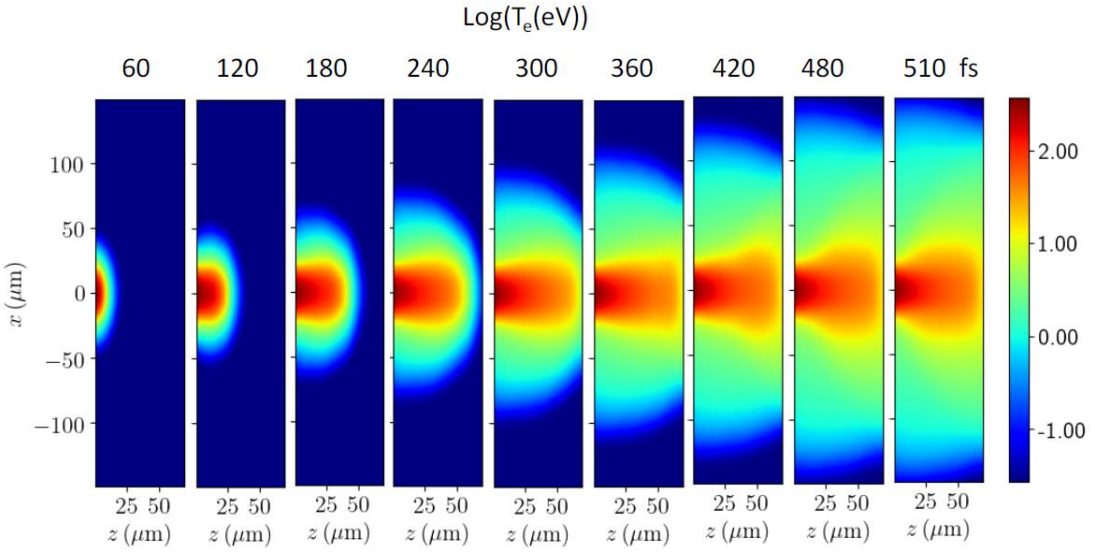

Fig 2.4.19 Electron deposition simulation result

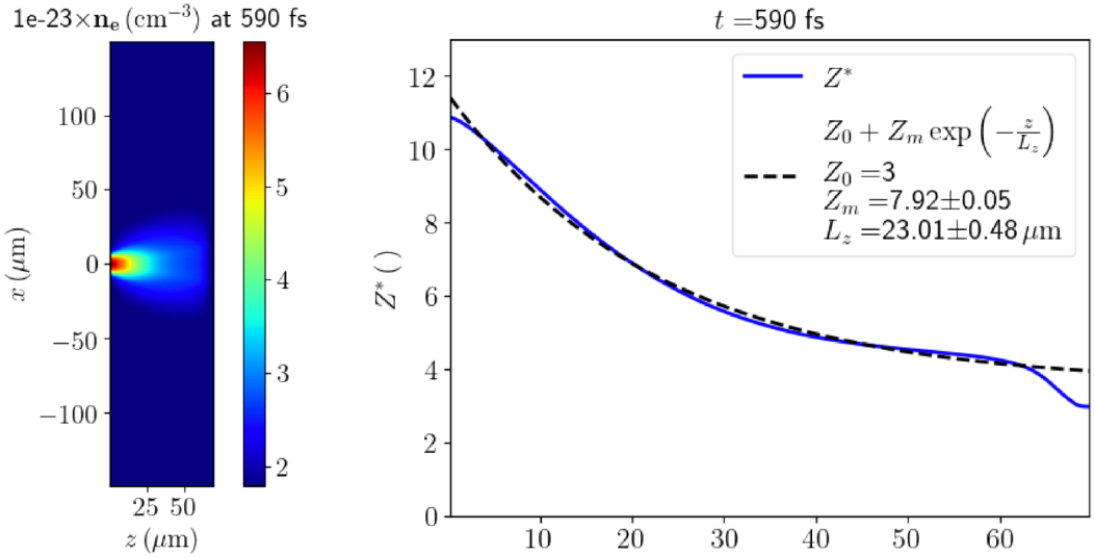

Fig 2.4.20 Simulation results rear side electron refluxing only

Simulation result show that target is strongly preheated by hot electron energy deposition.

In the current experiment, the hot electrons observed had lower energies compared to previous experiments. As a result, these lower-energy hot electrons deposited their energy more effectively in the target material, leading to a stronger target preheating effect. The higher energy deposition in the target can lead to the generation of stronger collective effects.

Although a compression wave is observed, it is noted that the wave does not exhibit the complete structure of a blast wave. A blast wave typically consists of a leading shock front followed by a rarefaction wave. The absence of the full blast wave structure suggests that the observed compression wave may be influenced by other factors or mechanisms in the experimental setup.

The presence of a strong compression wave indicates the transfer of energy and momentum from the hot electrons to the target material, causing significant changes in the target's physical properties. Understanding and characterizing these effects are crucial for applications such as shock ignition conditions and diagnosing matter under extreme pressure conditions.

Further analysis and investigation of the experimental data, along with complementary diagnostics and simulations, will be necessary to fully understand the dynamics and behavior of the compression wave and its relationship to the hot electron distribution and target response.

Conclusion

- Using a short-pulse high-intensity lasers we have been able to create very strong pressures (initially ≥ 100 Mbar)
- The pressure is not maintained in time and rapidly decreases to ≤ 1 Mbar at breakout
- Due to short pulse duration the shock has a blast wave structure
- There is a complex shock dynamic dominated by the effects of target expansion
- Due to non-maintained pressure, shock strength decreases with density faster than predicted from impedance effect only. Hence the shock does not accelerate but has constant velocity
- Due to target decompression the blast wave is lost along the axis and the pressure becomes lower and more uniform
- The blast wave structure is maintained out of axis
- The measurements of Doppler velocimetry seem to be confirmed by hydrodynamics calculations
- We showed that meaningful measurements of the physical characteristics of matter in HED states can be performed with short-pulse high-intensity lasers
- It may also be possible to do study using blast waves with implications for astrophysic

Chapter 3: Theoretical description of X-ray radiography and X-ray Phase Contrast imaging

3.1 X-RAY ABSORPTION IMAGING AND X-RAY PHASE CONTRAST IMAGING

3.1.1 X-ray absorption imaging

X-rays are electromagnetic waves with wavelengths ranging from approximately 10^{-12} to 10^{-8} m. Wilhelm Conrad Rontgen discover X-rays in 1895 and he quickly realised that they could be used to provide images. Rontgen's first X-ray radiograph of his wife's hand was taken only a month and a half after his discovery [Brailsford,1946; Mould,1980].X-ray continue to be an important diagnostic tool in medicine, biology, and materials science. They are particularly useful for investigating matter in extreme conditions, where the difference in the X-ray attenuation coefficient μ for different materials and densities leads to different patterns of intensity on detector is shown the basis for the principal Fig.3.1.1.

In inertial confinement fusion (ICF) experiments, unstable interfaces between materials at different densities give rise to hydrodynamic instabilities that can reduce target compression and increase mixing of the hot and cold parts of the fuel. These instabilities area major cause of reduced neutron yields, which means that measuring target compression and instability growth is essential to improving performance in ICF experiments. Crucially, X-ray absorption imaging can produce high-resolution images of the target throughout its compression sufficient to resolve density interfaces within the target and the growth of instabilities.

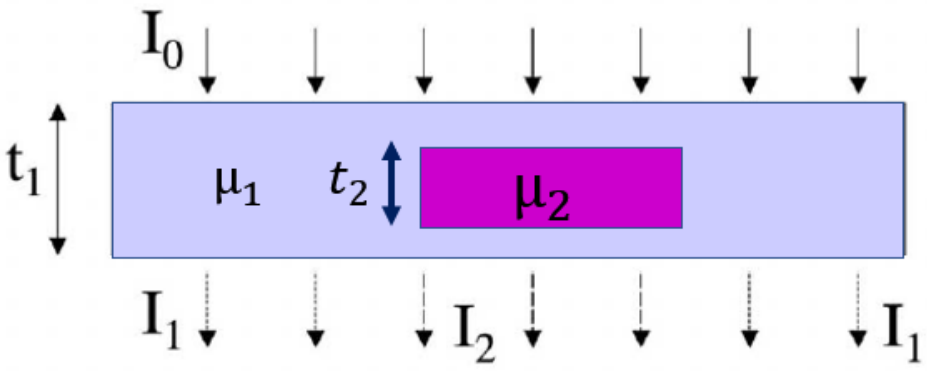

Fig 3.1.1 In the image presenting how contrast is produced in conventional X-ray imaging

Consider a simple radiographic scheme like that shown in fig 3.1.1. The attenuation contrast of X-rays passing through an object can be defined as

$$C_{att} = \frac{I_1 - I_2}{I_1} \text{ (3.1)}$$

where I_2 is the X-ray intensity transmitted in the shadow of the object and I_1 the intensity transmitted immediately outside it. If we define I_0 as the X-ray intensity incident on each object, then Beer-Lambert's law states that

$$I_1 = I_0 \exp(-\mu_1 t_1) \text{ (3.2)};$$

$$I_2 = I_0 exp[-\mu_1 (t_1 - t_2)] \exp(-\mu_2 t_2) \text{ (3.3)}$$

where μ_2 is the attenuation coefficient of the detail, μ_1 the attenuation coefficient of the background, t_2 and t_1 the thicknesses of object and background, accordingly [Webb,1988]. For an object composed of two compounds with different absorption coefficients $\mu_2 > \mu_1$, we can therefore express the attenuation coefficient as follows:

$$C_{att} = 1 - \frac{I_0 \exp(-\mu_1 t_1)}{I_0 exp[-\mu_1 (t_1 - t_2)] \exp(-\mu_2 t_2)} = 1\text{-}\exp[(\mu_1 - \mu_2) t_2] \text{ (3.4)}$$

When the two absorption coefficients are similar ($\mu_1 \sim \mu_2$) or the object is too thin, the exponential term in our equation approaches 1 and contrast will drop to zero.

3.1.2 X-ray phase-contrast imaging

X-ray Phase Contrast Imaging (XPCI) is based on the phase-shift of light and takes place together with absorption when light passes through matter. The absorption and phase-shift of light passing through matter can be characterized using the complex refractive index:

$$n=1-\delta+i\beta \text{ (3.5)}$$

where μ and δ related to the phase ϕ. In addition, μ and δ can be expressed like function of the object density. The β is connected to the attenuation properties of the given material [Suortti et al, 2003].

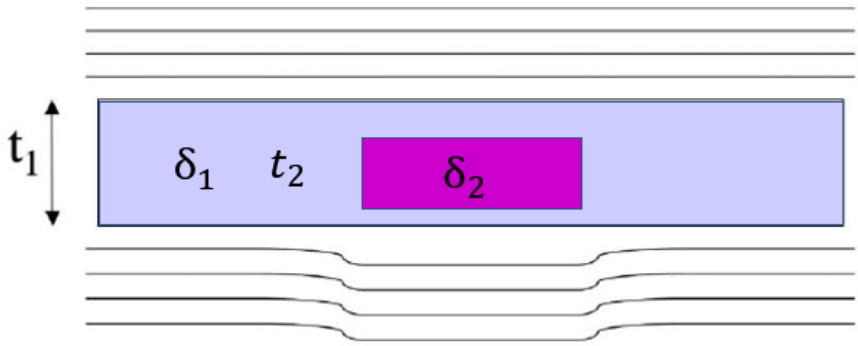

Fig 3.1.2 In terms of wave effects, interpretation of X-ray interaction with a sample consisting of a detail immersed in a uniform background.

$$\mu = \frac{4\pi\beta}{\lambda} \text{ (3.6)}$$

Where the λ is the x-ray wavelength. Here, δ represents the phase shift ϕ experienced by the x-ray wave field when it cross a given thickness of material

$$\phi(x,y) = \frac{2\pi}{\lambda}\int \delta(x,y,z)dz, \quad (3.7)$$

Where z is the propagation direction of x-ray. δ can be linked to the electron density ρ_e of a given material using the following equation:

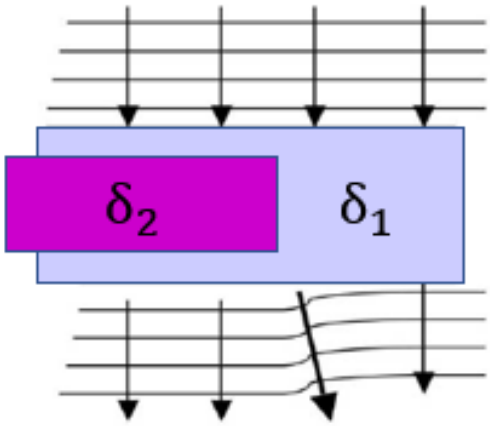

Fig 3.1.3 How object-induced wave front distortions translate into local changes in the X-ray propagation direction.Here we are using a ray-tracing representation (distortions have been exaggerated in the figure for clarity).

$$\delta = \frac{r_e \rho_e \lambda^2}{2\pi} \quad (3.8)$$

With r_e the classical electron radius. δ and β are directly linked to the imaginary and real part of atomic scattering factors [Bravin et al,2013].

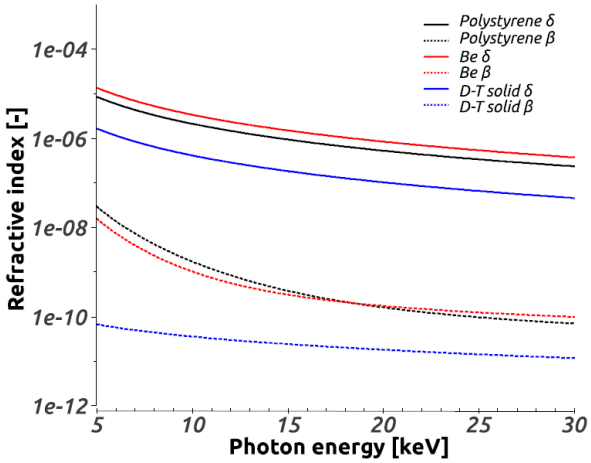

Fig 3.1.4 The two components of the complex refractive index for different materials of interest to nuclear fusion are plotted against photon energy [Tommasini et al,2017]. Energies are relevant to those that can be achieved at NIF and the curves are calculated using the data reported in [Henke et al,1993]. The graph shows both a factor 10^2 difference between δ and β, and their different dependence on photon energy.

The two components of the complex refractive index β and δ, are both functions of the density but scale differently with energy. The refractive index components for the materials illustrated in Fig.3.1.4 are shown as a function of

photon energy in Tab.3.1.1. The range of photon energies based on the most recent observations from NIF [Tommasini et al,2017], the curve are based on the information provided in [Henke et al,1993]. observing the δ values in compared to β, they are two orders of magnitude higher in Fig.3.1.4 one whose value falls as photon energy increases above δ. This means even at high photon energies, where attenuation is less than 10%, a high contrast can be attained using x-ray phase contrast imaging. Note also that using just absorption imaging, polystyrene and beryllium cannot be distinguished at these energies.

Material	**Density(g/cm^3)**	**μ(μm^{-1})**
D-T (solid)	0.252	$1.676*10^{-8}$
D-T(gas)	0.0006	$1.46*10^{-10}$
Be	1.85	$1.90*10^{-4}$
Polystyrene	1.04	$4.36*10^{-4}$

Table 3.1.1 Absorption coefficients for different materials of interest for nuclear fusion, evaluated at a photon energy of 8.0 keV .

There are variety of x-ray sources for X-ray phase contrast imaging, ranging from small-scale laboratories up to major facilities as:

- Rotating-anode and fixed-anode sources
- Synchrotron sources
- Free-electron lasers (such facilities as LCLS and XFEL)
- Energy-recovering linear accelerators
- Soft X-ray lasers

In summary, I would like to present a comparison between X-ray absorption and x-ray phase contrast imaging. In the case of XPCI, there are no constraints on object composition and size, where a X-ray absorption require materials that are strongly absorbing. XPCI has high sensitivity to density variation relative to X-ray absorption imaging. Furthermore, in absorption imaging the photon energy must be carefully selected considering composition the sample. Photon energy is not important for XPCI, but optics (crystal or gratings) or spatial set-up (distance) are required. For the analysis of X-ray absorption images, the Beer-Lambert law is used. In the case of XPCI, the analysis procedure depends on the photon energy range, object composition, and detection scheme.

3.2 X-RAY PHASE-CONTRAST IMAGING METHODS

X-ray phase-contrast imaging has been an important tool across medicine, biology and physics. The use of X-ray imaging to detect low contrast object in weakly absorbing materials is a powerful approach.

Different approaches have been created to take use of the phase-contrast in the x-ray regime. This section presents five major phase-contrast imaging methods: analyzer-based imaging methods, the interferometric method based on the use of crystal, grating interferometry (Talbot-Lau), edge illumination x-ray phase-contrast method, the propagation based imagine or in-line holography.

These techniques are different not only in parameters of experimental setup and criteria for x-ray beam spatial and temporal coherence, but also in determining the nature and amplitude of the images signal provided, and the amount of radiation dose sent to the object. The final image contrast for each of these approaches is characterized by several parameters, along with the x-ray detector's spatial resolution, the specific image generation mechanism, x-ray energy, and beam divergence. Also was done comparison of between all x-phase contrast methods.

3.2.1 Bonse-Hart interferometry (GBI)

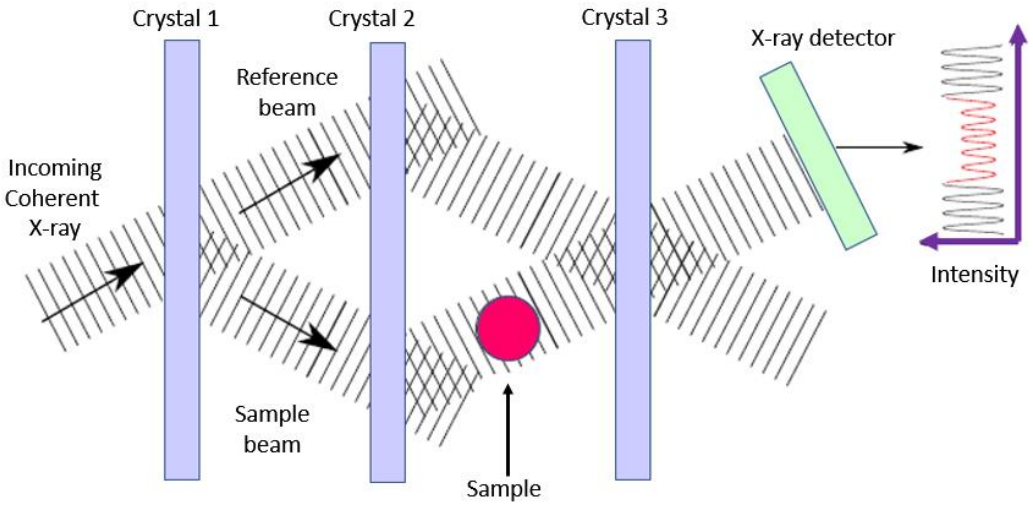

Fig 3.2.1 Layout of Bonse-Hart interferometer

The first phase contrast images were done using a crystal interferometer developed by Hart and Bonse in 1965 [Bonse et al,1965; Snigirev et al,1995]. The first crystal is a beam splitter that divides the x-ray beam in two. Next, the second crystal deflects the two beams so that they will converge at the same point on the third crystal. If an object is placed in the path of one of the beams-the sample beams before it reaches the third crystal, then the two beams will interfere on the third crystal and any modulations in phase can be measured. All three blades crystals are mounted on the same base and operate in in Laue mode. The beam is transmitted by the crystal but not reflected on surface in Laue geometry. The system is highly sensitive to vibration. The Bonse-Hart method is extremely sensitive to phase fluctuations but is also difficult to align. Bonse-Hant interferometry considered to be

one of the most sensitive XPCI techniques, but the method is not widely used widespread.

3.2.2 Analyser-based imaging (ABI)

Analyzer-based imaging (ABI) is a collective term used to describe methods such as: reflection-contrast radiography, phase-dispersion imaging, multiple image radiography, 'Schlieren' method, diffraction imaging, diffraction-enhanced x-ray imagine (DEI).

ABI uses a single analyzer crystal to record sample-induced changes in x-ray directions. The setup is a simplification of Bonse-Hart interferometer [Dean et al,2014]. Analyzer-based imaging methods use perfect crystal analyzers and a monochromatic beam. Only one crystal is applied as post sample beam analyzer, though other crystals are needed to condition the beam before it reaches the sample.

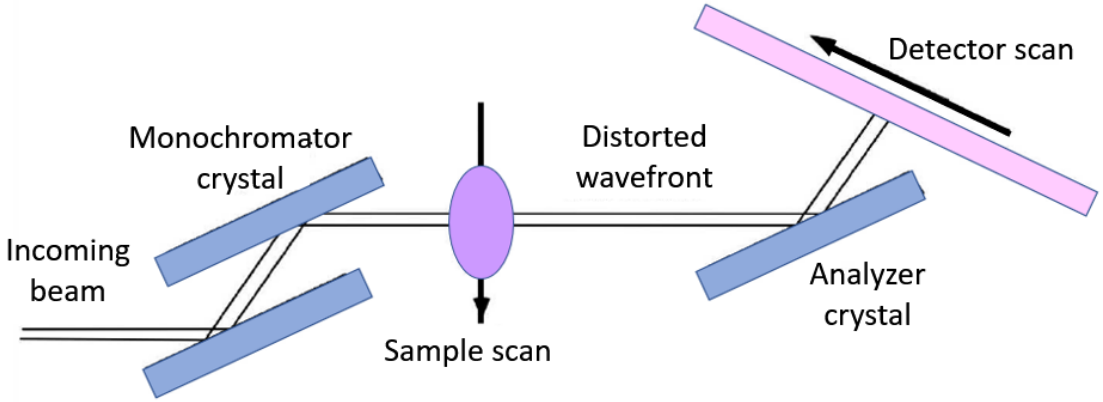

Fig 3.2.2 Analyzer-based imaging. The x-ray beam enters from the left-hand side,and is monochromatized by a double-bounce crystal. It then traverses the sample, is further reflected by the analyzer crystal, and eventually reaches the detector.

In fig 3.2.2 is presented a typical single analyzer crystal set up. In this case should be taken into account not just dependence of the crystal Bragg angle but also object and detector have to be scanned in opposite direction. This action is performed to compensate the inversion due to crystal reflection. The level of contrast can be tuned by changing the orientation of the crystal.

In fig 3.2.3, red lines represent rays diffracted by the top edge of the sample, while blue lines show rays deflected through a shallower angle towards the bottom of the crystal. The orientation of the crystal is on left side of the Bragg's peak. The negative fringe fit a top edge; the positive fringe corresponds the bottom edge.

The intensity can be described by the equation below if the diffraction plan of the crystal is parallel to the plan YZ which demonstrated in fig 3.2.3

$$I(x', y', k) \sim \frac{I_0}{M^2}\left[R(\theta) - R'(\theta)\frac{1\partial\phi}{k\partial y}\right]\theta \quad (3.9)$$

Where R is the crystal rocking curve and $R'$is first derivative of θ, θ is the angular variation of the crystal from the Bragg angle [Diemoz at el, 2012; Pogany at

el,1997]. Analyzer based image able to produce only one-dimensional map of the sample.

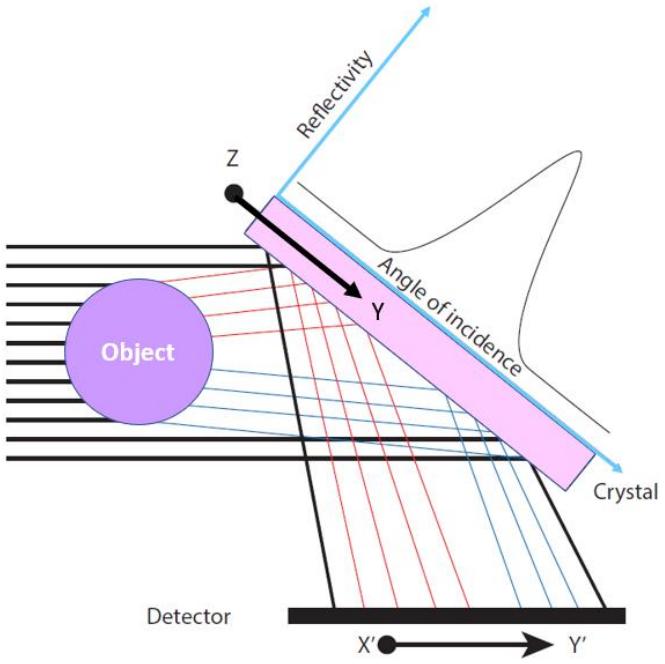

Fig 3.2.3 Analyzer based imaging: a planar crystal in Bragg geometry reflects the light coming from the object towards a detector. Rocking curve in the top of crystal presenting the reflectivity of the crystal-like function of angle of incidence

3.2.3 Edge illumination (EI)

Edge Illumination (EI) XPCI was developed in the late 1990s as an alternative to analyser-based imagine that does not need the use of an analyser crystal.[Olivo at el ,2001]. The main idea is illuminated only one edge of the detector pixels. Assume that the schematized set-up runs endlessly in the direction of the painting's plane. The slit is used to shape the beam so it should be very thin in the vertical direction and reaches far enough horizontally to encompass the entire target fig 3.2.4. The detector is composed of a single row of pixels and is the same width as the beam in horizontal direction [Peterzol et al,2005].

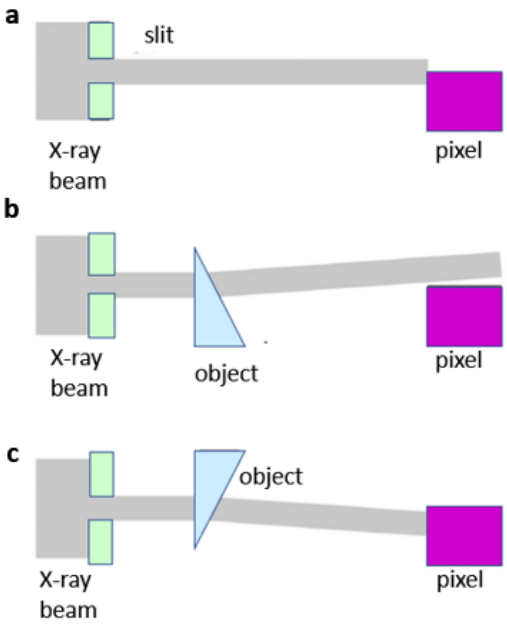

Fig3.2.4 The basic principle of edge illumination phase contrast imagines an x-ray beam aligned with the edge of a pixel (a) is refracted away (b) or toward (c) the pixel after passing through an object.

Scanning the object vertically through the beam, reading one image line at each item point, and combining these lines to generate the image map of 2D images. The main difference is that instead of fitting the detector active surface or at least reaching it in the middle, the beam hits the pixel array's edge.

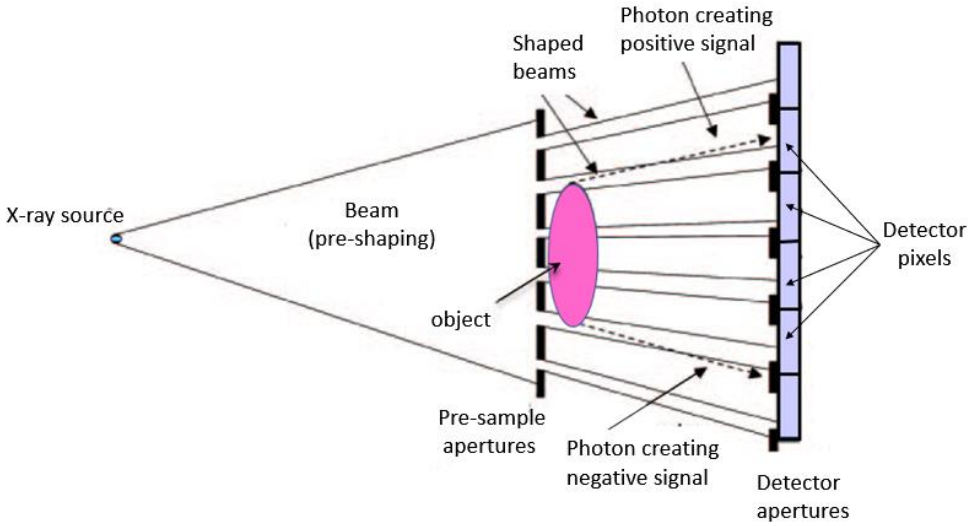

Fig 3.2.5 lay out of the lab realization of edge illumination phase contrast imaging. In presented schematic diagram two mask are used to reproduce the EI condition across the complete field of view

In addition, the technique allows for fully quantitative phase retrieval using only two images, which are obtained by illuminating the opposite edges of the pixel: this effectively inverts the differential phase signal while absorption remains unchanged,

similar to what happens in ABI when opposite sides of the crystal rocking curve are used. Second, the method was shown to be extremely resistant to increased X-ray energy, to the point that it can produce tens of times more image contrast than previous XPCI approaches as energy is increased [Diemoz et al,2013; Munro et al,2013]. However, and one of most important fact was demonstrated that if the set-up is adjusted and the phase retrieval method is further enhanced to include coherence effects, the method beats previous differential XPCI methods in terms of phase sensitivity by at least one order of magnitude. The approach also has the advantage of being resistant to environmental vibrations.

3.2.4 Propagation based imaging (PBI)

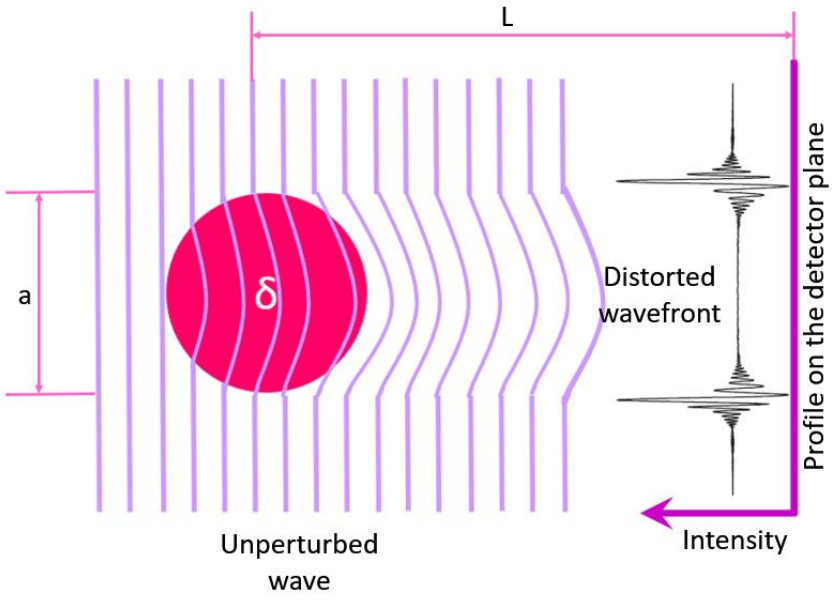

Fig3.2.6 During the image formation process in PBI, an image's intensity profile is provided. The perturbed and unperturbed wavefronts interfere according to the pattern's distance from the detector.

Optical elements are necessary for all the method outlined above. When a significant source of coherence is available, phase effects can be observed even without any optical components. The free propagation mode, also known as in-line propagation based XPCI or Propagation Based Imaging, is a unique method of imaging (PBI). This easy approach is represented in fig 3.2.6 an interference pattern is formed by positioning the detector at a distance from the object, rather than directly in touch with it as is done in radiology. If a sufficient propagation distance is given, the part of the wave front that has crossed the sample and is so deformed will interfere with the unaffected elements of the wave front passing immediately outside the sample[Wilkins et al,1996]. The region inside the object shadow is subtracted from the photons refracted by the object edge and the density gradient interfaces. These photons are refracted away from the path of the affected photons, creating an

increase in intensity around the object's edge, which is observed as interference peaks.

$$I(x,y,k) = \frac{I_0}{M^2} t \left[1 + \frac{R_1}{kM} \nabla_{xy}^2 \phi(x,y,R_0,k)\right] \quad (3.10)$$

Using the Fresnel-Kirchhoff formalism and a simplified model, the intensity distribution on the detector plane at distance R_1 can be described as follows. It is obvious from formula. that the intensity is proportional to R_1 as well as the source blurring effect, as previously explained. This means that increasing R_1 without diminishing the image is impossible [Snigirev et al,1995]. In comparison to the other three techniques, the intensity distribution on the detector plane is equal to the Laplacian of the phase, due to different sensitivity to phase variation. In addition, this approach can provide a two-dimensional map of the object phase.

3.2.5 Comparison of the XPCI Methods

The most used solution in XPCI are four techniques presented above (talbot-lau grating interferometry, analyser-based imagine, propagation based imaging, edge illumination). They have done multiple theoretical and experimental testing in a broad range of settings, including lab-scale facilities and synchrotron or FEL facilities. [Olivo et al,2014]

Firstly, lets discuss post-analysis of the measured images. The presence of optics gives constraints in the ABI, EI and GBI makes the phase-retrieval in this situation simpler. The phase shift, induced by the object and responsible of the intensity redistribution on the detector plane, is proportional to the grating period in the GBI technique. This fact give as opportunity to extrapolate all the information collected from a single observation, without modifying the set-up.

Secondary, let’s look at the source coherence. just propagation-based imaging method sensitive for spatial coherence of the source and resolution of detector. Other technique could work with incoherent sours and low-resolution detector. The reason of tolerance for the source and resolution of detector is availability of optic in set up.

As the third point of dictation is the set up. Set up of propagation-based imaging completely different compere other three methods. Optics precent in ABI, EI and GBI and absent in PBI. The set-up for a propagation-based experiment is resembling to an absorption imaging, it easy to be realize on facility designed for absorption imaging. PBI is less sensitive to alignment issues, which are crucial in the X-ray range, because it does not require optics. In comparison to the other three, it also needs less photon flux. The transmission of a grating in the X-ray range goes from 50% up to 80%. Because a crystal operating in the Bragg configuration can only reflect $4*10^{14}$ photons [Pfeiffer et al, 2008; Diemoz et al,2012; Stutman et al,2011; Pagot et al,2005; Zhou et al,2013] from a point-like source. The dependency of the image contrast on the object-detector at a distance is a problem of PBI. So also, this means while ABI, EI and GBI are orders of magnitude shorter than PBI setups, the PBI setup has a length scale in the order of meters.

Regarding the sensitivity to phase variation several studies have been done [Donnelly et al,2003].

It is challenging to specify the critical threshold at which one technique becomes more sensitive than the others. The procedure for creating an image involves many different components, for this reason. The size and spectrum of the source, the detector's resolution, the performance and quality of the optics, and the target under study are these [Pagot et al,2005]. Each of these variables has a different role to play in the three approaches. The PBI was noticed to be able to provide the best sensitivity for small objects (100 um scale) that present rapid variations in density in an experimental analysis. Larger things are more suited for the ABI and EI. The intermediate range is provided by the GBI.

Comparison of four XPCI technique was done using four points:

- ✓ Set up,
- ✓ Source spectrum and coherence,
- ✓ Sensitivity,
- ✓ Post-analysis procedure

The sum up of comparison clearly shown in table below

COMPARISON OF THE XPCI METHODS

	talbot-lau grating interferometry	**analyzer-based imagine**	**propagation based imaging**	**Edge illumination**
Setup	Grating (2 or 3) must be well aligned	Crystal	Optics are not necessary	Two masks
Source spatial coherence	Incoherent (Talbot-Lau)	Incoherent	Moderate coherence (related to the object features size)	conventional X-ray sources
Sensitive	Smooth density variation	Smooth density variation	Rapid density variation	Smooth density variation

Table 3.1 Comparison of different XPCI methods

Chapter 4: Results of X-Ray radiography and X-ray phase contras imagine experimental campaigns

4.1 RAL EXPERIMENTAL CAMPEING

The experiment described in this sections was prepared and performed in collaboration with CELIA, University of Bordeaux (France), University of York (United Kingdom), National Research Nuclear University MEPhI (Russia), Joint Institute for High Temperature, Russian Academy of Science (Russia), IGRRE JIHT RAS, Makhachkala (Russia), Dagestan State University (Russia), Science and Technology Facilities Council (UK), University of Oxford (UK), LULI Ecole Polytechnique (France), University of Leeds (UK)

4.1.1 Vulcan laser

Our experimental campaign was performed using the Vulcan laser facility, based at the Rutherford Appleton Laboratory.

Vulcan is an Nd:glass laser. These beam lines can be configured in any way to suit the experimental requirement. The Vulcan laser can deliver beams into three separate target areas: Target Area East (TAE), Target Area West (TAW) and Target Area Petawatt (TAP).

- TAE is a flexible area that can be configured to use all 8 beams. The six 10.8 cm/ 0.5 TW beams can each deliver several hundred joules in a nanosecond to target. The minimum pulse length for each beam is 80 ps and they can also be frequency doubled, if required. The two remaining 15 cm / 1 TW beams can be configured as back-lighter beams and again can be doubled.
- TAP currently uses a single ultra-high intensity beamline, provided by an optical parametric chirped pulse amplification (OPCPA) front-end. This can deliver up to 500 J in 500 fs within a focused diameter of 7 μm, resulting in a peak intensity on target of approximately 10^{21} Wcm−2
- TAW operates with two short pulse beamlines which can be configured in modes with pulse lengths from one to a few tens of picoseconds. Beam 8, using dielectric gratings, can deliver higher energies when operating at pulse lengths above 10 ps. Typical experimental configurations run with either dual 1 ps pulses or a mix of 1 ps and 10 ps pulses orientated at 90 degrees and deliver intensities of up to mid 10^{19}W/cm^2 .

Both short pulse beams operate with on-shot diagnostics including near and far field images, energy, spectrometer, autocorrelator, etc.

The 6 long pulse beams can be configured alongside the short pulses in multiple configurations, including single side cluster, cylindrical and spherical compression geometries. These beamlines are fully configurable in both number, location and angle. The beamlines can be operated with pulse lengths from 0.5 ns up to 8 ns and energy from 50 J per beam up to 300 J per beam depending on operational pulse length. Under request, the temporal shape of the pulse can be modified, and conversion into second harmonic is available on all long pulse beams. The standard jitter between the long pulses and the short pulses is around 150 ps but can be absolutely synchronized as a special configuration.

During performed experimental campaign was used laser parameter table 4.1

	Long pulse beam green	**Backlighted**
Pulse duration	2ns	1ps
Pulse energy	550J	50J
Pulse intensity	$3\ 10^{14}$ W/cm^2	$1\ 10^{18}$ W/cm^2
FWHM	400um	50um

Table 4.1.1 Vulcan laser parameters during experimental campaign

4.1.2 Gool of experiment

The experimental campaigns aimed to investigate the interaction of a strong shock with a cylindrical or spherical density inhomogeneity embedded in a low-density foam. These experiments were conducted both in the presence and absence of a strong magnetic field. To study these phenomena, low atomic number (low-Z) materials were used.

A key diagnostic tool employed in these experiments was high-spatial-resolution X-ray phase contrast imaging (XPCI). XPCI is a technique that is particularly sensitive to density gradients. It allows for the visualization and tracking of interfaces between different density regions, making it well-suited for studying the dynamics of shock-cloud interactions.

By utilizing XPCI, the experimental campaign aimed to access and analyze various parameters relevant to astrophysical shock-cloud dynamics. This includes the characterization of density gradients, the observation of interface evolution, and the identification of hydrodynamic instability structures as the shock wave interacts with the density inhomogeneity, resembling a "cloud" in this context.

The combination of low-Z materials, strong shocks, and XPCI as a diagnostic tool provides valuable insights into the behavior and dynamics of shock-cloud interactions. The findings from these experiments contribute to our understanding of astrophysical phenomena involving shocks and the complex interplay between shocks and inhomogeneous density structures.

Our primary objectives were to:

- ✓ Make X-ray phase-contrast imaging of strong shock interacting with a cylindrical object (‘cloud’) simultaneously in two orthogonal directions.

- ✓ Investigate the effects of varying, target geometry and shock strength on the "cloud".

4.1.3 Experimental design

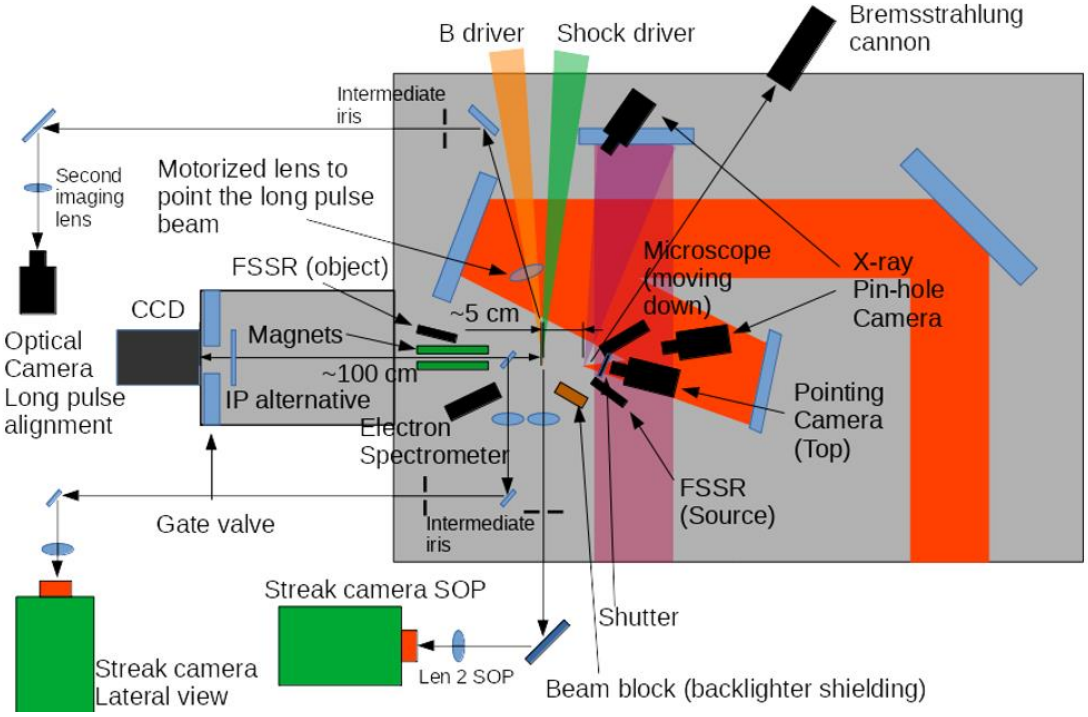

Fig 4.1.1A schematic layout of the experimental set-up

Three long-pulse beamlines at 2ω and nanosecond duration were used to drive a strong shock into a cylindrical target. The one short-pulse beamlines at 1ω was used to generate the back lighters for the XPCI at orthogonal direction with respect to the propagation direction of the shock. Parameters of the lasers is presented on the table 4.1

The short-pulse beamline was required for X-ray phase-contrast imaging. This beam was used to generate an X-ray pulse (bremsstrahlung radiation) 2 centimetres from the shocked target. The source size was limited by 5 μm pin-holes using a standard design for backlighter targets that had been deployed at other facilities (CLF and Orion). The detector image plate (BAS MS) was placed 40 centimetres from the target. A pinhole camera was imaging the laser and target interaction launching the shock and an optical streak camera for the image the rear side of the target to record the shock breakout (streaked optical pyrometry).

4.1.4 Targetry

Two type of target one for long pulse laser other for black lighter were used in TAW experiment as a back lighter target was used pin-hole to limit the source size attached to the backlighter foil (Cu). This design provides direct irradiation. Also

was used flag Cu foil (5-10 um thick) attached to the CH substrate. This type of target provide a lateral irradiation.

For the long pulse beam was designed foam target with plastic sphere inside and without it. The sphere was inserted in polystyrene sphere with radius 100um to simulate the “cloud”. The principle different between two target it’s just presents of the sphere inside the foam. Tube, pusher, and ablator made from same materials and thicknesses in a both target modification. Tube made of 5um polyimide. Ablator layer was parylene 25um. As a pusher was used 5 um of titanium to shield the foam from the radiation emitted during laser-matter interaction. The material inside the tube was TMPTA foam with density 0.1g/cm^3. Schematic lay out of the target with sphere is shown in fig 4.1.2.

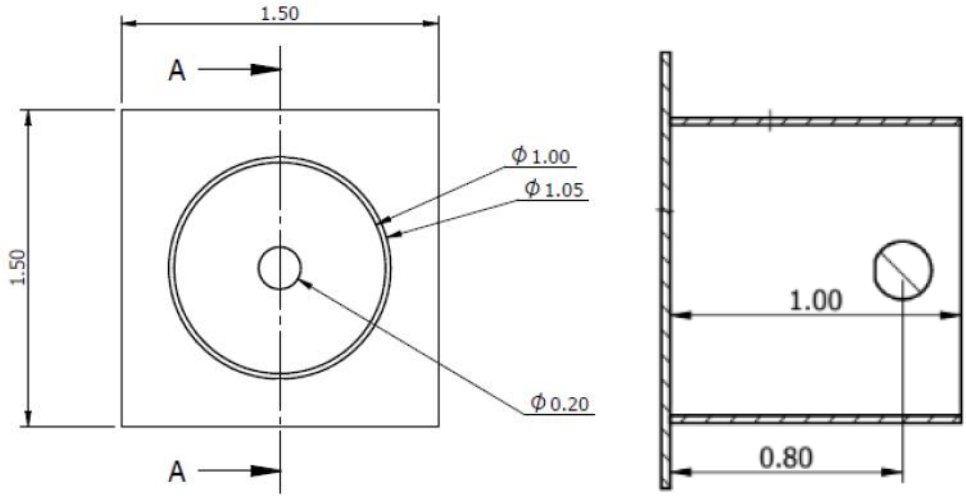

Fig 4.1.2 Designe of target with d=0.2 mm Polystyrene (C8H8)n sphere d=0.2mm

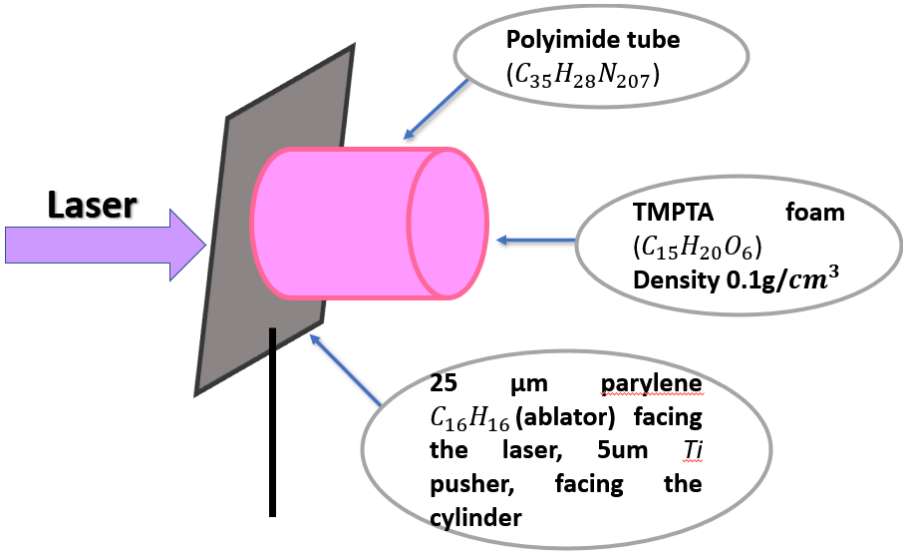

Fig 4.1.2 Target design

Three shots were done using grid targets. Gride made by cuprum. Pitch was 50um. Grid parameters were given conversion for the 1 pixel per microns. In our case 1 pixel equals 3.9 microns. For conversion was used shot #63 with grid target fig 4.1.3 behind and ImageJ framework. Magnification is 14.

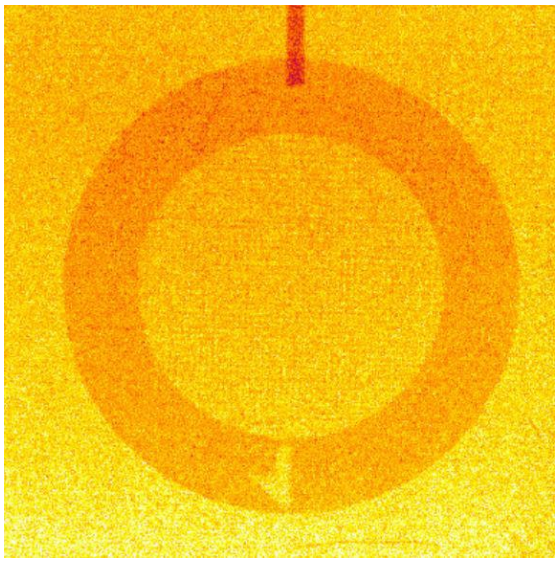

Fig4.1.3 picture of the Cu grid shot #63 for the resolution data. According to image 1 pixel equal 3.9 microns

The targets were aligned firstly at the target alignment stage equipped with four image systems absolutely referenced with the image systems for TCC by using tip. To align the target and set the target angle in image systems we used the target holder with the X-Y-Z manual translation. Target pre alignment was done in a same time using the external alignment bench in Vulcan facility.

4.1.5 Phase plates

Phase plates (PP) are optical elements used to alter and control the intensity distribution of laser beams in their focal plane. PP created to form the focal spot into highly repeatable envelope profiles with well-defined small-scale intensity statistics. Phase plates work by altering the phase of a beam in the near field (at the focusing optic), thus producing the desired intensity profile in the far field (in the focal plane). The Gershberg-saxton algorithm is used to design them: an input beam with a known input intensity profile and a best-guess phase profile in the near-field is the Fourier Transform to the far-field; an input beam with a known input intensity profile and a best-guess phase profile in the far-field is the Fourier Transform to the far-field. The focal-plane intensity is removed and replaced with the required intensity profile, but the phase is preserved. Then there's Inverse Fourier Analysis. Returning to the near-field, the intensity is destroyed and replaced with the known input intensity, while the phase is kept for the next iteration. The convergence is obtained. The near-field phase profile is binarized and glass slabs are engraved. Depending on the manufacturing process, various technologies of PPs exist. More recent methods have allowed to manufacture PPs with continuous phase-shifting profiles. The most common ones, Kinoform Phase Plate (KPP) are widely used in high -power laser facilities, and especially in the ICF domain. Random phase plates (RPP) reproduce the phase profile using discrete square elements that induce a 0 or π phase shift

Recent approaches have enabled the production of PPs with continuous phase-shifting characteristics. As an illustration, the probability density to find a hotspot with an intensity I for a beam smoothed by RPP follows an exponential law

$$P(I) \propto 1/\boldsymbol{I} \exp\left[-I/\boldsymbol{I}\right] \quad (4.1)$$

Small-scale intensity variations, also known as speckles, show that local areas of the plasma are eventually exposed to intensities several times higher than the average. For a purely RPP-smoothed speckle -pattern, according to formula, C=100% (this is also true of KPP-smoother speckle pattern). Reducing the contrast is achieved by other smoothing techniques, including the simple overlap of laser beams.

The RPP was used in TAW experimental campaign. The gaussian shape of the shock front was not seen in the shots without phase plate is shown on fig 4.1.4(b). The gaussian shape of the shock front is clearly observed in a shots with RPP fig 4.1.4(a)

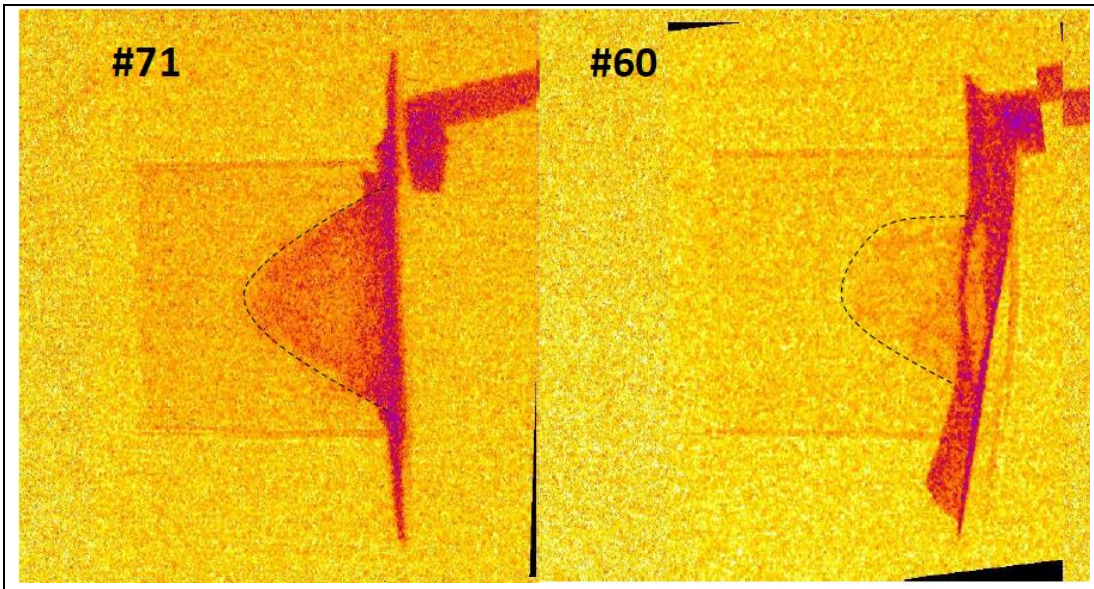

Fig 4.1.4 a) Gaussian shape of the shock in the shot with phase plate shot #71 with RPP E=617J, τ=35ns; b) shot #60 without phase plate E=551J, τ=10ns gaussian shape is not observed

Here and after in our analysis we consider just shots with RPP in which distinctly observed gaussian shape of the shock front.

4.1.6 Experimental result

In this section, we present the experimental results obtained using the Vulcan TAW laser at the Rutherford Appleton Laboratory's Central Laser Facility in Oxfordshire, United Kingdom. The aim of the experiment was to study the propagation of shockwaves using X-ray phase contrast imaging (XPCI).

X-ray absorption radiography, which relies on high density ratios for effective imaging, XPCI is particularly sensitive to density gradients within a material. This makes it a suitable diagnostic tool for studying shockwave dynamics, where density variations play a crucial role.

For our diagnostic purposes, we employed phase contrast-enhanced time-resolved X-ray radiography. This technique utilizes X-ray phase contrast imaging to enhance the visibility of various features within the sample, including target edges and the shock front. By capturing X-ray images at different time intervals, we were able to observe and analyze the temporal evolution of the shockwave.

The Vulcan laser facility provided the necessary infrastructure and capabilities to conduct these experiments. It is a high-power laser facility that offers precise control and delivery of intense laser pulses. The facility's advanced capabilities, combined with the XPCI diagnostic technique, allowed us to investigate the propagation of shockwaves in a controlled laboratory environment.

By analyzing the experimental results obtained at the Vulcan laser facility using XPCI, we gained valuable insights into the dynamics of shockwave propagation and the associated density gradients. These findings contribute to our understanding of shockwave physics and have implications for various fields, including astrophysics, material science, and high-energy density physics.

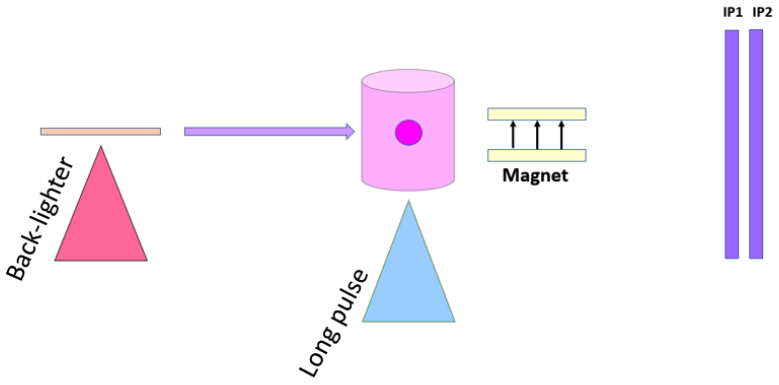

Fig 4.1.5 Experimental lay out of XPCI diagnostics. Distance between copper wire (backlighter target) and main target is 50 mm. Distance between main target and detector (first imaging plate MS) is 700mm. Magnet is placed between object and IP.

In the experimental setup, 10 μm diameter copper wires were used as backlighters for the imaging. Copper was chosen as the material for the wires due to its favourable characteristics, such as good penetration of approximately 8 keV photons through the target. The target itself consisted of plastic foam with a thickness of nearly a millimetres.

For detection purposes, an MS imaging plate (IP) was employed. The IP is a type of detector that records the distribution of radiation exposure. After each shot, the IP was scanned to capture the image. The time interval between shots and scanning of the IP ranged from 15 to 35 minutes.

In order to prevent hot electrons from reaching and saturating the imaging plate, a magnet was installed between the main target and the detector. The magnet helped in deflecting and redirecting the hot electrons away from the imaging plate, ensuring accurate measurements and preventing any undesired saturation effects.

The choice of using a magnet and the specific materials and parameters mentioned in the experimental setup were made to optimize the imaging process, minimize interference, and obtain clear and reliable data for further analysis and interpretation.

All images was normalised before analysis. For normalization should be followed several steps:

- Background should be subtracted. (Background is a value out of IP)
- Value of the image should be divided by the value of the source.

Normalization steps were done using ImageJ framework.

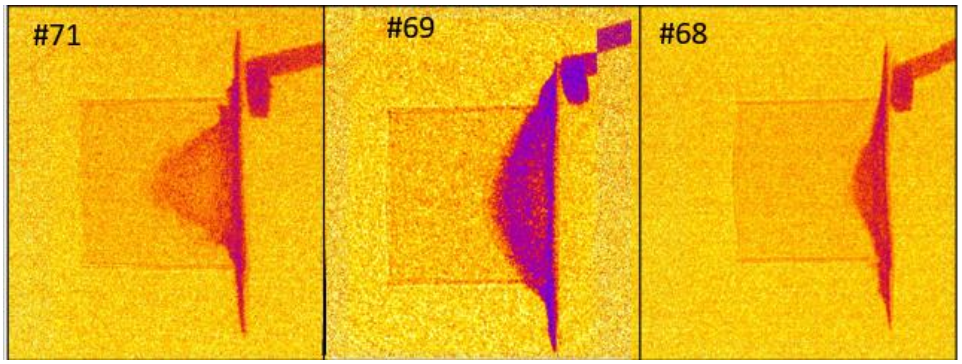

Fig 4.1.6 Normalised images of the shock-wave propagation at different moments of comparison. The delay of laser pulses increasing when going from the left to the right (15ns ,25ns and 35ns)

In the analysis, the length and width of the target were measured for each shot. These measurements were found to have good agreement with each other and with the schematic references, indicating the accuracy of the experimental setup.

To measure the distance between the shock and the pusher, an image analysis tool called ImageJ was used. ImageJ allowed for precise measurements of the shock distance in each shot. The conversion from pixels to microns was performed using the resolution shot data, which provided the necessary calibration for accurate distance measurements.

The shock distance was measured from the edge of the target to the maximum point of the shock. This distance measurement provided valuable information about the propagation of the shock wave.

In Figure 4.1.6, the Gaussian shape of the shock wave propagation is clearly observed. This characteristic shape allowed for the use of Gaussian interpolation to determine the shock propagation profile. The interpolation process was carried out using Origin 9 software, which is commonly used for data analysis and visualization.

By utilizing these measurement techniques and interpolation methods, the researchers were able to accurately characterize the shock wave propagation and obtain valuable insights into the dynamics of the experimental system.

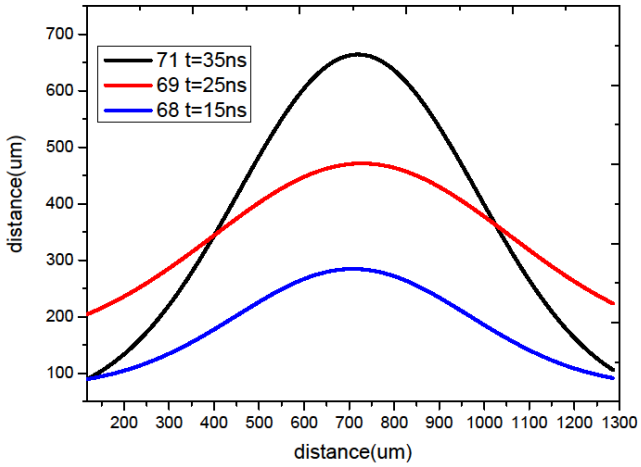

Fig 4.1.7 Gaussian interpolation of shock propagation profile of shots #71, #69, #68 with different delay of laser pulse.

In the table 4.1.2 is presenting laser pulse parameters and experimental condition for each shot. The value of FWHM was founded around 600-700um and shown in fig 4.1.7. Shots with different time delay was consider. FWHM doesn't depend on delay. Average shock distance and time delay was calculated for shots with and without phase plate. Shock distance equal 364 um with time delay 20 ns if we take into account shots where RPP was absent. Average value for shock distance and delay are 430 um and 25 ns in case of shot with phase plate were considered. Average energy was founded around 555J.Pulse duration was 2 ns and intensity I ~ $3*10^{14}$ W/cm^2 in a main laser beam.

Backlighter laser worked in picosecond regime with pulse duration 1ps, energy was 50 J. Intensity was I ~ $1*10^{18}$ W/ cm^2 . FWHM was 50 um. Data of laser parameter during experimental campaign is accurately performed in Table 4.1.2

#Shot	shock distance (um)	delay (ns)	Energy (J)	Presents of phase plate	FWHM(um)
57	280.8	10	565	-	-
58	312	10	573	-	-
59	304.2	10	512	-	-
60	491.4	10	551	-	-
64	437.9115	15	591	RPP	-
65	397.8	15	420	RPP	714
66	383.2	15	420	RPP	550
67	426.39	15	643	RPP	1170
68	291.2	15	623	RPP	608
69	436.2	25	594	RPP	776
71	655.2	35	617	RPP	625
#1	364	20	Average including shots without RPP		
#2	430	25	Average of shots with RPP		

Table 4.1.2 number of shots, shock distance(um), delay(ns), energy for each shot(J) and FWHM (um) were varied in order to get shots with different parameters is summarised in present table. Presents of phase plate also marked here. Average value of shot distance and delay was calculated.

Interpolation of the function of shock distance to delay was done using all shot with different time delay and laser energy. Concerning to interpolation was calculated shock velocity which equels17.20 km /s

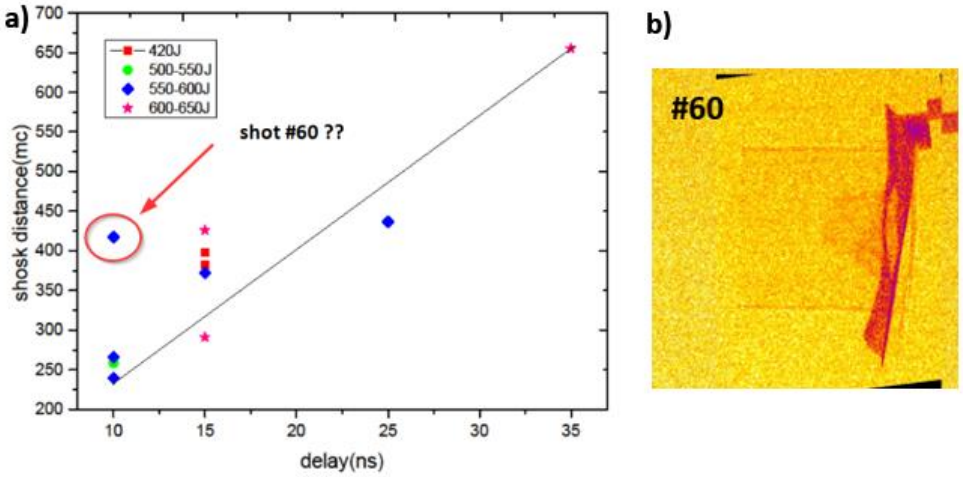

Fig4.1.8 (a) Interpolation of set of shots was done in presents graph. Velocity was founded 17.20 km/s. Shot #60 was not taking into account (b) The result of shock wave propagation for shot #60.

In the experimental analysis, it was observed that Shot #60 had certain discrepancies that raised doubts about its reliability. Figure 4.1.8(b) clearly shows that the target in this shot was tilted, and it was also performed without the phase plate. Due to these reasons, the decision was made not to consider the data from Shot #60 in the analysis.

To investigate the relationship between time delay and the distance of shock wave propagation, three specific shots were selected. These shots were chosen because they had the same energy and were performed with the phase plate, ensuring consistency in the experimental conditions. However, the time delays for these shots were different: 15 ns for Shot #68, 25 ns for Shot #69, and 35 ns for Shot #71.

The pusher velocity was calculated by interpolating the data from these three shots. The interpolation allowed for the determination of the pusher velocity as shown in Figure 4.1.9, which was found to be equal to 18.20 km/s.

The full analysis and comparison of these three shots, considering the same energy but different time delays, is presented in subsequent sections of the study. The analysis explores the direct dependency between the time delay and the distance of shock wave propagation, providing valuable insights into the dynamics of the experimental system.

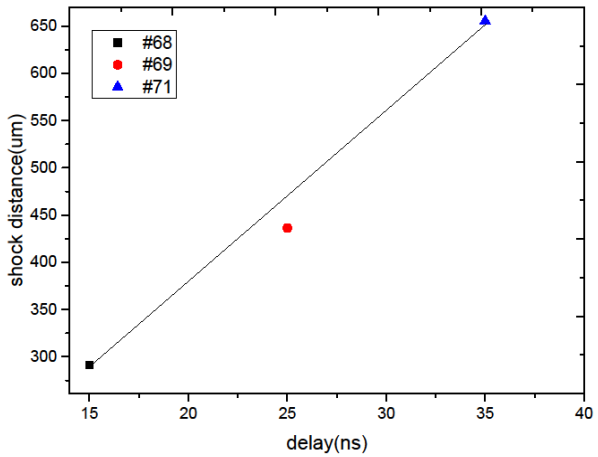

Fig 4.1.9 Interpolation of selected shots #68 #69 #71 is done in graph. Velocity was founded 18.20 km/s

Nominal FWHM, velocity pressure and intensity were calculated using analytical equation behind.

In a case we have Gaussian laser beam (intensity) equation behind can be used

$$I(r) = I_0\, exp\left(-2.77\frac{r^2}{D^2}\right) (4.2)$$

where D is the FWHM (for *r=D/2* you get *exp(-0.69)=0.5*).

Using the perfect gas approximation Relation between Intensity and pressure

$$P(MBar) = 8.6\left(\frac{I}{\lambda}\right)^{\frac{2}{3}} (4.3)$$

where ,

I-the intensity in units of 10^{14} W/cm^2

λ-the laser wavelength um

Relation between pressure and shock velocity (assuming perfect gas equation of state)

$$D\left(\frac{km}{s}\right) = \sqrt{\frac{\gamma+1}{2}\frac{P}{\rho}} = 11.53\sqrt{\frac{P(MBar)}{\rho(g/cm^3)}} (4.4)$$

Therefore

$$D\left(\frac{km}{s}\right) = 11.53\sqrt{\frac{8.6\left(\frac{I}{\lambda}\right)^{2/3}}{\rho(g/cm^3)}} = \frac{33.81\, I_0^{1/3}}{\lambda^{1/3}\rho^{1/2}}\, exp\left(-\frac{2.77}{3}\frac{r^2}{D^2}\right) (4.5)$$

$$\left(\frac{km}{s}\right) = 11.53\sqrt{\frac{P(MBar)}{\rho(g/cm^3)}} (4.6)$$

v-velocity

D~$I^{1/3}$ (4.7);

D_{shock}=400$\sqrt{3}$ (4.8)

Nominal FWHM compatible with FWHM of the laser(692um). Shock propagation is local 1D. Result of calculations shown in table4.1.3

	Nominal	Real in experiment
v(km/s)	60	18.20
P(Mbar)	27.5	2.23
I(W/cm^2)	$3*10^{14}$	10^{13}
FWHM(um)	692	700

Table4.1.3 comparison between experimental data and nominal calculated velocity, pressure, intensity value and FWHM

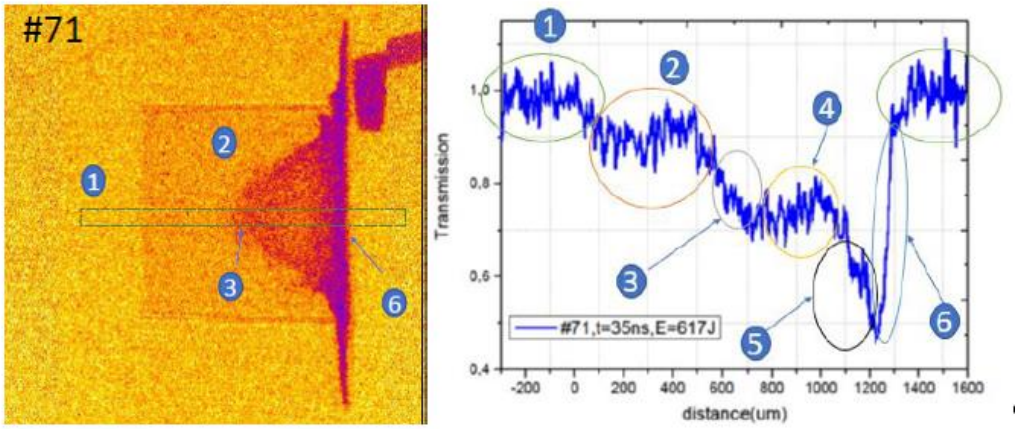

Fig 4.1.10 In the picture presented a) shock-wave propagation image of shot #71(E=617J, τ=35ns) and b) transmission profile of the shot #71 in horizontal direction (green square). Numbers related to the different matter condition of the foam target after laser interaction 1- vacuum (source intensity) 2- cold plastic 3- shock front 4- compressed material 5- expanding matter 6-beginning of the target

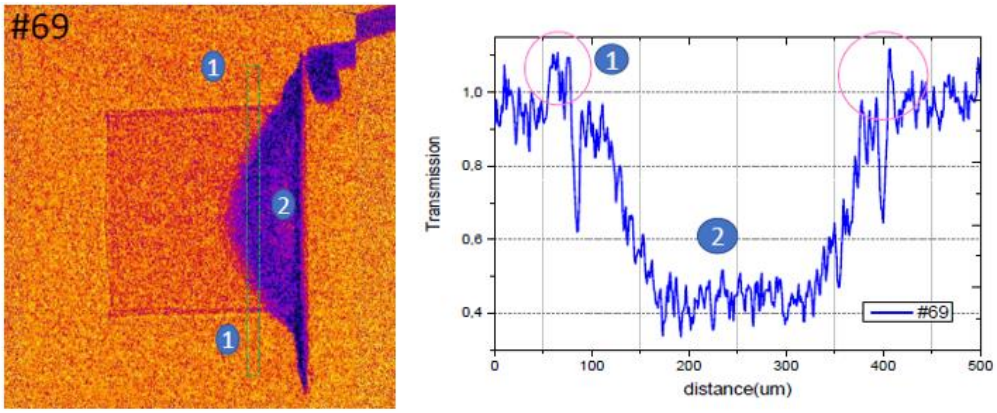

Fig4.1.11 In the figure demonstrated (a) shock propagation XPCI of shot #69 (b)Transmission profile of the shot #69 in vertical direction (green line).Number in a picture shown to the 1-X-ray phase contrast feature at target edge 2-Compressed material

Different matter conditions of the foam target after laser interaction presenting in fig 4.1.10. In presented transmission profile numbers correspond for matter condition.

1- vacuum (source intensity)
2- cold plastic
3- shock front
4- compressed material
5- expanding matter
6- beginning of the target.

In a fig 4.1.11 observed regions of X-ray phase contrast feature at target edge and compressed material in transmission profile of shock propagation image of shot #69. Grean line show direction of extracted transmission profile in both images fig 4.1.10 and fig 4.1.11.

Polystyrene sphere present in target in shot #69 and #71. Position of the sphere in target design drawn and in real shot imaging shown behind. In fig 4.1.12 clearly observed fact that shock didn't reach the sphere because of real intensity much lower than expected. The existence of the sphere does not affect the received data. We don't take into account presents of the polystyrene sphere in targets in shot 69 and 71 in our data analysis and numerical simulations.

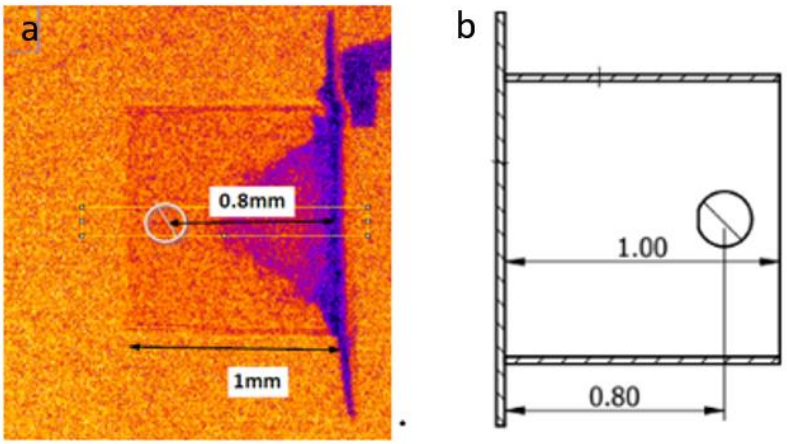

Fig 4.1.12 (a) shot # 71 with marked "guessing" sphere position (b) target disigne with position of the polystyrene (C8H8)n sphere d=0.2mm.

The theoretical transmission of cold material in our case is 0.864 calculated by [CXRO]. For theoretical calculetion we summarized transmision of materiale used in a target composition with the appropriate densities of used material(Polyimide ($C_{35}H_{28}N_{207}$) ;TMPTA($C_{15}H_{20}O_6$) with ρ~ 0.1 g/cm^3;Polystyrene(C_8H_8)).

Comperison of 3 transmision profiles with diferent time delay are shown in fig 4.1.13. In fig 4.1.13 clearly observed transmision around 0.9 in cold plastic reagion.

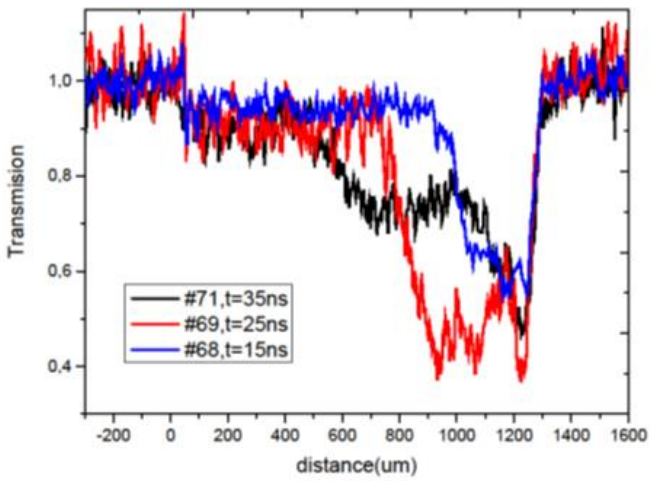

Fig4.1.13 Comparison of 3 shots transmission profile with different delay

Next step of analysis was to do hydrodynamic simulation. A hydrodynamic code is a computational program which solves fluids equations which control the material in experimental conditions. The object is split into cells. The physical parameters are computed from the equations and are taken as constants inside each cell. To prevent significant errors and keep the actual accuracy of the simulation, the variation of the values must be under control. The hydrodynamic codes are typically 1D or 2D. Because the variation only occurred along one axis, the computational time is decreased when the 1D approximation is used. A normal variance occurs in the 2D case, which produces a notable increase in computing time.

MULTI1D is a 1D Lagrange implicit code developed by [Ramis et al,2009]. Multi means Multigroup radiation transport in multilayer foil target. A physical quantity in this code at time n (discrete time) is a function of the values of the same quantity at the time n-1 and n+1.In this sense possible to say that MULTI is a implicit code. This characteristic makes code numerically more stable than an explicit code where a value at n a function only of value at n-1. The hydrodynamics equation is assumed to have a simple form because the use of Lagrangian coordinates assumes the absence of matter flakes between adjacent cells. SESAME or MPQueos are two examples of external thermodynamic tables that are used to explain the properties of the materials. We can recognize two regions in the plasma in the simulation

- ✓ Plasma corona the electrons take the energy from the laser beam and through the collisions heat the ion until the equilibrium
- ✓ Shock front matter is set into motion by ion wave and electrons are by the collisions

MULTI give possibility to simulate multilayer targets. Every layer is described by the thickness, atomic and mass number of the material used and geometry of the mesh. To achieve numerical stability, the distribution of mass must be smooth cell by cell. Where layers of various materials are employed, this is

critical. To assure a correct distribution of the laser absorption, the next cell must be ten times smaller than the laser wavelength.
In MULTI code can be chosen different laser profiles (in time):

- ✓ Gaussian
- ✓ Linear
- ✓ Flat top

Profile can be set by user to describe better the experimental situation if an experimental measure of the pulse duration is available.
The variables calculated step by step by Multi are

- ✓ Density
- ✓ Temperature
- ✓ Pressure
- ✓ Position in the lab frame

In some situations, it could be possible to make some approximations to simplify the problem solution easier. Use of 1D hydrodynamic codes like MULTI 1D is allowed by the 1D approximation. Compared to the 2D case, this type of situations computing time is significantly less. This approximation works well when the target is thin and the laser focusing spot is large. The 2D effects and the shock wave divergence become negligible under these conditions. The entire energy transferred in normal direction, and shock wave are strong as we can see from the simulations which predict high pressure and temperature. On the other hand, if we assume that 2D expansion is actual, energy isn't just moved in one direction. Due to the shock wave's divergence in this case, energy is lost in the transverse direction. The relaxation wave, which comes from the front side when the laser turns off, is another significant effect that lowers pressure. We applied both 1D and 2D hydrodynamic simulation in our situation.

In the 1D radiative hydrodynamic simulation of the target compression, the MULTI-1D code [Ramis et al, 2009] was utilized. The purpose of this simulation was to gain a better understanding of the experimental results obtained. The temporal profile of the laser used in the simulation followed a Gaussian distribution with a pulse duration of 2 ns.

To accurately model the target in the simulation, the relevant material properties were incorporated using the SESAME tables. The target consisted of different materials, namely CH (plastic foam), Ti (titanium), and TMPTA (a specific material). The densities and thicknesses of these materials in the target are depicted in Figure 4.1.14.

The simulation employed an intensity value $I = 2*10^{13}$ W/cm^2.that corresponded to the experimental conditions. This allowed for a comprehensive analysis of the target compression dynamics, including the effects of radiation and hydrodynamics.

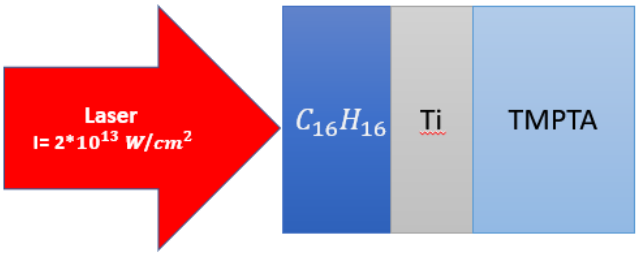

Fig 4.1.14 Model of the target used for MULTI 1D simulation layer $C_{16}H_{16}$ had thickness 25um, thickness of Ti equal 5 um and thickness of TMPTA($C_{15}H_{20}O_6$) was 1000 um. Laser intensity was used 2*10^{13}W/cm^2

The comparison between the hydrodynamic simulation and the real experimental data was conducted to assess the agreement between the two. In Figure 4.1.2, shots with different shock distances were marked, while shot #68 and #71, with energy ranging from 600-650J, were denoted by violet dots. Shot #69, with energy between 550-600J, was represented by a red square. It is important to note that these marked shots also had different time delays.

The presented simulation results demonstrate a good agreement with the experimental data. This agreement indicates that the hydrodynamic simulation successfully captured the behavior and characteristics of the shockwave propagation observed in the experiments. The simulation provides valuable insights into the physical processes involved and helps validate the experimental findings.

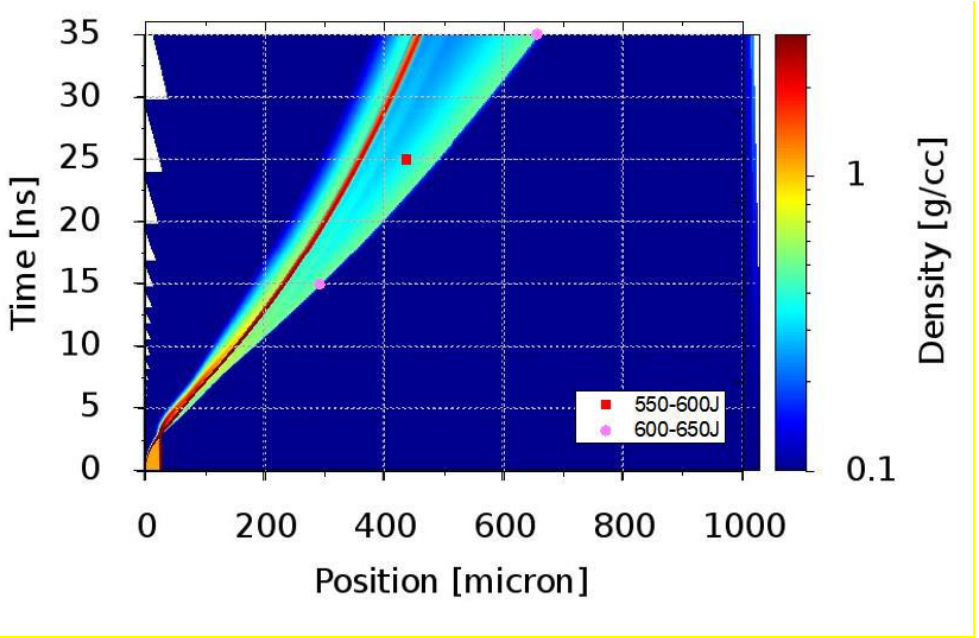

Fig4.1.15 Radiative hydrodynamics using MULTI 1D with I= 2*10^{13} W/cm^2 by the violet dote marked shot with energy 600-650 J by red square marked shot of energy 550-600J

The one-dimensional hydrodynamic simulation performed using the MULTI-1D code is presented in Figure 4.1.15. The comparison between the numerical simulation and the experimental results shows a clear agreement. The intensity profile in the simulation matches well with the real intensity observed in the

experiment. This agreement further validates the accuracy of the simulation and its ability to capture the key features of the experimental setup and dynamics.

Furthermore, the preliminary two-dimensional (2D) simulation results are also presented in subsequent figures. These 2D simulations provide additional insights into the complex behavior of the system and offer a more comprehensive understanding of the shockwave propagation and other relevant phenomena. These results contribute to the overall analysis and interpretation of the experimental data, allowing for a more complete characterization of the system under investigation.

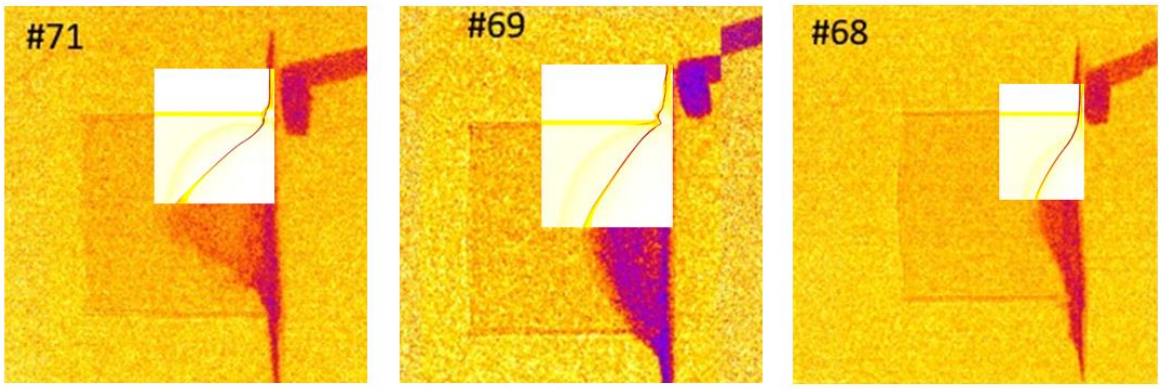

Fig4.1.16 Comparison between two-dimensional hydro simulation and real radiography experimental result performed in this figure. Numerical calculation was done using Gaussian shape of the laser. For shot #68 and 71 FWHW is 300um and $I=5*10^{13}W/cm^2$.FWHM=400um and $I=5*10^{13}W/cm^2$ for shot #69

2D hydro simulations were done using code MULTI2D. In simulation we used target with geometry like presenting in fig4.1.16. TMPTA thickness in calculation was 800um instead of 1000um to decrease time spend for simulation. This assumption possible to do because shock didn't reach last 200um of the foam target. This fact clearly shown in table4.1.2. Gaussian shape of the laser was used in two-dimensional hydrodynamic simulation. We simulate different value of intensity and FWHM. Intensity at all simulated shots was around $\sim 10^{13}$ its smaller than nominal one what is typical for hydrodynamic simulation. In shots #69 and #71 value of laser intensity was equal $1.5*10^{13}W/cm^2$. FWHM equal 300um was used in shots #68 and #71 also FWHM equal 400um for shot #69. These values are consistent with the experimental ones. In simulation presenting different value of FWHM its possible because of main beam consist of 3 beams with different energy which reach the target in a same time. Its can be reason to have different focal spot size shot by shot. Pusher is observed in shots #69 and #71.

In order to study the effects of including a polyimide tube in the target configuration, a two-dimensional simulation was conducted. The scheme of the target, including the polyimide tube, is presented in Figure 4.1.17. The polyimide tube had a thickness of 50 μm and was filled with TMPTA foam.

By incorporating the polyimide tube in the simulation, the behavior of the shockwave and other relevant dynamics can be examined with respect to this

additional component. This allows for a more comprehensive understanding of the system and provides insights into how the presence of the polyimide tube influences the overall behavior of the experiment.

The results of this two-dimensional simulation, taking into account the polyimide tube, provide valuable information for further analysis and comparison with the experimental data. It helps to assess the impact of the tube on the shockwave propagation, density gradients, and other relevant parameters, enhancing the understanding of the system's behavior.

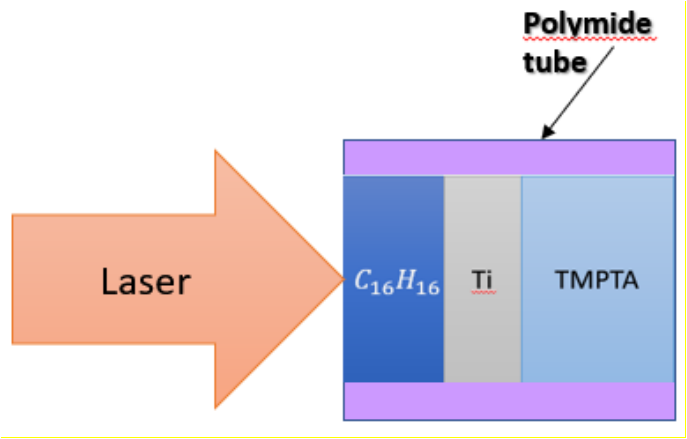

Fig 4.1.17 Target outline for hydrodynamic simulation layer $C_{16}H_{16}$ had thickness 25um, thickness of Ti equal 5 um and thickness of TMPTA($C_{15}H_{20}O_6$) was 800 um. Polyimide tube ($C_{35}H_{28}N_{207}$) wall thickness is 50um.

The simulation of the full geometry of the target was conducted, taking into account all the relevant components and structures present in the experimental setup. This includes the polyimide tube, foam material, and any other features that were part of the target configuration.

After the simulation, an Abel inversion technique was applied to the data in order to obtain a clear visualization of the shock region and the border of the target. Abel inversion is a mathematical algorithm used to reconstruct the radial distribution of a quantity based on its integrated projection.

The specific formula used for the Abel inversion depends on the details of the simulation setup and the data obtained. Typically, the inversion process involves calculating the inverse Abel transform of the integrated data, which allows for the reconstruction of the radial distribution of the desired quantity.

By applying the Abel inversion, the simulation results can be further analyzed and visualized to gain insights into the shock region and the overall behavior of the target. This helps to compare the simulation results with experimental data and validate the accuracy of the simulation model.

$$I = I_0 \cdot exp\left(-2\int_y^{\infty} \frac{\left(\frac{\mu_0}{\rho_0}\right)\rho(r)rdr}{\sqrt{r^2 - y^2}} \right) \quad (4.9)$$

Where ρ is the mass density, I_0 is the initial intensity, I is the intensity on the image, $\mu(r) = (\frac{\mu_0}{\rho_0})\rho(r)$ is linear absorption coefficient.

In figure 4.1.18, the simulation results clearly depict the region with the pusher and the shock wave. After applying the Abel inversion technique, it becomes possible to observe the formation of the shock wave near the edge of the target and close to the border of the polyimide tube. This is consistent with the experimental imaging, where the shock wave was observed to propagate initially outside of the tube.

The visualization provided by the simulation results helps to understand the dynamics of the shock formation and its interaction with the various components of the target. By comparing the simulation with the experimental data, valuable insights can be gained regarding the behavior of the shock wave and the effects of including the polyimide tube in the target configuration.

Overall, the simulation results and the Abel inversion analysis contribute to a comprehensive understanding of the shock dynamics and the role played by the different components of the target.

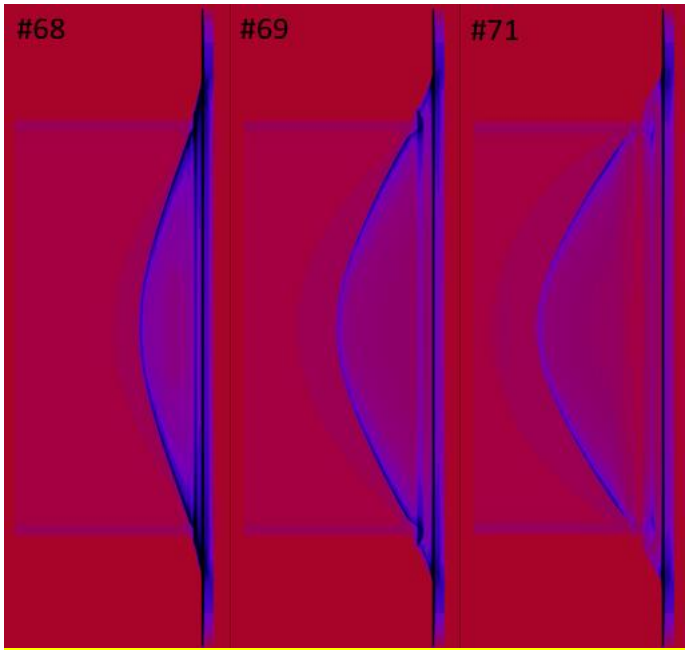

Fig 4.1.18 MULTI 2D hydrodynamic simulation with done Abel inversion. Shots with different time duration 15ns,25 and 35ns. Gaussian pulse shape. For shot #68 and 71 FWHW is 300um and I=10^{13}W/cm^2 and I=1.5*10^{13}W/cm^2.FWHM=400um and I=1.5*10^{13}W/cm^2 for shot #69

The simulation results, as you mentioned, indicate that the presence of the tube has a negligible influence on the propagation of the shock wave. This finding aligns with the experimental observations, where the position of the shock wave in

the radiography images corresponds to the simulated results. The presence of the pusher is also clearly observed in all shots, further confirming the accuracy of the simulation in capturing the dynamics of the target.

The agreement between the simulation and experimental results reinforces the validity of the simulation model and its ability to accurately represent the physical processes involved. This consistency provides confidence in the simulation as a tool for studying and analyzing the behavior of shock waves and the interaction of various components within the target.

Overall, the simulation results, when compared to the experimental data, demonstrate a close correspondence and support the conclusion that the inclusion of the tube has a negligible influence on the propagation of the shock wave, while accurately capturing the position of the shock and the presence of the pusher.

In the current experimental campaign, a bremsstrahlung cannon (BSC) was utilized as a diagnostic tool to characterize the temperature of hot electrons. A detailed description of this diagnostic can be found in Chapter 2 of the research work.

The BSC was installed inside a vacuum chamber, and there was a distance of 35 cm between the target chamber center (TCC) and the spectrometer. Additionally, a magnet was positioned near the BSC to prevent electrons originating from the target from reaching the spectrometer. This setup ensured the accurate measurement and characterization of the hot electron temperature during the experiments.

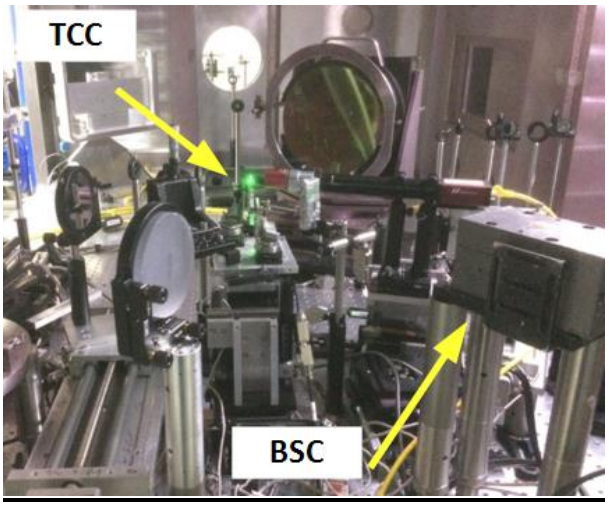

Fig 4.1.19 Position of bremsstrahlung spectrometer in VULCAN vacuum chamber

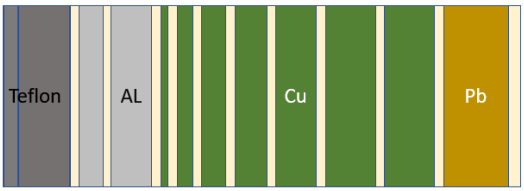

Filter	Teflon	Teflon	Al	Al	Cu	Cu	Cu	Cu	Cu	Cu	Cu	Pb
Thickness (mm)	6	267	2.0	4.0	0.3	0.5	1.0	1.5	2.0	3.0	4.0	1.0

Fig 4.1.20 Characteristics of the filters composing bremsstrahlung cannon used in our experiment on VULCAN laser facility

Based on the information provided, it appears that the experimental campaign used MS type imaging plates (IP) with thick lead housing, which were sensitive to X-rays in the energy range of approximately 20-150 keV. The transmission characteristics of the filters used in the spectrometer are shown in Figure 4.1.20. The experiment was conducted in a single-shot regime, and the scanner operated with settings S=4000, L=5, and B=16 bits.

The fade time, which refers to the time it takes for the imaging plate to lose a significant portion of its stored energy after exposure, was noted to be between 25-45 minutes at a temperature of 20 degrees for each shot.

The results obtained from the experiment were analyzed using both GEANT4 Monte Carlo simulation and a simple semi-analytical method. The details of both analysis methods are described in the corresponding chapter of the study.

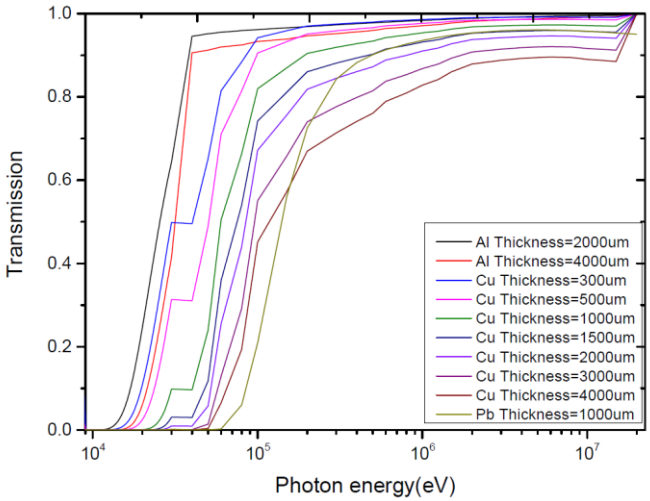

Fig 4.1.21 Transmission of the materials composing the bremsstrahlung cannon filters in Vulcan experimental campaign

Analysis for shot #69 and #71 is presenting behind.

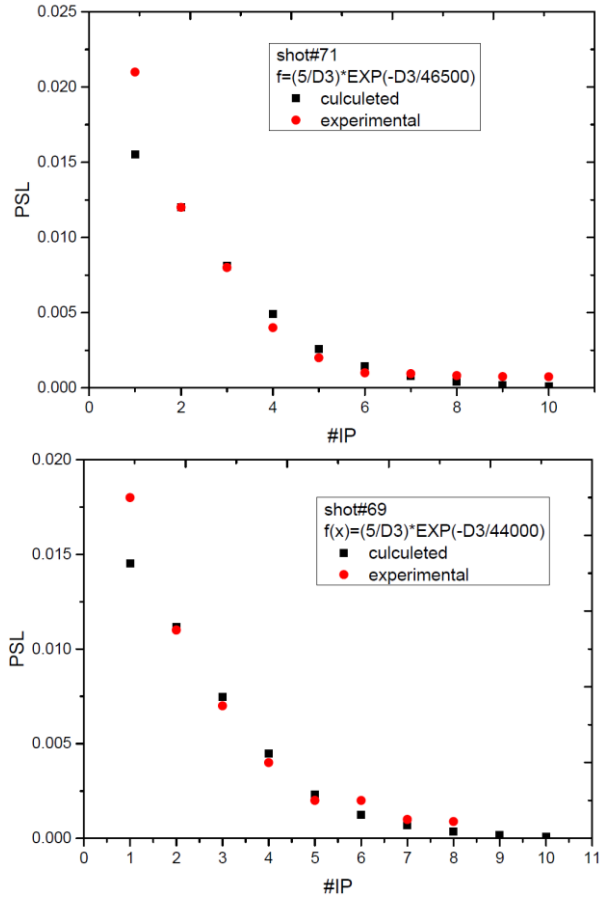

Fig 4.1.22 result obtain for the shot #69 and #71. Photon temperature 46.5 and 44keV was calculated. Two methods give same result.

In the analysis, the calculated and experimental PSL (photostimulated luminescence) values were compared, and the results are presented in Figure 4.1.22.

The photon temperature, which represents the effective temperature of the X-ray photons, was determined to be 46.5 keV in the calculated results and 44 keV in the experimental measurements. The comparison of these values provides insights into the agreement between the simulation and the actual data obtained from the experiment.

4.2 GSI WIRE EXPERIMENT

The experimental campaign in this chapter was prepared and performed in collaboration with CELIA, University of Bordeaux (France), University of York (United Kingdom), GSI Helmholtzzentrum fur Schwerionenforschung (Germany), National Research Nuclear University MEPhI (Russia), CLPU, Salamanca Spain.

4.2.1 Phelix laser

The Petawatt High-Energy Laser for Heavy Ion Experiments (PHELIX) is a laser facility, at GSI Darmstadt (Germany), delivering intense laser beams with energies up to 1 kilojoule. PHELIX employs two frontends (nanosecond and femtosecond frontend), a pre-amplifier and a main amplifier. The nanosecond fontend is used generating high energy beams, which delivers arbitrary pulse shapes and pulse durations between 1 and 10 ns. The femtosecond frontend is coupled to a chirped pulse amplification scheme, where a femtosecond laser pulse is stretched in time, amplified, and recompressed generating pulse laser with intensities $>10^{20}W/cm^2$. Table 4.2.1. shows the main parameters of the laser. The dual front-end architecture of PHELIX allows versatile generation of high-energy pulses of multi-nanosecond duration and likewise high-power pulses of sub-picosecond duration. In the nanosecond-pulse configuration, a fibre-based front-end with an integrated pulse shaper is used to inject a glass regenerative amplifier. The laser beam is then further amplified through a pre-amplifier and double passes the main amplifier where its energy reaches 500 J. In the sub-picosecond pulse configuration, a 10-Hz-repetition-rate laser front-end producing 30-mJ spectrally-broad pulses seeds the PHELIX glass amplifier. The short pulses are generated by a commercial short pulse oscillator, they are then stretched by 200 ps/nm in a tenable pulse-stretcher. In this way, the stretcher can be adjusted to the compressor, greatly reducing the complexity of its operation.

	Long pulse	**Shot pulse**
Frontend	nanosecond	Femtosecond
Wavelength	1064ns	1064ns
Pulse duration	1-10ns	0.5-20ps
Pulse energy	25-30 J	25-30J
Intensity	$10^{16}W/cm^2$	$10^{21}W/cm^2$

Table 4.2.1 Parameter of Phelix laser facility available in a vacuum chamber

For the experiment described in this chapter, a double-beams configuration was used. One is “heater” other “backlighter” The parameters of the two beams are equal, time duration 0.5 ps, pulse energy 50 J, ~10 μm focal spot, high-contrast.

Backlighter was illuminated the tungsten wire to generate broadband spectrum. The P-polarized laser pulse was incident on the target at 22.5°, delivering a maximum energy of 210 J in ~0.4 ps and was focused using a f/3 off-axis parabola to a minimum focal spot of ~7 μm in diameter. On target, the nominal laser spot included 40% of the laser energy, equal to a maximum intensity with around 6×10^{20} W/cm^2 on target. Total power is about 0.5 PW. The use of an ultrafast parametric amplifier before the main amplifier allowed for a main pulse to laser pedestal contrast of more than 10^{10}, assuring that no long-scale length preplasma formed in front of the solid target. "Heater" was heat-up the titanium wire (illuminating the tip) via relativistic electron production [Neumayer,2005; Bagnoud,2010].

Goal of experimental campaign

The goal of experiment was to test X-ray absorption spectroscopy (XAS) and X-ray absorption near-edge spectroscopy (XANES) to investigate an isochorically heated wire by laser-accelerated relativistic electrons. In particular was characterized the energy deposition observing the Kα emission along the wire, and the later wire expansion at different time using X-ray radiography. While the diagnostic was able to measure temperature and density of the wire, XAS and XANES can measure the degree of order of the electronic structure for the warm dense matter. The use of the combination of all the techniques (X-ray spectroscopy, X-ray radiography, XAS and XANES) is crucial for a deep understanding of WDM and equation of state (EOS) measurements.

We used laser-accelerated relativistic hot electrons to heat thin titanium wire targets to a warm dense matter (WDM) state in a recent experimental campaign. Using spatially resolved X-ray emission spectroscopy and the Ti K_α characteristic lines, the WDM temperature profiles along several hundred microns of the wire were predicted. A maximum temperature around ~30 eV was reached.

4.2.2 Targetry

In presenting experimental campaign was used holder shown in fig 4.2.1 for main target and backlighter.

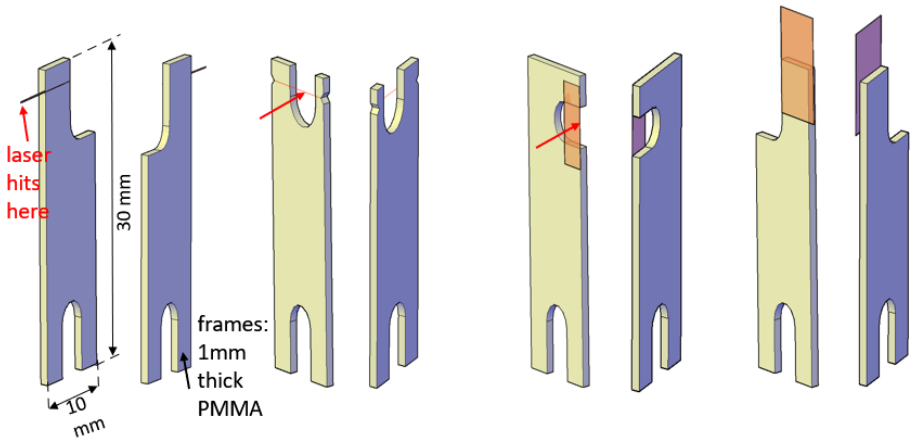

Fig 4.2.1 the holder for the target and back lighter is shown in image

The main target was a titanium wire with a diameter of 50 μm. We considered also smaller diameter such as 20 and 10 μm (to increase the transmission). As backlighter we used a tungsten wire of 5 μm diameter, already used in the previous campaign. For the proton radiography we used thin metallic foil.

When compared to thin foil, employing a wire target has several benefits for study of electron propagation. [Schoenlein,2016; Zastrau,2010]

1. First, if the wire is long enough, it releases the constraint upon the laser prepulse.
2. Second, whereas relativistic electrons can heat the target along hundreds of microns in several hundreds of fs, laser heating (up to several keV) takes over several microns near the critical density surface, meaning they are the only ones governing heating of the target deep along the wire.
3. Thirdly, the radial electrostatic field produced by the charge separation is strong enough to confine most of the hot-electron population for a wire radius equal to the electron source. The energy flux is hence constrained to flow along the wire. By contrast, in the case of planar targets, the electron current density rapidly decreases with target depth because of the natural divergence of the fast electron beam. Far from interaction region the heating of target by hot electron propagation rapidly become negligible. A high current density is kept in the wire even at large depths (along hundreds of microns).

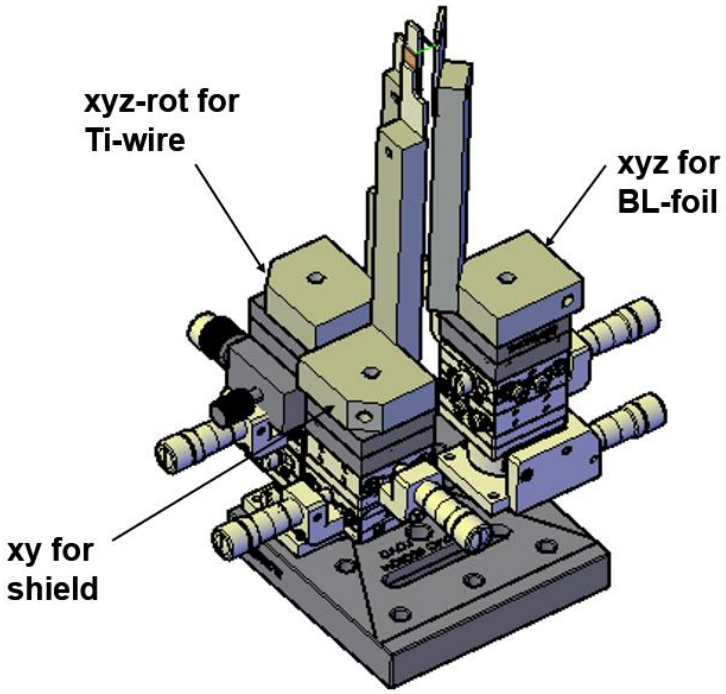

Fig4.2.2 Scheme of motor for alignment main target and backligter

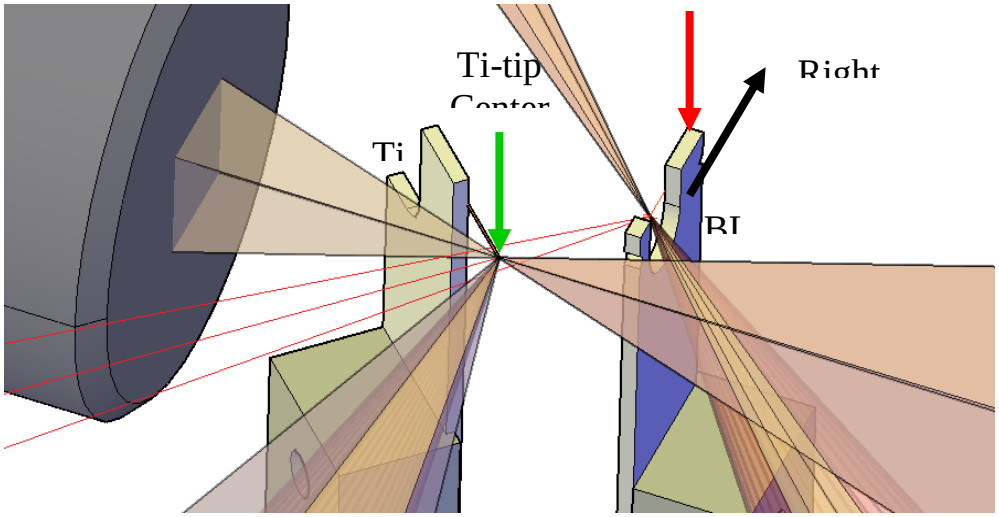

Fig 4.2.3 In a picture is shown position of main target and backlighter in microscope with direction of alignment

For alignment procedure was used microscopes which is located on Phelix target aria. The XYZ translation stage holding the microscope. The motorized stages are moving the targets holder up and down. Main target and backlighted target should be aligned in a same time.

4.2.3 Set -up

The setup of experiment can be observed in figure 4.2.4. RPP was used in this campaign.

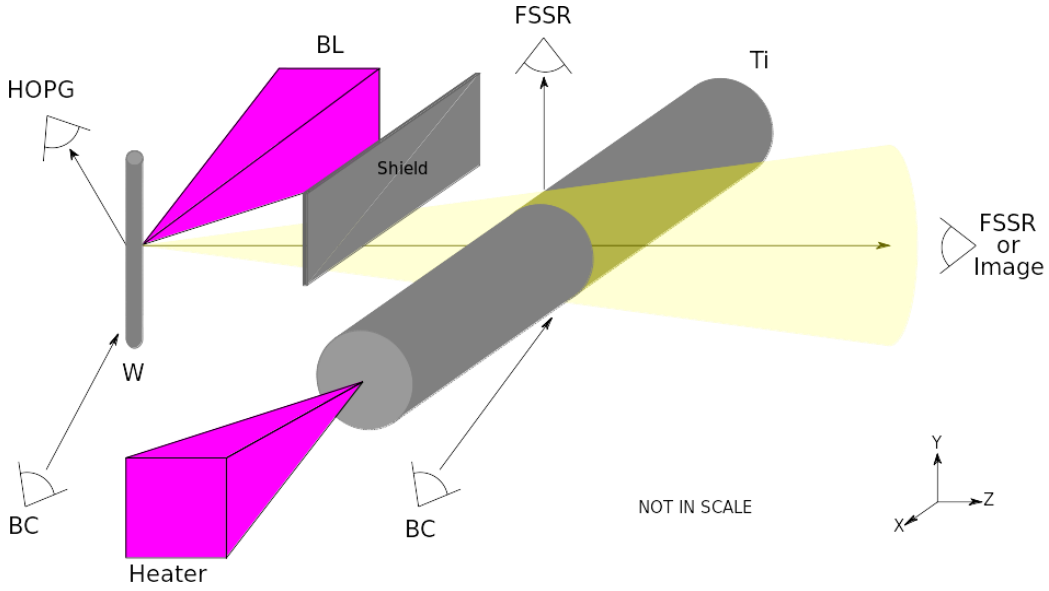

Fig 4.2.4 experimental set up

During experimental campaign in PXELIX laser facility was used set of diagnostics. Description is below.

X-ray emission spectroscopy: We was detected the emitted K_α along the wire using focusing spectrometer with spatial resolution (FSSR). The measurement used to estimate penetration of hot electrons and the temperature along the wire. of the spectrometer configuration is shown in Fig 4.2.5. FSSR spectrometer, which employs a spherically bent -quartz crystal with Miller indices 211 (2d = 3.082) and a radius of curvature R = 150 mm to record WDM emission. It was developed to regularly record X-ray emission with high spectral resolution in a spectrum range of 2.45–2.8 (4.4–5.1 keV), including Ti XXII (Ti21+) Ly, Ti XXI (Ti20+) He, and Ti K1, K2 characteristic emission lines, the axis wire is perpendicular to the page, the source (back-lighter) and target are both located inside the Rowland target. This verified that all X-ray wavelengths were able to penetrate the full wire section.

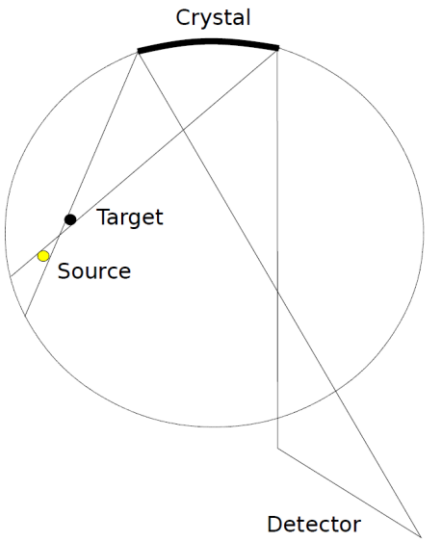

Fig 4.2.5 The Rowland circle is used to configure the spectrometer.

With a magnification factor of 0.3, the spectrometer provided a spatial resolution of a few mm along the wire's Z axis and a field of view of a few mm. X-ray films were used as detectors. X-ray films were chosen as detectors because they had a high spatial resolution (20 um) and a high spectral resolution ($\lambda/\delta\lambda \sim 3000$).

X-Ray absorption spectroscopy: This was the main diagnostic of the experiment. We used a spherically bent crystal to record the transmitted X-ray signal through the wire from the X-ray source generated by the second laser beam with the tungsten wire.

Radiography set up shown in figure below. We used SR imagine plate as a detector.

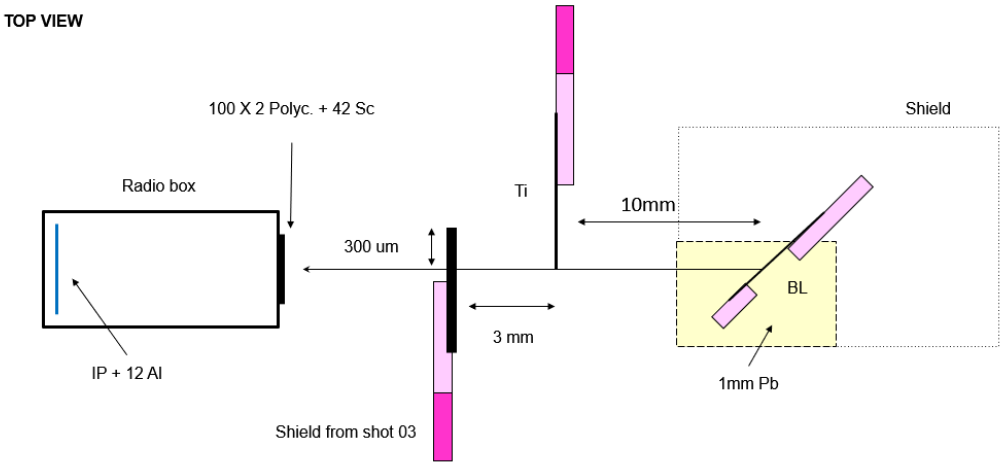

Fig 4.2.6 Top view of radiography setup

Bremsstrahlung cannon: This diagnostic was used to measure the temperature of the fast electron distribution. A second cannon was used to monitor the emission from the X-ray source.

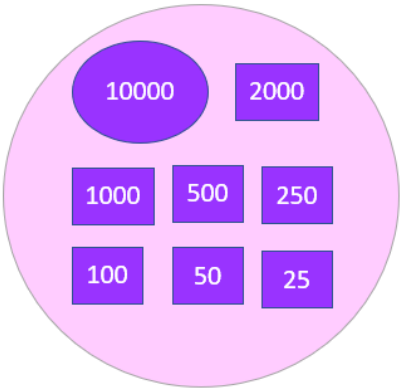

Fig 4.2.7 Characteristics of the filters that present the bremsstrahlung cannon performed in our Phelix laser experiment (um units)

The Bremsstrahlung cannon consist of tantalum filters with thickness 25, 50, 100, 250, 500, 1000, 2000 and 10000 microns. SR type of IP was used. Plastic 1.3 cm and 100 micrometres shielded with a thick piece of plastic (4mm) plus 2 millimetres of led were installed before filters.

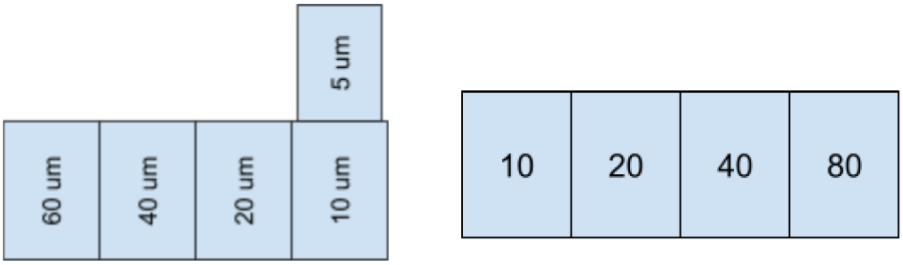

Fig 4.2.8 Characteristics of the filters composing bremsstrahlung cannon used in our experiment on Phelix laser facility to detect emission from X-ray sours.

During the experiment, two sets of filters were utilized. The first set consisted of wedge step filters, which were also installed in front of the IP-radiography, specifically designed to correspond to the Bremsstrahlung spectrometer (BSC) and measure the emission from the X-ray source. These filters were attached to a polycarbonate plate with a thickness of 100 micrometers. Prior to the filters, a 3 mm thick plastic material was used as an additional barrier.

In terms of the setup, a magnet was installed at a distance of 27 cm from the TCC (Target Chamber Center) to prevent electrons from the target from reaching the spectrometer. The distance between the first IP (Image Plate) and the TCC was consistent at 60 cm for both cases of the Bremsstrahlung spectrometers.

By utilizing these filters and maintaining specific distances within the setup, the experiment aimed to effectively measure and characterize the emissions from the X-ray source using the Bremsstrahlung spectrometers.

4.2.4 Result

A deep knowledge of matter behavior in extreme pressure and temperature conditions is mandatory to describe a lot of phenomena, like inertial fusion in particular fast ignition and shock ignition research, astrophysical phenomena, and all the physics of laser-driven radiation and particle sources [Betti,2016;Batani,2014;Mourou,2006;Bailey,2015;Nahar,2016;Drake,2018].Such extreme states of matter are usually referred to as WDM (warm dense matter) and HED (high energy density). WDM is typically defined as matter having a density of 0.1–100 g/cm3 and a temperature of 1–100 eV, equivalent [Batani,2016].

Thin titanium wire targets were irradiated on their tip by a high-intensity optical laser resulting in electron acceleration up to relativistic energies. These hot electrons (HE) propagate along the wire for 100s um, producing inner-shell ionization of Ti atoms and the emission of the X-ray Ti K_α line. At the same time, the hot electrons passing across the wire draw a low-energy electron return current [Tikhonchuk,2002]. When both currents are combined, matter can be heated to a few tens of eV. Most crucially, heating and ionization processes is happened faster (1 ps) than the wire's hydrodynamic expansion (10 ps), hence the volume is same during heating.

Shot	Energy	Focal spot size	Pulse duration	Intensity (*0.4)	T_{hot} (Beg's scaling law)
#	J	μm	ps	W/cm^2	MeV
1	50	30	0.5	$5.7*10^{18}$	0.4
2	190	30	1.9	$5.7*10^{18}$	0.4
3	200	30	1	$1.1*10^{19}$	0.5
4	210	7	0.4	$5.5*10^{20}$	1.8

Table 4.2.2 Laser pulse parameter used in our analyses. Set of the shot if the nominal focal spot contains 40 % of the laser's energy used for analysis.

The laser energy, focal spot size and pulse duration were changed to generate a range of shots with different parameters can be seen in Table 4.2.2. Figure illustrates the experimental setup.

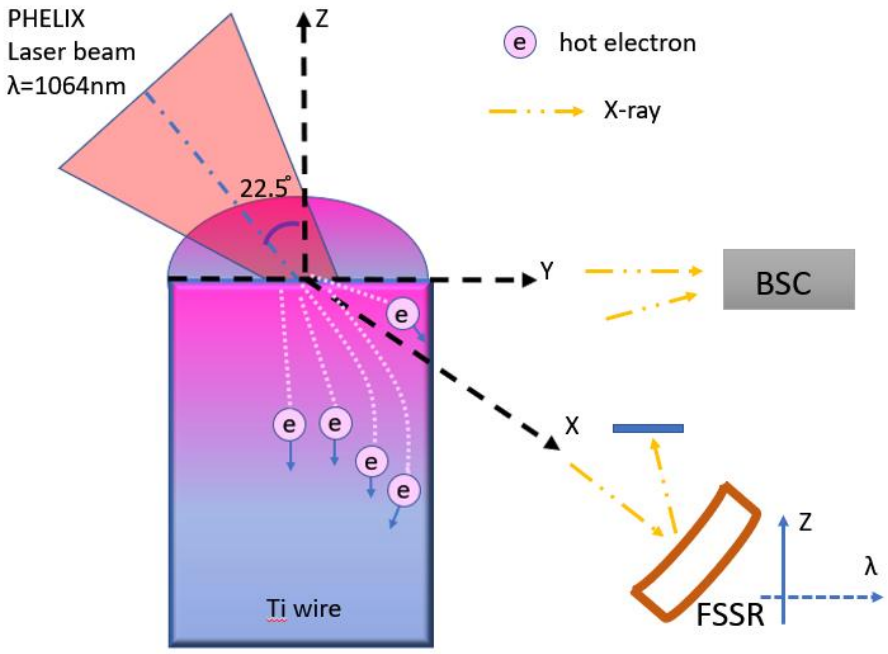

Fig4.2.9 Experimental scheme showing relativistic ps laser beam interaction with a 50 μm Ti wire tip and consequent isochoric matter heating by the laser-accelerated hot electron flow, resistive heating by return currents, and related processes. Laser plane of incidence (P-polarization one) coincides with YOZ plane. BSC and FSSR were placed in XOY plane as shown.

Based on a study of Ti Kα X-ray emission spectra taken with FSSR, the WDM temperature profiles were obtained. The HE energy distribution was calculated using a bremsstrahlung cannon spectrometer (BSC), with Monte-Carlo simulations and analytical method described in chapter 2. For performed calculation was used to side the incoming bremsstrahlung radiation produced by hot electrons. In current

experimental campaign, the BSC was able to detect the presence of hot electrons with energies ranging from 0.1 to 5 MeV.

As shown in Fig 4.2.9 an electron potential generated on the target surface prevents most of the HE from escaping. Heating of deeper-lying regions of the wire is generally caused by HE, return currents, and other processes, but ionization is assumed to be mostly induced by HE. However, due to a bulk conductivity process, the first few tens of microns of the wire were heated. As a result, the plasma in this region is highly ionized, having high temperatures with several hundred eVs. Since such temperatures are too high for the "neutral" K_α line to be emitted, the line may be seen in the temporally integrated spectra. The neutral K_α line in this case is most formed in the very early stages and comes from the relatively cold regions surrounding the hot focal spot. It's also important to remember that the first stage of electron propagation in the target, i.e. from the laser focal spot along the laser beam axis to the wire's edge, is not taken into account here. Although this process occurs on a wire diameter size (50 μm), it is difficult to separate from the hot plasma zone experimentally. Especially heating deeper than ~60 μm, where electrons are expected to move along the wire, is taken into consideration and described.

Profiles of Ti K_α were spatially resolved along the wire and compared to modeling spectra computed with the atomic-kinetic code PrismSPECT. PrismSPECT is a collisional-radiative spectral analysis code designed to simulate the atomic and radiative properties of laboratory and astrophysical plasmas.

However, it appears that SCFLY, which includes more atomic levels and configuration for low-charged ions with multiple bound electrons is more accurate in the atomic-kinetic modeling of X-ray spectra. As an outcome, only the results of experimental data processing with SCFLY are shown 4.2.10. The spectra were calculated using a 0.5 MeV HE fraction of 1 percent. In the range of 0.5–2.5MeV, spectral line profiles did not show any significant dependence on HE energy (which correspond to the range of hot electron energies in the performed experiment). As a result, we could analyze our experimental data from shots with different laser intensity using the same set of curves (i.e. regardless of the expected HE energy). The impacts from different stages of plasma expansion were time-integrated in all experimental spectra. Therefore, a two-temperature approach appeared to provide a reasonable description of experimental data.

The temperature of the WDM was calculated as the sum of comparatively low T_{low} and high T_{high} bulk temperatures (with a fraction of a = 0..1).

$$T_{bulk}^{avg.} = \alpha T_{bulk}^{low} + (1-\alpha) T_{bulk}^{high}, \quad (4.10)$$

was in range of 0.4-0.6 and dependents $\frac{T_{bulk}^{low}}{T_{bulk}^{high}}$ was about 1.5-2.For example,α=0.6 , $T_{bulk}^{low} = 20\ eV, T_{bulk}^{high} = 30eV$ calculated for the shot #3 at 100um.

The laser-target interaction point was defined as the area in space where Ti K_α total emission reaches its maximum and was set to "0 m" on the Z axis. The temperature profiles described in Ref. [Schönlein,2016] were recently claimed using a similar but simplified method. The temperature profiles observed and explained in fig 4.2.10.

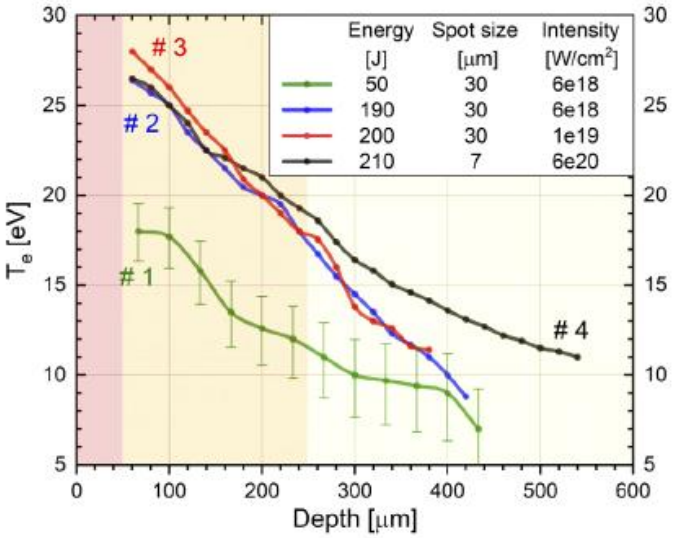

Fig 4.2.10 For the shots specified in Table 4.2.2, experimental temperature profiles of WDM produced inside the titanium were acquired through an examination of its K_α emission. Error bars are only shown for shot #1 to make comparisons simpler. Profiles were obtained along the axes OZ in Fig.4.2.10; "0 m" corresponds to the laser-target interaction point, however in the opposite direction [Martynenko,2021]

Influence of laser energy and intensity on laser accelerated HE energy distribution were discussed below. According to a semi-empirical scaling law, the general HE energy spectrum can be normally represented by a Maxwellian distribution with a characteristic temperature T_{hot} [Hutchinson,2002], which can be predicated on the laser intensity value. T_{hot} [MeV] = 1.01 $(I\lambda^2/10^{18})^{1/3}$ (4.10) (where I [W/cm^2] and λ[um] are, respectively, laser intensity and wavelength) was applied here as a modified version of Beg's law for high intensity range [Alkhimova,2018]. Black curve in fig 4.2.10 is used to represent it. Then, increasing laser intensity while keeping a constant laser energy result in increased in T_{hot} and the corresponding HE energy redistribution. The total energy deposited to the HE component increases as laser energy is increased while keeping a constant laser intensity, however T_{hot} is not significantly changed. As a result, should be predict a more effective target heating with same T_{hot}. Let's compare 2 separate experimental shots (#1 and #2 in Table 1) in which the laser energy was changed while the laser intensity remained constant to show the validity of these statements. Here, the laser energy varied by a factor of four, the focus point remained unchanged, and the laser intensities were assumed to be constant by adjusting the laser pulse time, as shown in Table 4.2.2. Figures 4.2.11 (a) and (b), which illustrate the HE temperature and complete energy for these shots,

respectively. Although that T_{hot} values for the two shots are about similar within the measurement's accuracy, the low-energy shot #1 generated almost half as much HE as the high-energy shot #2. The green and blue curves for shots #1 and #2, correspondingly, in figure 4.2.10 demonstrate how this has some effect on the temperature profile of hot matter. The two profiles visibly lie in different temperature regions. For the low energy shot #1 and the high-energy shot #2, the maximum temperatures at 60 um depth are approximately 18 and 28 (1.5) eV, respectively. In both profiles, the WDM temperature is seen to decline linearly up to a maximum visible heating depth of about 400 um. Due to the low signal-to-noise ratio in this area, a similar dynamic was not experimentally demonstrated, although it is predicted for deeper lying layers (depth > 400 um). The experimental results supported what we had said about how laser energy affects HE temperature and full energy.

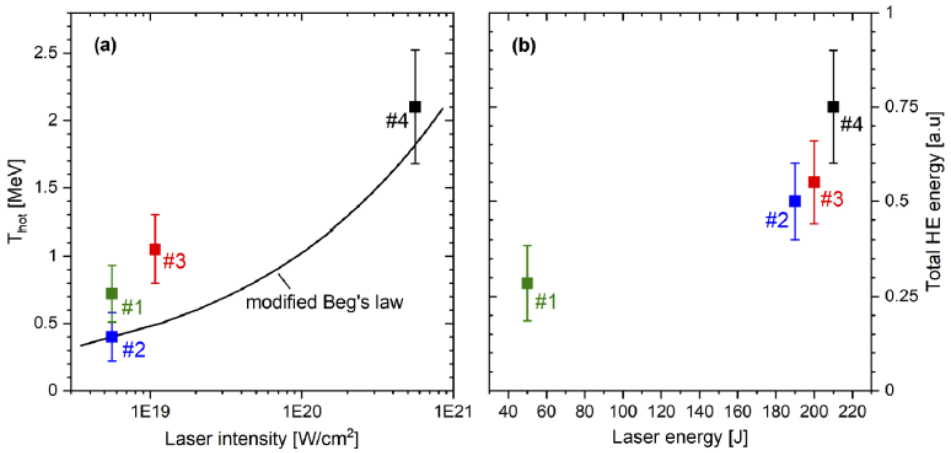

Fig 4.2.11 (a) Hot electron temperatures and (b) total hot electron energy for the shots listed in Table 4.2.2. Experimental values were revealed based on a bremsstrahlung cannon spectrometer and are marked with black dots. The black curve corresponds to the modified semi-empirical Bag's law. [Cui,2013]

Target heating responds variably to changes in laser intensity. Comparing the experimental outcomes (temperature profiles) for shots #2 and #3 in fig. 4.2.10 clearly demonstrate this. Here, the laser energies were approximately constant while the laser intensities were adjusted by a factor of two, $I_2/I_3 \sim 2$ and $E_3 \sim E_2$. We could see that throughout the whole observed region, the temperature profiles are almost comparable. This is also consistent with the HE criteria that the BSC showed. As seen in Fig. 4.2.11(a) and 4.2.11(b), HE electron temperatures and full energy are equal within measurement error bars (b). This demonstrates that, at least for the range of intensities taken into account, doubling the laser intensity is insufficient to significantly the amount of energy deposited by HE, i.e. to increase WDM temperature and depth of heating. We apply a basic physical approach that takes into account the interaction of HE of different energies with matter to provide a fundamental interpretation and qualitative description of the discussed experimental data. We used Monte-Carlo GEANT4 [Agostinelli,2003; Batic,2013] simulations to take into account heating a Ti solid-state, laterally infinite material block with HE of

various energies injected opposite to the target surface. Electric potential generated on the target surface prevents HE from fleeing and guides them to proceed along the wire, even if initially in the experiment HE starts to propagate with some angular distribution along a laser axis [Pompili,2016]. We therefore simulate the process by injecting HE without initial divergence, considering HE propagation and matter heating many hundreds of microns deep into the target. The energy deposited in solid Ti by Hs of different energies is illustrated in Figure 4.2.12(a) as a function of depth. The collisional frequency of HE decreases with increasing HE energy [Jackson,1999]. It is obvious that as HE energy increases, the depth corresponding to peak energy deposition increases, while temperature profiles smooth out. Figure 4.2.12(a) demonstrates that HEs with energies below 1 MeV must be the main source of heat for matter up to a depth of approximately ~250 um. Target regions heated mostly by HEs with energy > 1 MeV are indicated by a deeper lying target region that is highlighted in yellow. According to Beg's law, the T_{hot} value increases with laser intensity. The number of relatively high energy HEs increases for higher values of T_{hot}, even though low energy electrons always prevalent in the electron energy spectrum. This is demonstrated in Figure. 4.2.12(b), which shows the dependence on depth of energy deposited by HE fluxes with a Maxwellian distribution for different T_{hot} (the total electron energy was set to be the same for all curves). It is evident that for very slight increases in T_{hot}, the temperature curves for T_{hot} 1MeV do not significantly change (i.e. of laser intensity).

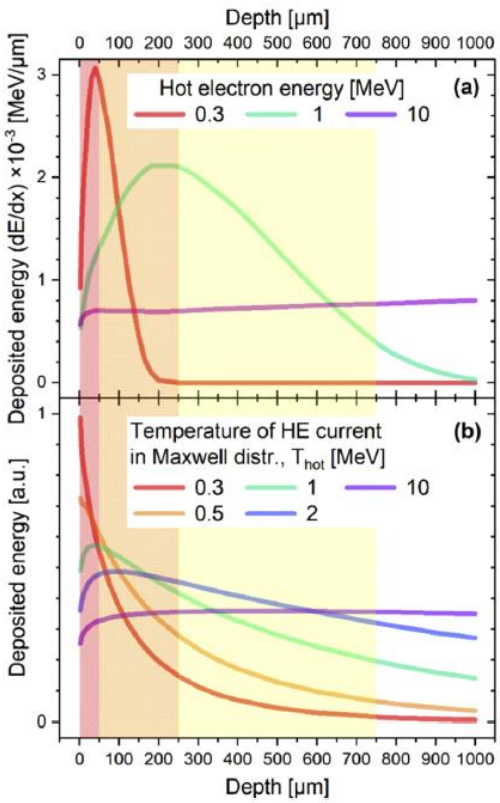

Fig4.2.12 (a) Dependence of energy deposited in solid-state Ti by single hot electrons on the layer depth calculated in GEANT4 took it for various hot electron

energies. (b) Calculated total deposited energy in solid-state Ti by a hot electron current having a single-temperature Maxwell distribution energy spectrum. Total electron energies were set to be the same for all cases. The target was considered as a solid-state, laterally infinite material block. The effect of the confinement of hot electron flow due to the wire geometry was not considered.

One can got changed in the WDM temperature profile and an effective heating of the target to deeper lying layers when the laser intensity is increased even more (while keeping the laser energy on target). This can be seen by contrasting the green and blue curves in Fig. 4.2.11 for T_{hot} = 1 and 2 MeV. The energy deposition is approximately the same between 0 and 300 um, however between 300 and 1000 um, the change is more obvious. These predictions are supported by the experimental temperature profiles for shots #2 and #4. I_4/I_2 ~100 and E_4~E_2 were used to increase the laser's intensity while keeping the energy constant. The measured T_{hot} values for shots #4 and #2 were 2.1 (0.4) and 0.4 (0.2), respectively. The predicted HE full energy is in general agreement with Beg's rule, as shown in Fig. 4.2.11(a)). Fig. 4.2.11 for changes of a factor of 1.5. (b). These shots WDM temperature profiles are identical. In figure 4.2.10 can be observe details. Within the measurement's accuracy up to depths of about ~300 um. This demonstrates that WDM temperature profile is not significantly impacted by laser pulse intensity. The heating depth is also significantly higher for high intensity shot #4 than it is for shot #2 (see the range of ~300-550 um in Fig. 4.2.10) at the same time. and the WDM temperatures, 14 and 10 eV for shots #4 and #2, respectively, differ noticeably at 400 um depth. This demonstrates that higher laser intensity results in higher heating depth and typically smoother profiles. Future experiment design is made suitable and acceptable by the approach we used to explain why temperature profiles depend on laser intensity and energy. The dynamics and observable influence of WDM temperature profiles on laser parameters are both well-described generally. The description of target edges and other related effects, such as the presence of induced surface currents and self-generated electromagnetic fields, their influence on electron current, the temporal evolution of these processes, etc., were left out. We specifically ignore the collimating effect is caused by the wire's limited shape. These combined effects would influence how deeply HE penetrates materials, how far they can stop, and finally how much energy they deposit. The results made in this work about the relative changes as a function of laser energy and intensity, however, we believe will remain true. In any case, it is very interesting to construct full computational models explaining HE generation, penetration, and heating of materials, and the experimental findings in our work may be used to verify such models. In work [Schönlein,2016], these impacts were in fact at least partially considered. It is important to note that the discussed experimental results and simplified physical approach. Additionally increasing the laser intensity while keeping the same energy level is estimated to result in a significant increase in the heating depth and a slight change in the maximum WDM temperature. Our studies also point to the possibility of adjusting the laser pulse characteristics to produce a particular desired WDM

temperature profile. The WDM temperature increased in the first few hundred μm in diameter of the target if the wire tip is coated with a high-Z material, which may result in the simultaneous decrease of T_{hot} and increase of HE number. The most effective method of raising the wire WDM temperature, although being in practice a very expensive option, is to increase the deposited laser energy.

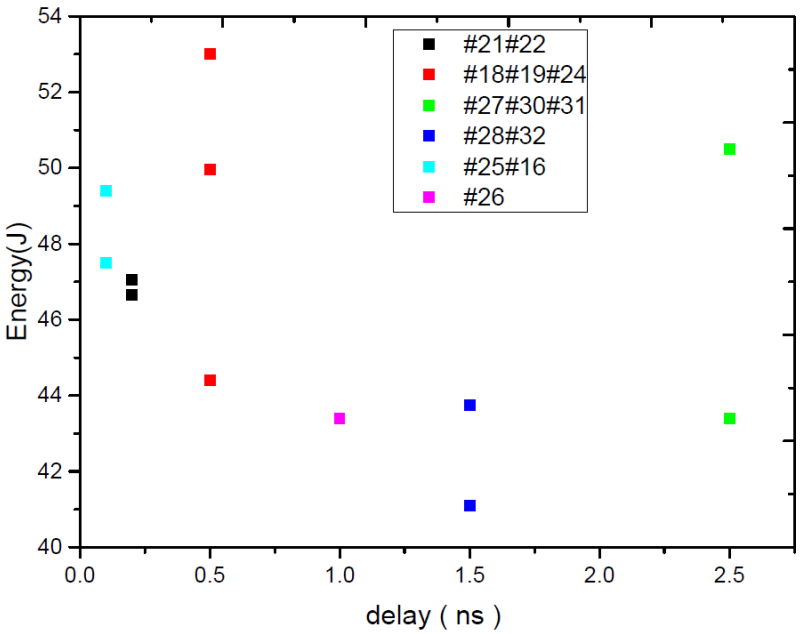

Fig 4.2.13 Function of dependents laser energy and delay

Set up presenting in a figure 4.2.6. During experimental campaign was done 35 shots. First 16 shots were done with 53 mm distances between object-detector other was done with 63.5 mm. 12 um Al + 100 um Polycarbonate x2 + 12.4 um Sc + 1 mm Polycarbonate was used like set of filters to prevent saturation of imaging plate. In figure presenting radiography data with different delay but same energy. We can clearly observe dependents from the time and expansion of the titanium wire.

We used a combination of X-ray spectroscopy and X-ray radiography for understanding the state of matter heated by electrons. X ray radiography was used in this experiment for imaging cold wire targets. Backlighter target was 5um tungsten wire. The experiment of heated wire was studied by time resolved X-ray radiography. Measurement of wire expansion was done at different time. X-ray radiography was successfully used to measure plasma expansion, sound velocity and plasma temperature.

During the experiment, hot electrons were generated through the interaction and propagated along the wire, resulting in isochoric heating of the titanium material. The term "isochoric" refers to a condition where the volume of the material remains constant during the heating process.

The hot electrons, accelerated by the laser, transferred their energy to the titanium wire, causing it to heat up. As the hot electrons propagated along the wire, they deposited their energy, leading to the heating of the titanium material without significant expansion or compression. This is in contrast to isobaric heating, where the pressure is kept constant during the heating process.

By studying the behavior of the hot electrons and their interaction with the titanium wire, researchers could gain insights into the energy deposition mechanisms, electron-heat transport processes, and the resulting temperature distribution within the wire. This information is crucial for understanding the dynamics of laser-matter interactions and the physics of high-energy-density systems.

The use of X-ray spectroscopy, such as XAS and XANES, along with X-ray radiography, allowed for the characterization of the isochorically heated titanium material. These techniques provided valuable data on the electronic structure, energy absorption, and expansion dynamics of the wire, enabling a comprehensive analysis of the isochoric heating process and its effects on the material. X-ray emisison spectroscopy (FSSR) of the titanium K-α line was performed to retrieve the wire temperature along the wire, i.e. T=T(z) where z=0 corresponds to the wire tip.

After this initial quasi-instantaneous heating, the expansion of the wire was followed using time-resolved X-ray radiography. Backlighter target was 5um tungsten wire illuminated by a second laser beam with similar characteristics. Measurement of wire expansion was done at different time by changing the delay between the two laser beams. X-ray radiography was successfully used to measure plasma expansion and sound velocity $c_s = c_s(z)$.

We observed how local plasma expansion velocity along the wire is consistent with the temperature extracted from FSSR data.

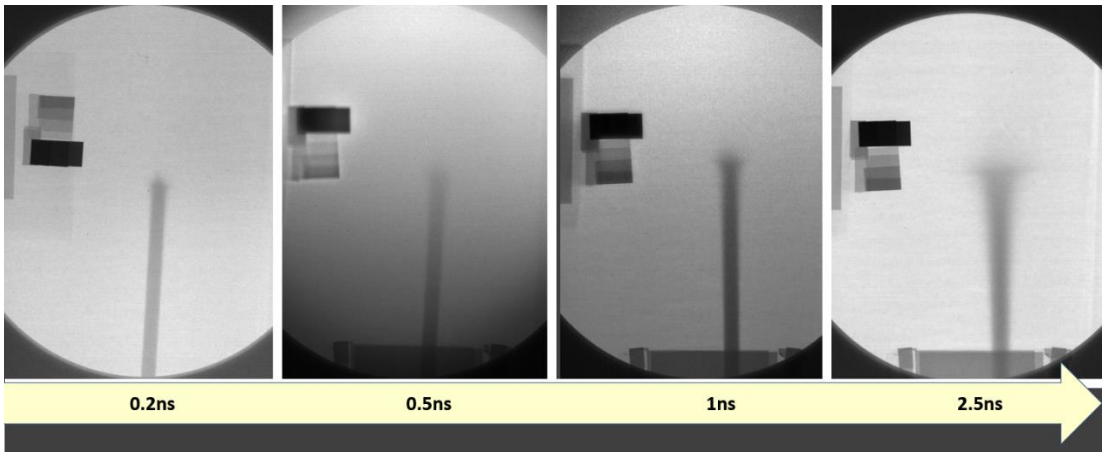

Fig4.2.14 Images of radiography shots #22 #24 #26 and #30 with different time delay presented on the arrow.

4.3 OMEGA EP EXPERIMENTAL CAMPEING

This section's experimental campaign was designed and scheduled in partnership with Laboratory for Laser Energetics, University of Rochester ,University of York, UK ,Rutherford Appleton Laboratory, UK ,CELIA, University of Bordeaux, France Ecole Polytechnique, Palaiseau, France, University of Rome "La Sapienza", Rome, Italy.

The application of x-ray phase-contrast imaging in the field of laser-driven high-energy density hydrodynamics is a powerful technique to image and locate shock-front positions in both high- and low-density regions of the target with higher accuracy than in standard absorption-based radiography.[i] It is expected that this technique will provide new physics insights in inertial confinement fusion and high-energy density physics experiments on MJ-class laser facilities such as the National Ignition Facility and LMJ-PETAL. We applied the technique on OMEGA EP to measure the density profile of strong shocks in solid CH targets and to image turbulent flows from hydrodynamic instabilities in CH foam targets. The IR short-pulse beam from OMEGA EP (50 ps, 250 J, ~2×10^{17} W/cm^2) was focused normal on either a 10-μm diameter Cu wire or a 5×30×300 μm^3 strip of Cu foil glued onto a 10 μm thin CH substrate producing ~8.6 keV x rays. The experiment demonstrated a spatial resolution of ~15 μm at sufficiently high photon energies so that the images were not affected by the strong x-ray self-emission from the plasma generated by the drive beams on the main target. One or two 2-ns, 1250-J, and 351-nm laser beams with an overlapped intensity of up to ~2×10^{14} W/cm^2 generated shock waves in the main target. High-quality radiographs of the shock front with phase-contrast enhancement were obtained for single-shock and double-shock experiments.

4.3.1 OMEGA EP laser facility

The 60-beam UV OMEGA Laser System was upgraded to the OMEGA EP (extended performance) Laser System in 2008, which enhances the performance and capabilities of the LLE Omega Laser Facility. OMEGA EP includes four individually programmable, frequency-tripled, kilojoule class NIF beamlines, two of which can be compressed for petawatt-class operation with brief pulses. High-field, high-pressure materials, high-energy-density (HED) research, as well as the creation of cutting-edge radiation sources for applications, are all made possible by the combination of high intensity and high energy in short- and long-pulse operation and flexible diagnostic systems. With 7 to 8 shots per day, a full system shot cycle of roughly 1.5 h is normal; however, interleaved beam operation on a shot cycle of 45 minutes is possible for appropriate studies with 2 additional shots per day.

The OMEGA-EP composed of 4 beams kilo-joule class principals. Two laser lines denoted BL-1 and BL-2 can be used as short pico-second pulses bringing them to near-PW class [Waxer et al., 2005] in this configuration. These two lines 1 and 2 are generally designated by the terms Side lighter and Backlighted respectively. To these two laser chains that can be used in short and long pulses are added 2 other

lines of light in pulse long nano-second only, carried by the BL- 3 and BL-4 beams. The duration between 2 shots on the installation is approximately one and a half hour but can be slightly reduced in the case where an alternation of 1-3 and 2 -4 beam configurations can be achieved. The experimental chamber is a spherical chamber 3.35 m in diameter.

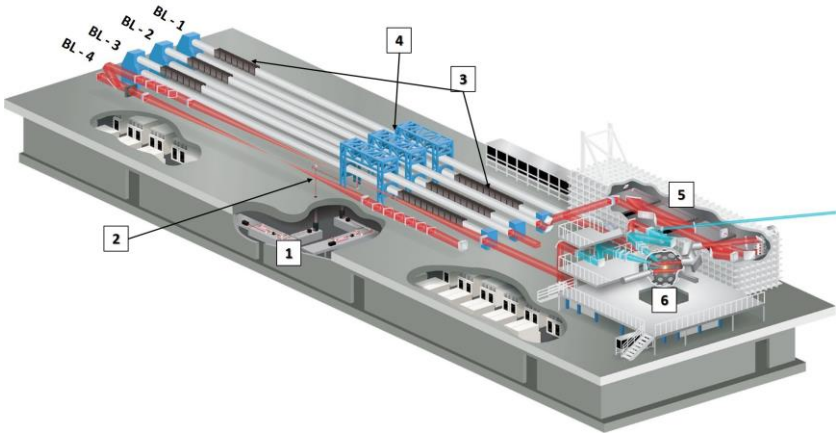

Fig4.3.1 Description of the OMEGA-EP installation: (1)-Laser sources , (2)-Source beam injection , (3)- Amplifiers , (4) Spatial filters , (5) Pulse beam compressor short - (6) Experimental chamber.

In order to describe the installation of OMEGA-EP [Omega EP facility.2006, 2007], we will then rely on the diagram presented in figure 4.3.1. Each of the 4 beams available has its source independent laser (1), located under the room where the beams are amplified. Laser sources beams 1 and 2 can provide an initial pulse between 1 and 1000 ps, while the sources for beams 3 and 4 provide initial pulses of 1×10 ns.

The beams are then raised using an optical lift (2) to then be amplified (3) at the main chain. Between each amplification step, the beams pass through filters (4), allowing to spatially clean the pulses laser to remove the high frequency components, before being tripled in frequency to reach a wavelength of 351nm to then be sent in the interaction chamber (6). Before being focused in the experimental chamber, beams 1 and 2 can be redirected to an optical compressor to adjust the duration of the pulsed beams short.

The beams are transmitted using vacuum tubes, at the same pressure as the interaction chamber, and a set of mirrors at the ends of their individual circuits. At the entrance to the chamber, the beams are focused using lenses, making it possible to define the size of the focal spot on the target in the center of the chamber. The spatial shaping and the homogeneity of the focal spot of the beams are obtained using phase plates arranged around the chamber.

Parameter of OMEGA EP laser facility available in a vacuum chamber is presented in a Table 4.3.1 below.

	Beam 1	**Beam 2**

Characteristics	Maximum	side lighter	Channel	Backlighted
Pulse duration (ps)	2	10	100	10
Focal spot (um)	10	10	20	10
Energy (kJ)	0.45	0.09	2	1.25
Intensity (W/cm^2)	~$2*10^{20}$	$5.7*10^{18}$	$6.3*10^{18}$	$1.6*10^{20}$

Table4.3.1 Parameter of OMEGA EP facility

Goal of experiment

X-ray phase contrast imaging (XPCI) is a technique that is widely used in biology and medicine. It is based on the phase-shift induced by a density gradient in matter. When a density gradient is present perpendicularly to the propagation direction of the x-ray, it deflects the x-ray beam in the opposite direction with respect to the density gradient. If we consider a density edge, the resulting XPCI image of this edge is located between a maximum and a minimum of the intensity profile. This effect can highlight every density interface and it is not density dependent. Strong density gradients of very different densities can be probed at the same time. This makes this diagnostic more versatile compared to standard x-ray absorption radiography. Additionally, XPCI is a useful tool for the study of warm dense matter and HED physics because it operates with both monochromatic and broadband sources. A common configuration for XPCI experiments is an X-ray free electron laser or synchrotron because of the high energy flux and beam coherence. However, lateral coherence, which is described as

$$l_t = R\frac{\lambda}{s}, \quad (4.11)$$

where s is the source's size, λ is the photon's wavelength, and R is the source's distance from the object. This formula makes it clear that phase-contrast enhancement is possible if one can employ a small source size, slightly hard x-rays (a few keV), and a setup that maximizes the source-object distance (which may be constrained by the photon flux and other technical requirements). Additionally, by using high-energy x-rays, it is possible to shield the detector from target self-emission and focus on the target's hydrodynamic evolution. proof-of-principle experiment at the PHELIX laser at GSI, Germany, using a laser-driven bremsstrahlung source, which produced experimental images of the shock front and the rarefaction wave.

As a proof-of-concept experiment was done using the PHELIX laser at GSI in Germany, giving experimental images of the shock front and the rarefaction wave using a laser-driven bremsstrahlung source. [Antonelli et al.,2019]

Goal of experiment was to develop the x-ray phase-contrast imagine (XPCI) technique on OMEGA EP with short pulse backlighter. This technique was applied

to measure the density profile of a strong shock. The possibility of XPCI to describe strong shocks on OMEGA EP is important step which give us opportunity to use this technique to lager laser facilities like NIF and LMJ.

4.3.2 Target

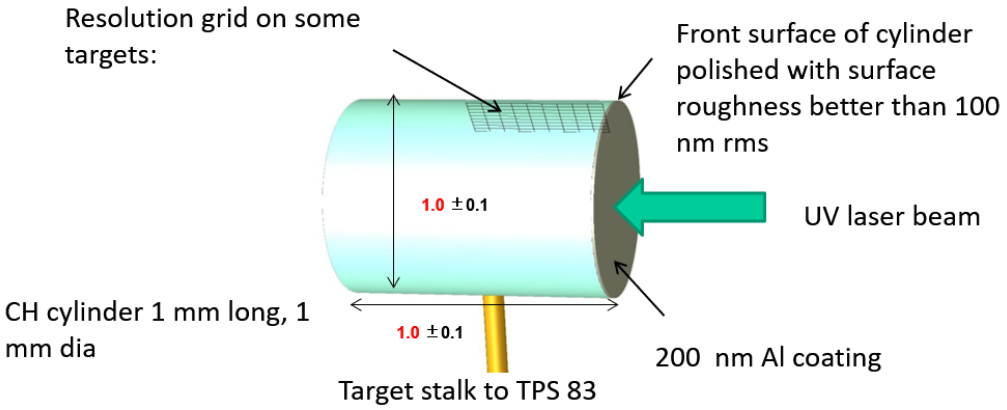

Fig 4.3.2 CH cylinder with Al coating was used as a main target

The target of this experiment consists of cylinder made by CH. CH cylinder long 1 mm and diameter 1 mm. Aluminum coating 200nm placed in a laser side. Front surface of cylinder is polished with surface roughness. Scheme of target shown in figure 4.3.2 . The target was glued in a flag configuration. The resolution grid was applied in some target.

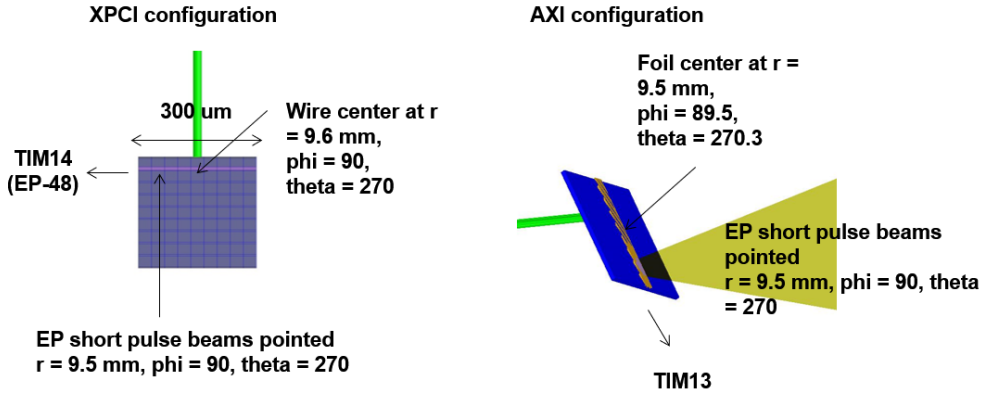

Fig 4.3.3 Positioning of backlighter target with respect to the pointing of the short pulse beams

As a backlighter target was used Cu wire 10 um. Wire was glued to a needle like flag in different angle from 0 to 23 degree. The Cu strip was aligned down the axis to TIM14, which contained a passive imaging plate detector in a heavily shielded box, and the IR beams B1 or B2 were focused normally onto the strip (LLDI).

For some shot was used undriven Aur grid with parameter presenting in Fig 4.3.4

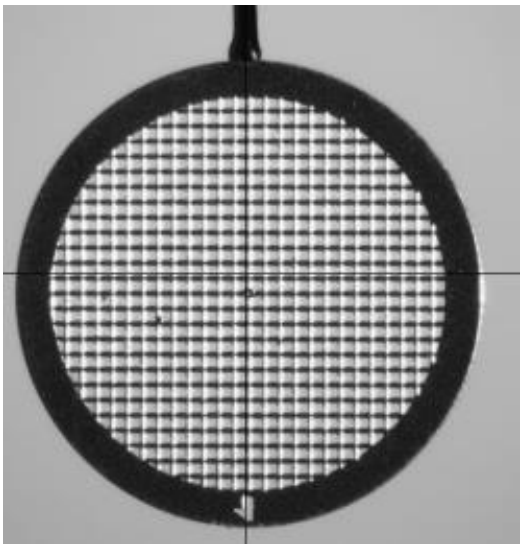

Fig4.3.4 Gilder Grids Standard Square Mesh, 3.05 mm diameter. 250 Au mesh, 100 um period, 70 um opening, 30 um bar. Thickness 18 um

4.3.3 Experimental set up

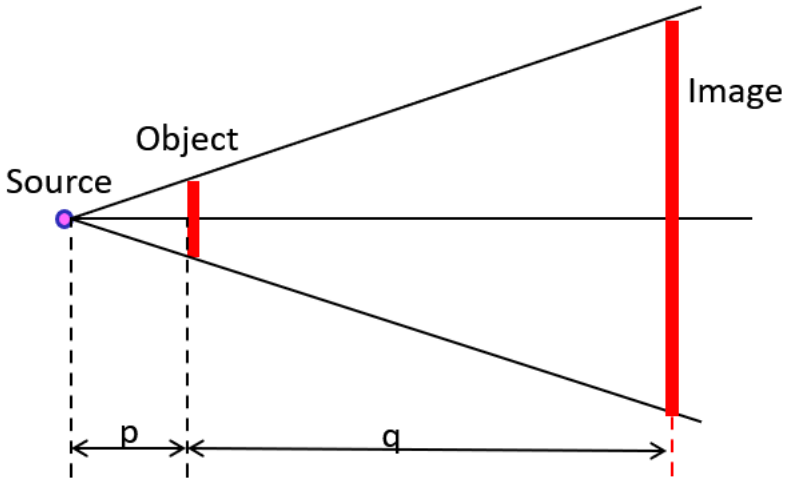

Fig 4.3.5 The point projection technique scheme

To calculate magnification was used simple formula M = (p+q)/p (4.12). As a detector was used imagine plate. Calculated parameter is presented in table 4.3.2

Standard radiography	XPCI

p(cm)	0.835	2.3
q(cm)	49.24	135.7
M	60	60

Table 4.3.2 Comparison of parameter between standard radiography and XPCI where p-distance between source and object, q distance between object and image and M- magnification.

Configuration of main beam and backlighter beam is shown in figure below.

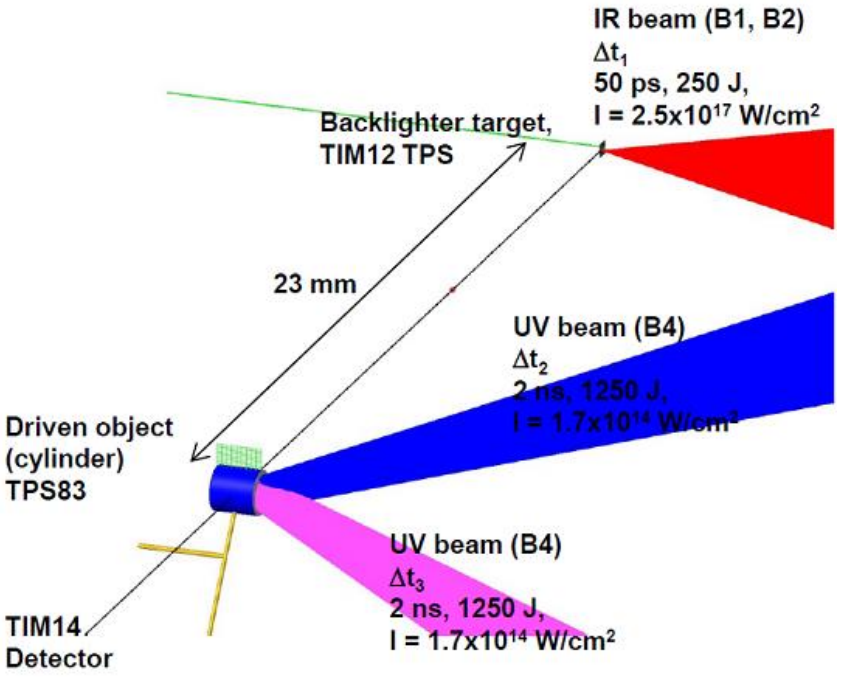

Fig4.3.6 Setup of the XPCI configuration on Omega EP

4.3.4 Result

In this part we discussed experiment (XPCI-EP-19A), that showed x-ray phase contrast imaging on OMEGA EP (Rochester ,US). In order to study the density profile of a strong shock in a cylindrical CH target, the experiment developed the XPCI technique on OMEGA EP with short pulse backlighter. The x-ray phase contrast source was tested on a range of backlighter targets composed of Cu material. At sufficient photon energies (8–9 keV), the experiment showed a spatial resolution of 15 m, which means that the images are undisturbed by the plasma corona's strong x-ray self-emission. Images of (a) a single and (b) a double laser-induced shock-wave are shown in Figure 4.3.7. The experimental setup is visualized in Fig 4.3.6. The two UV (λ= 0.35 m) laser beams (B3, B4) focused on the front side of a CH cylinder with a 1 mm diameter and 1 mm length produced an energy of 1250 J/beam in a 2 ns square pulse. The beams had SG8-0750 distributed phase plates (DPPs) attached, which provided a laser spot with a diameter of 750 um (1/e value of peak

fluence) and a fluence distribution envelope that is well represented by a super-Gaussian function of order 6.4.

The backlighter target was constructed from a 10 um-thin CH substrate and a 5-um-long, 30-um-wide strip of Cu foil that was attached to it. Strong emission between 8 and 9 keV, especially from the He_α and Ly_α resonance lines, was produced by the backlighter. A 60x magnification was possible thanks to the distances of 2.3 cm between the backlighter and the CH cylinder and 1.4 m between the CH cylinder and the IP detector. Resolution Au grids were mounted on the top of the cylinder, which provide a spatial fiducial and are used to infer the spatial resolution, which was found to be 15 μm in the horizontal direction and 18 μm in the vertical direction. The size of the source and the accuracy of the strip target alignment set a limit on the spatial resolution. The IP has numerous scratches visible in the photographs, which have somehow reduced the image quality. Before the experiment, the IPs were used numerous times, and as a result, scratches developed. Future experiments will apply for new IP set to prevent this.

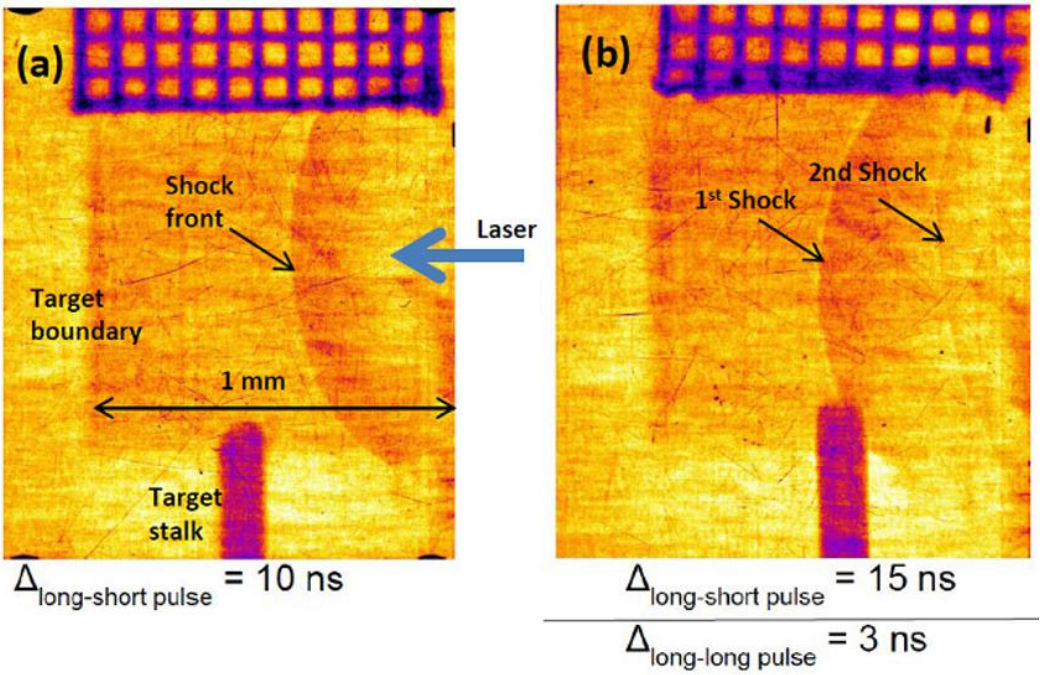

Fig 4.3.7 (a) Shot #30658.The data of single laser induced shock wave on OMEGA EP. Shot was taken 10ns after the start of the UV beam and the shock wave has propagated over several hundred um in the CH target. (b) Shot #30662 The XPCI data of double laser induced shock-wave on OMEGA EP. Shot was taken at 15 ns after the start of the first UV pulse. The second UV pulse was launched at a 3 ns delay with respect to the first UV pulse

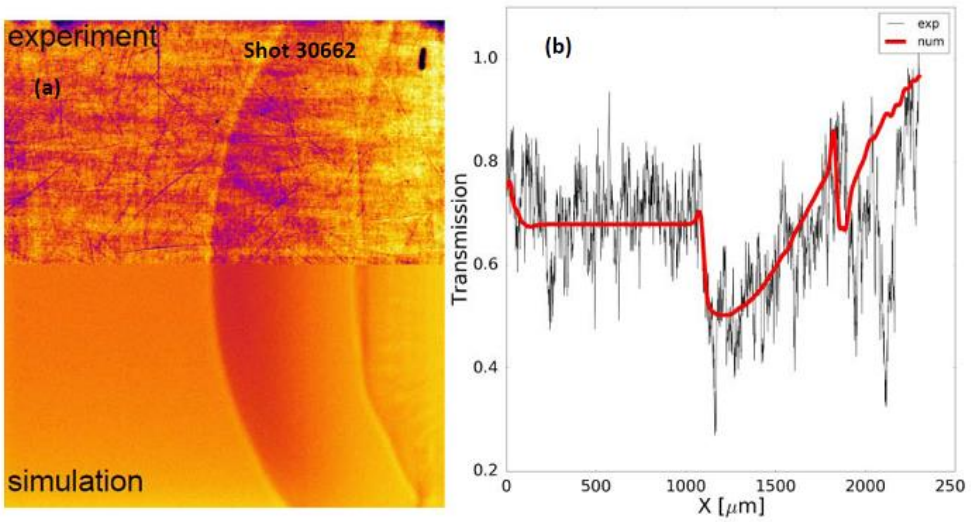

Fig4.3.8 (a) Comparison of the experimental data (top) from the double shock experiment and the simulated x-ray phase contrast image (bottom) showing good agreement of the general signal level and the positions of both shock fronts. (b) Line-outs along the horizontal axis of the experimental data and the simulated data, showing the typical signal excursions that are caused by the phase-enhancement.

Simulations of the UV beam interaction using the 2-D radiation hydrodynamic code DUED were able to accurately reproduce the results. Hydrodynamic codes as DUED are designed for calculating the properties of matter (pressure, density, temperature, and flow velocity), during the interaction with a laser by solving numerically the hydrodynamic equations. Figure 4.3.8 shows the experimental data from the double shock experiment at the top with a simulated x-ray phase contrast image at the bottom, demonstrating good agreement for both the general signal level and the positions of both shock fronts. Line-outs of the experimental data and the simulated data can be seen in Figure 1A.2 (b), illustrating the typical signal excursions brought on by the phase-enhancement. An XPCI code that is described in [Atzeni et al.,2005] was used to post-process the hydrodynamic simulation data. Because neither beam interacts with the target surface at normal incidence and also at an angle of incidence of 23 degrees with respect to the target normal, the shock wave is not perfectly symmetrical. The study of the data still seems to be ongoing, with plans to compare it to other hydrodynamic codes, improve picture filtering to increase image quality, and perhaps even compare it to other XPCI codes. The XPCI experiment on OMEGA EP showed that strong shocks can be imaged using x-ray phase contrast with more than enough contrast in a low Z material.

Chapter 5: Conclusions

The objective of this thesis was the study and optimisation of X-ray diagnostics of laser produced plasmas. In particular, I used a bremsstrahlung cannon to detect hot electrons produced in nanosecond laser interactions with solid wire targets. One method of characterizing hot electrons is to analyse the hard X-rays they emit while propagating inside the target material (bremsstrahlung emission). The broad continuous spectrum is related to the kinetic energy of electrons which produce it and therefore one can relate the emitted photon spectrum to the fast electron distribution.

The objective was to compare the performance of x-ray phase contrast imaging with X-ray absorption radiography. XPCI was used to study the dynamics of laser-generated shocks and blast waves propagating in plastic targets and to detect non-uniformities in compressed laser-irradiated materials. I have presented results from multiple experiments aimed at characterising the propagation of very strong shocks (initial pressures larger than 100 Mbar) in solid density materials. is important for developing a platform for diagnosing matter in extreme pressure conditions which are relevant for shock ignition conditions. The work focuses on the development and optimization of time-resolved X-ray imaging diagnostics for the study of physics of matter in extreme conditions (HED: high energy densities) and of inertial confinement fusion

In chapter 2 we report an experimental campaign, performed at the CLPU VEGA – II laser facility, focused on studying the dynamics of shock produced by fs-laser via the energy deposition from hot electrons generated in laser-matter interactions. Due to the short pulse, pressure is not maintained in time and the shock takes the form of a blast wave.

In the experiment, solid-density targets of various materials and thicknesses were irradiated by the by the fs-laser and a full characterization of the blast wave formation and propagation was performed using several diagnostics. Optical diagnostics (shock chronometry) provided information on the propagation of the blast wave in solids. Doppler reflectometry provided information on the target rear surface. Preliminary experimental results confirm the generation of a blast wave which is initially very strong and very rapidly decays in time, confirming the estimations of hydrodynamic and particle in cell simulations. X-ray emission was detected by using a bremsstrahlung cannon, a Kirkpatrick-Baez and GEMPix detector. Together with electron spectrometers they provided information about hot electron temperature.

In a chapter 2, we describe the “bremsstrahlung cannon” (BSC) and we discuss a simple approach to analysing the collected data.

The typical BSC design consists in a stack of detectors used to detect photons (imaging plates), separated by filters of different materials and thickness. The choice

of filter materials and thicknesses must be optimized for the expected photon distribution.

Bremsstrahlung spectra are usually assumed to be exponential corresponding to a hot electron Maxwellian distribution. The slope of this exponential is taken as a representative of the temperature of hot electrons. I developed an easy tool for estimating hot electron temperature, which is based on a semi-analytical model, which takes filter transmission and IP sensitivity into account. The method was used to analyse data from experimental campaigns conducted at various European large-scale laser facilities: Vega at CLPU (Spain), VULCAN at RAL (England) and Phelix at GSI(Germany). Obtained results were compered to Monte-Carlo simulations done by GEANT4 code using Penelope library.

In chapter 3 I introduced description of XPCI and described difference with classical X-ray radiography and X-ray phase contrast imagine. Different XPCI techniques described and compared on the basics the following points. Comparison based on four main points: setup, source spectrum and coherence, sensitivity and option of data post analysis.

X-ray imaging is used to observe shock waves travelling in target material. The state of art is represented by X-ray absorption radiography, which relies on the absorption of the photons travelling across matter. The disadvantages of this technique are: low sensitivity to low Z material (which are essentially transparent), and poor contrast at interface (like front-wave). These drawbacks would be addressed by using X-ray Phase Contrast Imaging (XPCI). XPCI is extensively used in different fields: from biology to material science, where it demonstrates a superior sensitivity to density variation than X-ray absorption imaging. Experimental campaigns described in chapter 4 successfully show the application of XPCI to laser-driven shock wave imaging.

In chapter 4.1 I described an experiment at the Vulcan TAW laser (Rutherford Appleton Laboratory, England) to study the propagation of shock-waves in solid targets. As diagnostic, we used phase-contrast-enhanced time-resolved X-ray radiography,while allows enhancing the visibility of discontinuities in the sample, like target edges and the shock front.

Thee laser beams (with duration of 2 ns, average total energy 550 J) were used to launch the shock. These were equipped with Phase plates producing a Gaussian spatial intensity distribution with FWHM = 400 μm. Then a laser pulse with duration of 1 ps, energy of 50 J was used to irradiate a back-lighter Cu wire (with diameter of 10 μm) producing photons at energy ≈8 keV.

The shocked target was a polymide tube (tube thickness 50 μm, inner diameter 1000 μm, length 1000 μm) filed with TMPTA foam (density 0.1 g/cm3). As ablator we used 25 μm of parylene, while the pusher was 5 μm Ti.

The propagation of a shock with a Gaussian shape is clearly observed in the 7 performed shots. Images were obtained for different time delays 15 ns, 25 ns and 35

ns allowing to follow the dynamics of shock propagation in time. We observed that the FWHM of spatial shape of shock front remains constant in time (with FWHM ≈600-700 μm). This seems to show that 2D effects in shock propagation are negligible in our case.

Finally experimental results were compared to numerical results obtained from 1D and 2D hydro simulations performed using the code MULTI.

In chapter 4.2 I studied the influence of laser pulse parameters on the temperature profiles of WDM generated in a titanium wire heated by a laser-accelerated hot-electron current in Phelix laser facility. Laser intensity and energy were varied in ranges of 6×10^{18}–6×10^{20} W/cm^2 and 50–200 J, respectively. The increase in laser energy (while keeping intensity constant) leads to an increase in the total HE energy and to the subsequent rise of WDM temperature in the first few hundred microns of the target. The HE temperature were obtained by BSC. Beyond laser intensities of about 1×10^{19} W/cm2 (which corresponds to ∼1 MeV characteristic temperature of hot electron distribution), the maximum WDM temperature becomes weakly sensitive to the laser intensity and mainly depends on the deposited energy. On the other hand, an increase of laser intensity at constant laser energy leads to heating of deeper target layers. These dependencies are explained with basic physical principles and simplified numerical simulation of HE flows and WDM heating to show the influence of laser parameters on the WDM temperature profile. Our experimental data may also be used to construct and verify more complex models of WDM heating by laser-accelerated HEs in further studies. The preliminary analysis of radiography images shows dependence between delay and expansion in a wire.

In chapter 4.3, we presented results obtained at the OMEGA EP laser facility. The diagnostic has been employed with a laser-produced broadband X-ray source. We clearly showed that it is possible to realise XPCI in a high energy facility and we used it to observe two subsequent shocks lunched in the material by double laser pulse.

In conclusion, the present work has demonstrated the feasibility of XPCI as new diagnostic tool for inertial confinement plasma and that XPCI can be a useful tool in studies of warm dense matter and high energy density physics. The rise of new laser facilities now offers exciting perspectives, opening new possibilities where XPCI could become a central diagnostic suitable for studying matter under extreme conditions including the observation of laser driven shock waves.

Bibliography

[Zel'dovich et al,1966] Ya. B. Zel'dovich Yu. P. Raizer. Phyisics of Shock Waves and High-Temperature Hydrodynamic Phenomena. *Academic Press New York and London*, 1966.

[Waxer et al,2005] L.J Waxer, D.N Maywar, JH Kelly, TJ Kessler, BE Kruschwitz, SJ Loucks, RL McCrory, DD Meyerhofer, SFB Morse, C Stoeckl, et al. High-energy petawatt capability for the omega laser. *Optics and photonics news*, 16(7) 2005.

[Maddox et al,2011] B R Maddox , H S Park, B A Remington, N Izumi, S Chen, C Chen, G Kimminau, Z. Ali, M. J. Haugh, Q. Ma High-energy x-ray backlighter spectrum measurements using calibrated image plates. *Review of Scientic Instruments* 82(2) 2011.

[Geant4,2021] Geant4 Installation Guide Documentation Release 11.0 2021

[Meadowcroft et al,2008] A. L. Meadowcroft, C. D. Bentley, and E. N. Stott. Evaluation of the sensitivity and fading characteristics of an image plate system for x-ray diagnostics. *Review of Scientic Instruments* 79(11) 2008.

[Boutoux et al,2016] G. Boutoux, D. Batani, F. Burgy, J.-E. Ducret,P. Forestier-Colleoni, S. Hulin, N. Rabhi, A. Duval, L. Lecherbourg, C. Reverdin2, K. Jakubowska, C. I. Szabo, S. Bastiani-Ceccotti, F. Consoli, A. Curcio, R. De Angelis, F. Ingenito, J. Baggio, and D. Raffestin. Validation of modelled imaging plates sensitivity to1-100 keV X-rays and spatial resolution characterisation for diagnostics for the "PETawatt Aquitaine Laser " *Review of Scientic Instruments* 87(4), 2016.

[Touati et at,2014]M Touati, J-L Feugeas, Ph Nicolaï, J J Santos, L Gremillet, and V T Tikhonchuk. Areduced model for relativistic electron beam transport in solids and dense plasmas. *New Journal of Physics*, 16(7), 2014.

[Bonnet et al 2013] T. Bonnet, M. Comet, D. Denis-Petit, F. Gobet, F. Hannachi, M. Tarisien, M. Versteegen, M. Aléonard Response functions of imaging plates to photons, electrons and 4He particles. *Review of Scientic Instruments* 84(10) ,2013

[Omega EP facility,2006] Omega EP facility. OMEGA EP System Operation Manual, (7) - System Description- Chap.1 System Overview. Laboratory for Laser Energetics, 2006.

[Omega EP facility,2007] Omega EP facility. OMEGA EP System Operation Manual, (7) - System Description - Chap.7 Experimental System. Laboratory for Laser Energetics, 2007.

[Antonelli et al.,2019] L. Antonelli, F. Barbato, D. Mancelli, J. Trela, G. Zeraouli, G. Boutoux, P. Neumayer, S. Atzeni, A. Schiavi, L. Volpe, V. Bagnoud, C. Brabetz, B.Zielbauer, P.Bradford, N.Woolsey, B.Borm and D. Batani. X-ray phase-contrast imaging for laser-induced shock waves *Europhysics Letters* 125, 2019

[Atzeni et al.,2005] S.Atzenia, A.Schiavia, F.Califanob, F.Cattanib, F.Cornoltib, D.Del Sartob, T.V.Liseykinab, A.Macchib, F.Pegorarob Fluid and kinetic simulation of inertial confinement fusion plasmas. *Comput. Phys. Commun*. 169 (153), 2005.

[Batani,2016] D. Batani, Matter in extreme conditions produced by lasers *EPL* 114(6), 2016.

[Betti et al., 2016] R. Betti and O. A. Hurricane, Inertial-confinement fusion with lasers, *Nat. Phys*. 12(5), 2016.

[Batani et al.,2014] D. Batani, S. Baton, A. Casner, S. Depierreux, M. Hohenberger, O. Klimo, M. Koenig, C. Labaune, X. Ribeyre, C.Rousseaux, G. Schurtz, W. Theobald, and V. T. Tikhonchuk, Physics issues for shock ignition, *Nucl. Fusion* 54(5), 2014.

[Mourou et al.,2006] G. A. Mourou, T. Tajima, and S. V. Bulanov, Optics in the relativistic regime, *Rev. Mod. Phys.* 78(2), 2006.

[Bailey et al.,2015] J. E. Bailey, T. Nagayama, G. P. Loisel, G. A. Rochau, C. Blancard, J. Colgan, P. Cosse, G. Faussurier, C. J. Fontes, F.Gilleron, I. Golovkin, S. B. Hansen, C. A. Iglesias, D. P. Kilcrease, J. J. MacFarlane, R. C. Mancini, S. N. Nahar, C.Orban, J.-C. Pain, A. K. Pradhan, M. Sherrill, and B. G. Wilson, A higher-than-predicted measurement of ironopacity at solar interior temperatures, *Nature* 517(7532), 2015.

[Nahar et al., 2016] S. N. Nahar and A. K. Pradhan, Large Enhancement in High-Energy Photoionization of Fe XVII and Missing Continuum Plasma Opacity, *Phys. Rev. Lett*. 116(23), 2016.

[Drake,2018] R. P. Drake, High-Energy-Density Physics: Fundamentals, Inertial Fusion, and Experimental Astrophysics ,2018.

[Zastrau et al.,2011] U. Zastrau, A. Sengebusch, P. Audebert, E. Brambrink, R. R. Fäustlin, T. Kämpfer, E. Kroupp, R. Loetzsch, Y. Maron,H. Reinholz, G. Röpke, E. Stambulchik, I. Uschmann, and E. Förster, High-resolution radial Kα spectra obtained from a multi-keV electron distribution in solid-density titanium foils generated by relativistic laser-matter interaction, *High Energy Density Phys*. 7(2), 2011.

[Schönlein et al,2016] A. Schönlein, G. Boutoux, S. Pikuz, L. Antonelli, D. Batani, A. Debayle, A. Franz, L. Giuffrida, J. J. Honrubia, J. Jacoby, D. Khaghani, P. Neumayer, O. N. Rosmej, T. Sakaki, J. J. Santos, and A. Sauteray, Generation and characterization of warm dense matter isochorically heated by laser-induced relativistic electrons in a wire target , *EPL* 114(4), 2016.

[Tikhonchuk, 2002] V. T. Tikhonchuk, Interaction of a beam of fast electrons with solids, *Phys. Plasmas* 9(4), 2002.

[Cui et al.,2013] Y.-Q. Cui, W.-M.Wang, Z.-M. Sheng, Y.-T. Li, and J. Zhang, Laser absorption and hot electron temperature scalings in laser–plasma interactions, *Plasma Phys. Control. Fusion* 55(8), 2013.

[Hutchinson,2002]I. H. Hutchinson, Principles of Plasma Diagnostics *Cambridge University Press*, 2002.

[Agostinelli et al.,2003] S. Agostinelli, J. Allison, K. Amako, J. Apostolakis, H. Araujo, P. Arce, M. Asai, D. Axen, S. Banerjee, G. Barrand, F. Behner, L. Bellagamba, J. Boudreau, L. Broglia, A. Brunengo, H. Burkhardt, S. Chauvie, J. Chuma, R. Chytracek, G. Cooperman, G. Cosmo, P. Degtyarenko, A. Dell'Acqua, G. Depaola, D. Dietrich, R. Enami, A. Feliciello, C. Ferguson, H. Fesefeldt, G. Folger, F. Foppiano, A. Forti, S. Garelli, S. Giani, R. Giannitrapani, D. Gibin, J. J.Gomez Cadenas, I. Gonzalez, G. Gracia Abril, G. Greeniaus, W. Greiner, V. Grichine, A. Grossheim, S. Guatelli, P. Gumplinger, R. Hamatsu, K. Hashimoto, H. Hasui, A. Heikkinen, A. Howard, V. Ivanchenko, A. Johnson, F. W. Jones, J. Kallenbach, N. Kanaya, M. Kawabata, Y. Kawabata, M. Kawaguti, S. Kelner, P. Kent, A. Kimura, T. Kodama, R. Kokoulin, M. Kossov, H. Kurashige, E. Lamanna, T. Lampen, V. Lara, V. Lefebure, F. Lei, M. Liendl, W. Lockman, F. Longo, S. Magni, M. Maire, E. Medernach, K. Minamimoto, P. Mora de Freitas, Y. Morita, K. Murakami, M. Nagamatu, R. Nartallo, P. Nieminen, T. Nishimura, K. Ohtsubo, M. Okamura, S. O'Neale, Y. Oohata, K. Paech, J. Perl, A. Pfeiffer, M. G. Pia, F. Ranjard, A. Rybin, S. Sadilov, E. di Salvo, G. Santin, T. Sasaki, N. Savvas, Y. Sawada, S. Scherer, S. Sei, V. Sirotenko, D. Smith, N. Starkov, H. Stoecker, J. Sulkimo, M. Takahata, S. Tanaka, E. Tcherniaev, E. Safai Tehrani, M. Tropeano, P. Truscott, H. Uno, L. Urban, P. Urban, M. Verderi, A. Walkden, W.Wander, H. Weber, J. P. Wellisch, T. Wenaus, D. C. Williams, D. Wright, T. Yamada, H. Yoshida, and D. Zschiesche,GEANT4 - A simulation toolkit," Nucl. Instruments Methods Phys. Res. Sect. A Accel. Spectrometers, *Detect.Assoc. Equip*. 506, 2003.

[Pompili et al,2016] R. Pompili, M. P. Anania, F. Bisesto, M. Botton, M. Castellano, E. Chiadroni, A. Cianchi, A. Curcio, M. Ferrario, M. Galletti, Z. Henis, M. Petrarca, E. Schleifer, and A. Zigler, Femtosecond dynamics of energetic electrons in high intensity laser-matter interactions, *Sci. Rep*. 6(1), 2016.

[Jackson et al,1999] J. D. Jackson and R. F. Fox, "Classical Electrodynamics,", *3rd ed Am. J. Phys*. 67(9), 1999.

[Zastrau et al,2010]U. Zastrau , E. Stambulchik, M. Bussmann, E. Förster, S. Höfer, T. Kämpfer, T. Kluge, E. Kroupp, R. Loetzsch, Y. Maron, H. Marschner , and I. Uschmann Electron trapping by strong Coulomb coupling in a relativistic laser plasma *Phys.Rev E* 81,2010.

[Neumayer et al,2005] P. Neumayer, R. Bock, S. Borneis, E. Brambrink, H. Brand, J. Caird, E. M. Campbell, E. Gaul, S. Goette, C. Haefner,T. Hahn, H. M.

Heuck, D. H. H. Hoffmann, D. Javorkova, H.-J. Kluge, T. Kuehl, S. Kunzer, T. Merz, E. Onkels, M. D.Perry, D. Reemts, M. Roth, S. Samek, G. Schaumann, F. Schrader, W. Seelig, A. Tauschwitz, R. Thiel, D. Ursescu, P.Wiewior, U. Wittrock, and B. Zielbauer, Status of PHELIX laser and first experiments, *Laser Part. Beams* 23(03),

2005.

[Bagnoud et al,2010] V. Bagnoud, B. Aurand, A. Blazevic, S. Borneis, C. Bruske, B. Ecker, U. Eisenbarth, J. Fils, A. Frank, E. Gaul, S.Goette, C. Haefner, T. Hahn, K. Harres, H.-M. Heuck, D. Hochhaus, D. H. H. Hoffmann, D. Javorková, H.-J. Kluge,T. Kuehl, S. Kunzer, M. Kreutz, T. Merz-Mantwill, P. Neumayer, E. Onkels, D. Reemts, O. Rosmej, M. Roth, T.Stoehlker, A. Tauschwitz, B. Zielbauer, D. Zimmer, and K. Witte, Commissioning and early experiments of the PHELIX facility, *Appl. Phys. B* 100(1),2010.

[Brailsford et al.,1946]Brailsford J. F., Br. J. Radiol., Roentgen's discovery of X-rays; their application to medicine and surgery *The British journal of radiology* 19(453) ,1946.

[Mould et al., 1980] Mould R. F., A History of X-rays and radium *IPC Business Press Ltd, London*,1980.

[Martynenko et al.,2021] A. S. Martynenko, S. A. Pikuz, L. Antonelli, F.Barbato, G. Boutoux, L. Giuffrida,J. J. Honrubia,E.Hume, J. Jacoby,D. Khaghani, K. Lancaster,P.Neumayer, O.N.Rosmej, J. J. Santos, O. Turianska,and D. Batani. Role of relativistic laser intensity on isochoric heating of metal wire targets" *Optics Express* 29 , 2021.

[Webb,1988]Webb S., The Physics of Medical Imaging *IOP Publishing, Bristol, UK* ,1988.

[Henke et al., 1993] B.L. Henke, E.M. Gullikson, and J.C. Davis. X-Ray Interactions: Photoabsorption, Scattering, Transmission, and Reflection at E = 50-30,000 eV, Z = 1-92. *Atomic Data and Nuclear Data Tables* 54(2) ,1993

[Tommasini et al.,2017] R. Tommasini, C. Bailey, D. K. Bradley, M. Bowers, H. Chen, J. M. Di Nicola, P. Di Nicola, G. Gururangan, G. N. Hall, C. M. Hardy, D. Hargrove, M. Hermann, M. Hohenberger, J. P. Holder, W. Hsing, N. Izumi, D. Kalantar, S. Khan, J. Kroll, O. L. Landen, J. Lawson, D. Martinez, N. Masters, J. R. Nafziger, S. R. Nagel, A. Nikroo, J. Okui, D. Palmer, R. Sigurdsson, S. Vonhof, R. J. Wallace, and T. Zobrist .Short pulse, high resolution, backlighters for point projection high-energy radiography at the National Ignition Facility. *Physics of Plasmas* 24(5) ,2017

[Suortti et al,2003] Suortti P. and Thomlinson W. Medical applications of synchrotron radiation, *Phys. Med. Biol*., 48 ,2003 .

[Bravin et al,2013] Bravin A., Coan P. and Suortti P., X-ray phase-contrast imaging: from pre-clinical applications towards clinics *Phys. Med. Biol*., 58 ,2013.

[Bonse et al., 1965] Bonse U. and Hart M., An x-ray interferometer with long separated interfering beam paths *Appl. Phys. Lett*., 6 ,1965.

[Snigirev et al., 1995] Snigirev A., Snigireva I., Kohn V., Kuznetsov S. and Schelokov I., On the possibilities of x-ray phase contrast microimaging by coherent high-energy synchrotron radiation *Rev. Sci.Instrum*., 66 ,1995

[Diemoz et al.,2012] P.C. Diemoz, A. Bravin, M. Langer, and P. Coan. Analytical and experimental determination of signal-to-noise ratio and figure of merit in three phase-contrast imaging techniques. *Optics Express* 20 (25) 2012.

[Pogany et al.,1997] A. Pogany, D. Gao, and S. W. Wilkins. "Contrast and resolution in imaging with a microfocus x-ray source." *Review Of Scientific Instruments* 68 (7)1997.

[Dean et al,2014] Dean M. Connor and Z. Zhong. "Diffraction-Enhanced Imaging." *Current Radiology Reports* 2(7) , 2014.

[Munro et al., 2013] Munro P. R. T., Hagen C. K., Szafraniec M. B. and Olivo A., Applications of a non-interferometric x-ray phase contrast imaging method with both synchrotron and conventional sources *Opt. Express*, 21, 2013.

[Diemoz et al,2013] Diemoz P. C., Endrizzi M., Zapata C. E., Pesic Z. D., Rau C., Bravin A.,Robinson I. K. and Olivo A., X-Ray Phase-Contrast Imaging with Nanoradian Angular Resolution *Phys. Rev. Lett*., 110, 2013

[Peterzol et al.,2005] Peterzol A., Olivo A., Rigon L., Pani S. and Dreossi D., The effects of the imaging system on the validity limits of the ray-optical approach to phase contrast imaging *Med. Phys*., 32 ,2005.

[Olivo et al,2001] Olivo A., Arfelli F., Cantatore G., Longo R., Menk R. H., Pani S., Prest M., Poropat P., Rigon L., Tromba G., Vallazza E. and Castelli E., An innovative digital imaging set-up allowing a low-dose approach to phase contrast applications in the medical field *Med. Phys*., 28 , 2001

[Wilkins et al,1996] S. W. Wilkins, T. E. Gureyev, D. Gao, A. Pogany, and A. W. Stevenson. Phase contrast imaging using polychromatic hard X-rays. *Nature* 384(6607) 1996

[Stutman et al.,2011] D. Stutman and M. Finkenthal. Talbot-Lau x-ray interferometry for high energy density plasma diagnostic. *Review of Scientific Instruments* 82(11) ,2011.

[Pagot et al., 2005] E. Pagot "Quantitative comparison between two phase contrast techniques: diffraction enhanced imaging and phase propagation imaging. *Physics in medicine and biology* 50(4),2005.

[Zhou et al.,2013] T. Zhou, U. Lundström, T. Thüring, S. Rutishauser, D. H. Larsson, M. Stampanoni, C. David, H. M. Hertz, and A. Burvall. "Comparison of two x-ray phase-contrast imaging methods with a microfocus source. *Optics Express* 21(25) ,2013.

[Donnelly et al.,2003] E. F. Donnelly, R. R. Price, and D. R. Pickens. Quantification of the effect of system and object parameters on edge enhancement in phase-contrast radiography.*Medical physics* 30(11), 2003.

[Pfeiffer et al.,2008] F. Pfeiffer, M. Bech, O. Bunk, P. Kraft, E. F. Eikenberry, Ch Brönnimann, C. Grünzweig, and C. David. Hard-X-ray dark-field imaging using a grating interferometer. *Nature Materials* 7(2)2008

[Zeraouli at al.,2019] G. Zeraouli, G. Gatti, A. Longman, J. A. Pérez-Hernández, D. Arana, D. Batani, K. Jakubowska, L. Volpe,L. Roso, and R. Fedosejevs Development of an adjustable KirkpatrickBaez microscope for laser driven x-ray sources *RSI* 90 (6), 2019

Appendices

Appendix A

Hydrodynamic plasma description

The plasma is considered as neutral, made of two different fluids of two species - the electrons and the ions in the hydrodynamic model. Each fluid can be described by four hydrodynamic variables: the mass density $\rho_{e,i}$, the average velocity $\boldsymbol{u}_{e,i,}$ the average energy ε, and the pressure *P*. For both the electron and the ion fluid, the equations of conservation of mass, momentum and energy are written as

$$\frac{\partial \rho_{e,i}}{\partial t} + \Delta \rho_{e,i} \boldsymbol{u}_{e,i} = 0 \qquad (1.1)$$

$$\rho_{e,i} \frac{\partial \boldsymbol{u}_{e,i}}{\partial t} + \rho_{e,i} \left(\boldsymbol{u}_{e,i} \nabla\right) \boldsymbol{u}_{e,i} + \nabla P = F_{ext} \quad (1.2)$$

$$\frac{\partial}{\partial t}\left[\rho_{e,i}\left(\varepsilon + \frac{1}{2}u_{e,i}^2\right)\right] + \nabla\left[\rho_{e,i}\boldsymbol{u}_{e,i}\left(\varepsilon + \frac{1}{2}u_{e,i}^2\right) + P\boldsymbol{u}_{e,i}\right] = w_V + w_S + q_H + q_{ext} + q_{exhange} + q_{rad} \qquad (1.3)$$

Where are the external forces F_{ext}, the volumetric work w_V , the surface work w_s, the heat transport q_H , the external heat q_{ext} , the heat exchanged between the two fluids $q_{exhange}$ and the radiative contribution q_{rad} . $\rho_{e,i}, \boldsymbol{u}_{e,i}, \varepsilon, P$ are the plasma physics quantities. The latter gives a relation between these hydrodynamic variables. Such equation is called Equation of State (EOS) and is usually presented as:

$$\varepsilon = \varepsilon(P, \rho) (1.4)$$

For a complete resolution, the heat transport coefficients of the system also must be determined, and furthermore the hydrodynamic equations have to be coupled to the Maxwell equations, as the external force F_{ext} and the pressure P may depend on the electromagnetic fields. The plasma hydrodynamic codes are usually based on the solving of the hydrodynamic equations coupled with Maxwell equations in order to predict the evolution of the plasma variables over space and time.

MULTI 1D and MULTI 2D codes were used to model shock wave propagation in a solid target in this work.

Appendix B MULTI 2D simulations

I=1.5 10^{13} W/cm^2
FLHM=300 um

15 ns 25 ns 35ns

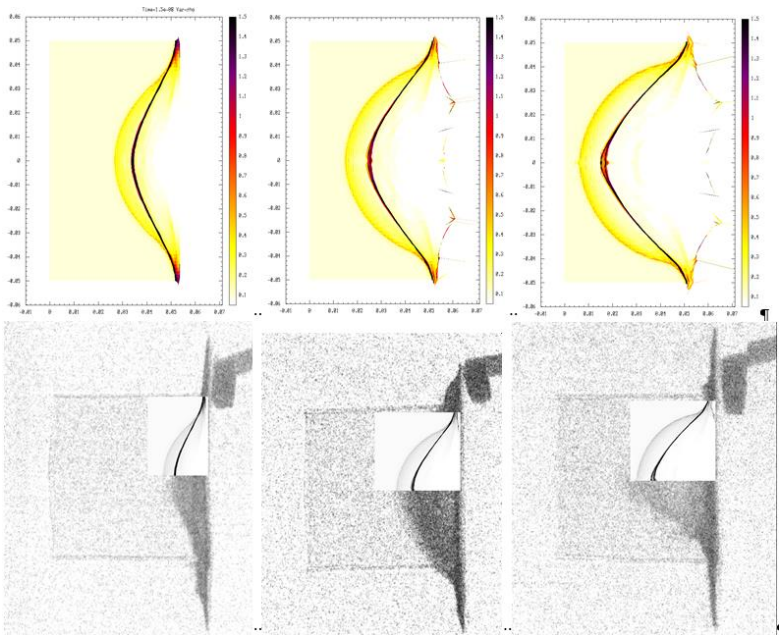

I=1.5 10^{13} W/cm^2
FLHM=400 um

15 ns 25 ns 35ns